Characterizing the Atmospheric Neutrino Spectrum with the IceCube Neutrino Observatory

by

Tania R. Wood

A thesis submitted in partial fulfillment of the requirements for the degree of

Doctor of Philosophy
in
Physics

Department of Physics
University of Alberta

Abstract

Neutrinos, one of nature's fundamental particles, have been demonstrated to oscillate (change flavour) from their point of production to detection; implying neutrinos must have mass and hence providing the first evidence for physics beyond the Standard Model of Particle Physics. Atmospheric neutrinos, produced in cosmic ray interactions with the Earth's atmosphere, played a crucial role in the first measurements of neutrino oscillations, thereby launching the current era of precision measurements of neutrino properties. These enigmatic particles from our atmosphere continue to comprise an important part of the global neutrino effort, acting as a primary signal for some experiments, and a key background consideration for others. In particular, advancing our understanding of the production mechanisms, and hence the resultant flux, of atmospheric neutrinos has become increasingly important as planning for the next generation of particle astrophysics detectors takes centre stage in this rapidly evolving field.

This thesis presents a study of the atmospheric neutrino flux in an energy range between 5.6 GeV and 180 GeV reconstructed energy. Particular attention is paid to measurements of the kaon-to-pion parent meson contributions to the flux, providing a direct measure of the production mechanisms of the neutrinos in the atmospheric in-

teractions. The study utilizes the world's largest accumulated data set of atmospheric neutrinos, detected with the cubic-kilometre-scale IceCube Neutrino Observatory located at South Pole Station, Antarctica.

The results of the analysis are the first atmospheric neutrino energy spectrum measurements from IceCube's DeepCore low-energy detector array. The data set extends the previous measured IceCube atmospheric neutrino energy spectrum from 100 GeV in ν_μ [1] and 80 GeV in ν_e [2], down to 5.6 GeV; providing the highest precision to date in much of the considered energy range. A series of 19 leading atmospheric neutrino flux models were tested against the IceCube-DeepCore data; the best fit of the atmospheric models was rejected at a level of 3.79σ. Due to limited statistics in the data sample above $\sim$80 GeV, it was found that this analysis had only limited sensitivity to the kaon-to-pion ratio and provided a measurement of predominately pion parent mesons in the sample. We note that the methods used in this analysis are flux preserving, unlike previous IceCube-DeepCore oscillation results, and we find the extracted oscillation parameters to be within the 90% confidence limits of the previous results [3].

The results from this study directly impact the on-going and future measurements and modelling of atmospheric neutrinos and their production processes. It is rather remarkable that, after providing one of the key measurements that launched the field of measuring neutrino mixing parameters, the atmospheric neutrino oscillation parameters are now some of the least well known. One of the primary limitations to improving this scenario has been a precise knowledge of the source of atmospheric

neutrinos at energies neighbouring those where oscillation measurements are prevalent.

The presented analysis investigates a crucial (overlap) region for the atmospheric neutrino flux energy spectrum that complements previous measurements at lower-energies (*e.g.* by the Super-Kamiokande experiment in Japan) and the significantly higher energy regime opened by the IceCube detector. This overlap region has largely been lacking in experimental measurements, affecting the historical precision of estimating the potential flux contributions at these energies. The direct measurements provided here augment the active modelling of the atmospheric neutrino predictions at these energies, providing a path to directly improve the current and future atmospheric neutrino oscillation programs.

Preface

The work presented in this thesis is the author's own and is original except where noted below. The use of other's work is cited in the text where relevant.

The IceCube Neutrino Observatory is the result of work of thousands of scientists and engineers over 20 years. The IceCube collaboration publication author list currently has approximately 300 identified contributors. As such, it is natural that an author over the course of a doctoral degree contributes to many collaborative efforts.

The analysis of the atmospheric neutrino models and the characterization of the atmospheric neutrino energy spectrum has been independently developed by the author, although some of the applied software tools and methods were developed for other purposes by members of the collaboration. Specifically, the software tool applied as the base of the analysis frame work was developed by Juan Pablo Yanez (doctoral thesis, DESY 2014). For the purposes of this analysis, the framework was significantly modified to accommodate the unfolding of the atmospheric neutrino energy spectrum. The flexible theoretical atmospheric lepton flux modelling software MCEq was developed by A. Fedynitch et. al. [4]. The author provided the first low-energy ($\sim$5 GeV–1 TeV) verification of the MCEq output via comparisons to the HKKM2014 [5] model, as well as developed the software for flux table generation at

the IceCube detector location. The modified χ^2, applied as the fitter minimization function in this analysis, was originally developed by the IceCube collaboration in [3].

The author was the first member of the IceCube collaboration that brought the above elements together in a way that allows one to perform a first measurement of the atmospheric neutrino energy spectrum in the low-energy regime with the IceCube-DeepCore array.

Acknowledgements

Thank you to my supervisor Darren Grant. This thesis would not be possible without your vision and patient editing. I would also like to thank the IceCube Collaboration in general and its wonderful members for the opportunity to explore exciting science together; I have made lifelong friends and had experiences I will always remember.

A special thank you is due to Juan Pablo Yanez and also to Anatoli Fedynitch and for their advice and contributions to this work.

Thank you to my office mate and longtime friend Sarah Nowicki for support and friendship and thanks to Thomas McElroy for sharing woes and taking care of me along the way; I don't know what I would have done without your friendships in the dark times. Thank you to my parents for their excitement about my work, for understanding the time commitment it takes and for their examples of hard work and relentless determination. Thank you to my brother Robert and to those I was closest too for their compassion and support during the sometimes isolating years of undergrad and grad school.

Contents

List of Tables

List of Figures

List of Abbreviations

List of commonly used abbreviations

CR	Cosmic Ray (primary particle)
DAQ	Data Acquisition
DeepCore	low energy extension (5GeV-100GeV) of IceCube
DRAGON	Name of the data sample used
DOM	Digital Optical Module
eV	electronVolt, 1.6×10^{-19} Joules
fADC	fast Analog-to-Digital converter
GEANT	GEometry ANd Tracking software
GeV	Giga-electronVolt
HQE	High Quantum Efficiency
HV	High Voltage
IceCube	IceCube neutrino observatory (detector)
kg	kilogram
kpc	kiloparsec (3.086×10^{19} m)
K/π	leptons coming from kaon decays over leptons coming from pion decays
LED	Light Emitting Diode
MCEq	Matrix Cascade Equation solver
PE	Photo Electron
PID	Particle Identification algorithm
PMT	PhotoMultiplier Tube
Super-K	Super-Kamiokande neutrino observatory (detector)

Chapter 1

Introduction

Neutrinos are fundamental particles in nature, second only to photons in abundance in the universe [6]. A cornerstone of the Standard Model of Particle Physics (see Figure 1.1), neutrinos are leptonic particles with spin 1/2 and no charge. Neutrinos interact with other Standard Model particles only via the weak force through exchange of a $W^{\pm}$ or Z^0 boson. As such, neutrinos have a very small probability (cross-section) for interaction and therefore propagate essentially unhindered over cosmological distances between their point of origin and detection. This has made the study of the neutrino's inherent properties quite challenging. As an example, it was nearly 80 years after first being postulated [8] that it was determined neutrinos are not massless. This discovery was made via the observation that neutrinos oscillate (change flavour) as they propagate [9, 10]. That neutrinos are massive is widely recognized as one of the first direct pieces of evidence for physics beyond the Standard Model; neutrinos are unique in that they have an anomalously small masses [8], suggesting either a non-standard model coupling to the Higgs boson or another (as yet unknown) form of mass generation.

Neutrinos are produced prolifically in the fusion processes that take place in stars, in the decay of radio active elements, and in the high energy collisions at astrophysical sources, in particle accelerators on Earth, and in cosmic ray interactions in our atmo-

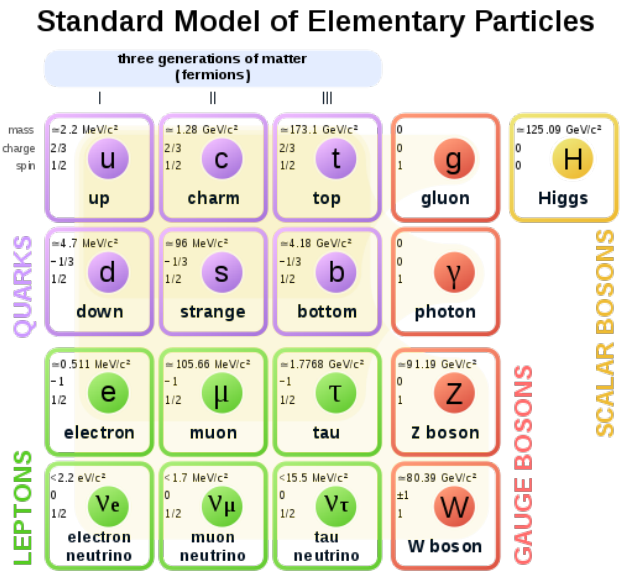

Figure 1.1: Showing the Standard Model of particle physics [7]. The Standard Model describes the interactions between the building blocks of matter and three of the four fundamental forces. The building blocks are made up of basic particles called quarks and leptons, which occur in related pairs or 'generations'. The lightest pair making up the first generation. Interactions of the three forces (electromagnetic, weak and strong) are carried via the exchange of bosons (the 'force carriers'). The colour groups shown here are the quarks in green, the leptons in blue and the bosons (which are the force carriers) in red.

sphere. The latter are known as atmospheric neutrinos. Measurements of oscillations in atmospheric neutrinos [9] near the GeV-scale played a crucial role in launching the current global program to measure the neutrino mixing parameters. It is somewhat remarkable that the atmospheric neutrino parameters are now some of the least precisely measured [11]. This is primarily due to a few key factors: measurements of atmospheric neutrinos have largely been statistically limited due the size of the available detectors, where (below 100 GeV) the predicted spectrum changes shape and is rapidly falling; the cosmic ray spectrum and hadronic interaction models, that provide the neutrino source in the oscillation measurements, represent the largest uncertainties in these studies [12] and improvements in their precision has remained an experiment and theoretical challenge for the broad field.

The IceCube neutrino observatory (IceCube), located at South Pole Station, Antarc-

tica, detects Cherenkov photons produced by charged particles propagating through the Antarctic ice. At the cubic-km-scale, IceCube is the world's largest neutrino detector (by volume) and measures neutrinos with high efficiency at energies between approximately 5 GeV and the PeV-scale. The low-energy infill detector array, called DeepCore, deployed in the deepest and clearest glacial ice at the bottom of the IceCube detector is optimized to detect neutrinos between 5 GeV and approximately 200 GeV; a region ideal for studies of atmospheric neutrinos, including the energy spectrum and neutrino oscillations. The DeepCore volume at nearly 30 MTonne provides unprecedented number of neutrino candidates (nearly 200,000 per year at trigger-level; and 20,000 per year at final analysis level). By utilizing the main IceCube array as a active veto volume against the otherwise potentially overwhelming background of atmospheric muons, DeepCore provides the capability to overcome statistical limitations in previous measurements of atmospheric neutrino oscillations. In addition, studies of the spectral shape and therefore the underlying production mechanisms of the cosmic ray interactions are possible; the detector is sensitive to the crossover region between the dominant meson production in the showers, pions and kaons, which are in turn tied to the hadronic interactions.

This thesis presents an analysis that overlaps with, and explores the regions between, atmospheric neutrino flux energy spectrum measurements established at low energies by Super-Kamiokande [13] and at higher energies by IceCube [1] [2]. A precise measurement of the atmospheric neutrino flux will directly impact current and future neutrino oscillation analyses, and will inform corrections to the available cosmic ray spectrum and hadronic interaction models, in particular refining the existing large uncertainties in the predictions for pion and kaon production in high-energy air showers. With the lowest statistical uncertainty atmospheric neutrino sample available to date, a binned analysis utilizing a modified χ^2 test is performed. Two case studies are implemented; in the first, 19 atmospheric neutrino flux models are tested against IceCube data; in the second, a (quasi) model-independent characterization of the spectrum is obtained, including a precision measurement of the atmospheric

neutrino energy spectrum and extraction of the oscillation parameters.

In Chapter 2, the reader will find a detailed description of the theoretical connection between cosmic ray interactions and atmospheric neutrino production. Chapter 3 provides an overview of large-scale neutrino detectors including the introduction to IceCube. In Chapter 4, we introduce the details of the construction of the IceCube data handling and the event selection to generate the final analysis level data sample. Chapter 5 provides the reader with an overview of the simulation generation for the primary analyses and the data/simulation verification cross-checks of the final data sample. The primary analysis tools for the atmospheric neutrino flux measurement, including the event reconstruction and particle identification algorithms, as well as the detector livetime corrections, are described in Chapter 6. Chapter 7 provides a detailed overview of the systematic uncertainties considered in the analysis and then describes the analysis methods (distinctly the model-dependent and (quasi) model-independent case studies) as well as the background considerations. In Chapter 8, the results of the measurements are reported and the thesis concludes with Chapter 9, where a discussion of results in view of their impact on the global measurements is presented. Chapter 9 closes with a brief outlook of future considerations for improving the analysis.

Chapter 2

From Cosmic Rays to Neutrinos

Kilometre-scale hybrid detectors, like the IceCube Neutrino Observatory, have made possible extensive combined particle and high energy cosmic ray physics. Particle astrophysics brings these topics together in a symbiotic relationship where natural beams of particles from astrophysical and atmospheric origin provide high statistics data samples that can be used to tell us more about the cosmos, particle interaction physics, neutrino properties and the standard model of particle physics.

This chapter describes the theoretical connection between cosmic ray interactions and atmospheric neutrino production. Section 2.1 presents a description of cosmic ray physics and section 2.2 presents the relevant information on atmospheric neutrinos.

2.1 Cosmic Rays

Cosmic rays, discovered in 1912 by Victor Hess [14], are high energy particles of extraterrestrial origin consisting of ionized nuclei, 90% of which are protons, 9% helium nuclei, and 1% heavier nuclei [14]. They strike the Earth's atmosphere at a rate of $\sim$ 1000 per square meter per second. In 1938, Pierre Auger demonstrated the existence of extensive air showers (cascades of secondary particles) initiated by

these cosmic rays, noting energies above 10^{15} eV [15]. This was done by observing the simultaneous arrival (coincident in timing) of secondary particles over hundreds of meters of detectors, indicating they were part of the same event. Today, cosmic ray detectors have measured events with energies up to 10^{22} eV [14].

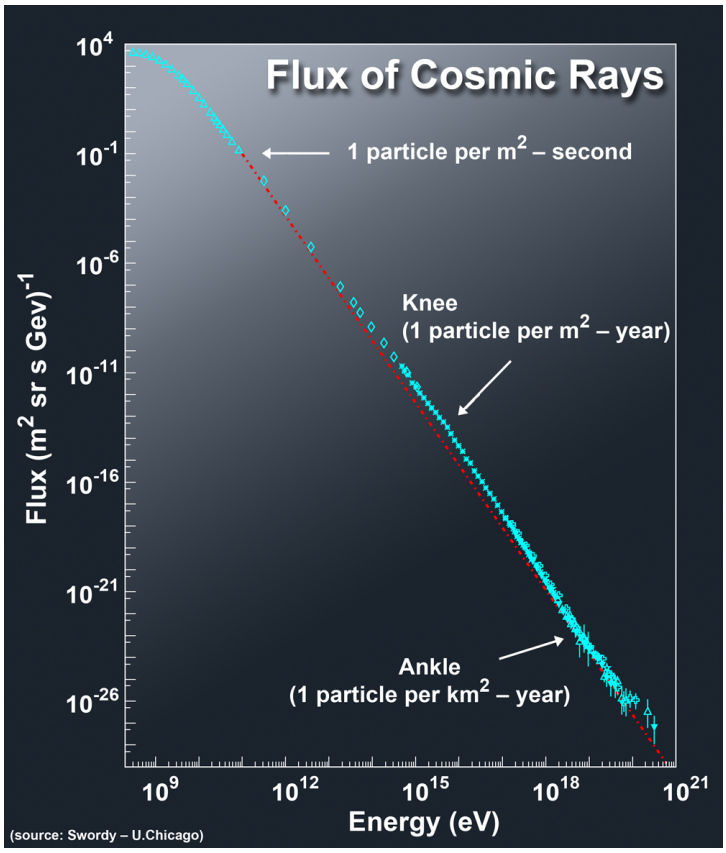

Figure 2.1: The Cosmic Ray Spectrum. At 100 GeV, we expect one particle per square meter per second [16].

Their origin and the acceleration mechanisms, however, remain unknown [6]. In recent years it has become clear that the majority of cosmic rays originally from inside our galaxy, but outside of our solar system [6]. It is expected that several source populations are needed to explain the observed cosmic ray spectrum [6]. The small fraction of cosmic rays that come from the Sun (Population 1, cutting off at $\sim$ 10 GeV) are temporally correlated with violent solar events [6]. In general, cosmic ray rates show anti-correlation with solar activity as the expanding magnetized plasma from the sun (solar wind) is effective at pushing the emitted particles out of

our solar neighbourhood [6]. Also within our galaxy are (Population 2) old supernovae remnants (*i.e.* 10-20 yrs old), with an energy cut off at $\sim$ 100 GeV [17].

Up to energies of $\sim 10^{15}$ eV, cosmic ray particles originate primarily from within the Milky Way in stars or stellar events [6]. This may be from the fast-moving magnetic shock fronts thrown out by supernova explosions, and phenomena like our solar wind and represent Population 3 that cuts off near energies of 100 TeV, or the 'knee' of the spectrum. These moving magnetic shocks, where the magnetic field slows abruptly, can cause particles to be trapped, or 'reflected'. In this way, cosmic ray nuclei can gain energy from a shock front [16]. Direct evidence from X-ray and radio emission have shown that these magnetic shock fronts accelerate electrons to near the speed of light, but evidence that high energy protons and other nuclei, making up the major component of cosmic rays, are also accelerated in the same way is only circumstantial and needs further study [16]. Beyond these energies are in Population 4, galactic fast spinning massive stars with mass 20-50 M_{sun}, and galactic hyper-novae (rare, 1 in 1000 years), creating TeV-PeV neutrinos and Population 5, galactic hyper-novae and gamma-ray bursts (GRBs) (rare, 1 in 10,000 years), that may create PeV neutrinos.

The cosmic rays expected to be of extra-galactic origin are at the highest energies and have gyro-radii larger than the size of the galaxy [6]. These events may provide clues about physics at extreme energies, in addition to the astrophysical information they carry. Beyond these energies, the highest energy magnetic shock fronts observed cannot produce the highest energy cosmic rays, and their origin is entirely unknown. Observational evidence suggests that cosmic rays above 10^{18} eV (Population 6, extragalactic protons, which are expected to be superimposed on population 5, also creating PeV neutrinos and above) originate from outside our own Galaxy, as they do not, in measurements to date, point back to sources, even though at such energies, the expected deflection of these particles should be small. They also do not seem to arrive preferentially from the disk of the Milky Way or the centre of the galaxy. The origin of such cosmic rays are only hypothesized; sources including Active Galactic Nuclei (AGN) jets or colliding black holes [6].

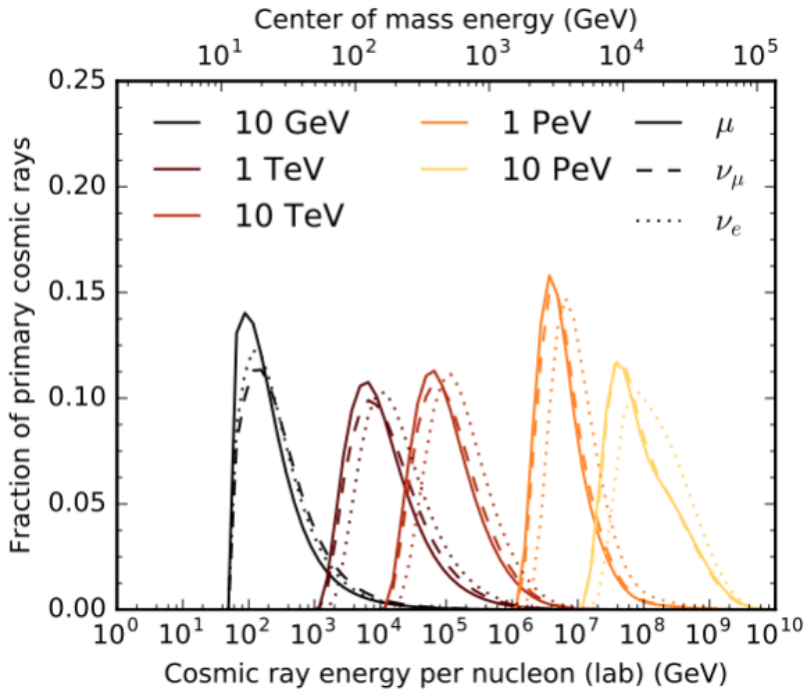

Figure 2.2: Showing a simulation of the fraction of cosmic ray primaries as a function of energy in the lab frame and center of mass frame [18] [19]. The solid, dashed and dotted lines show muon and neutrino particles. For example, a 10 GeV neutrino is primarily produced by 100 GeV cosmic rays, but there is a small tail on either side. Note that the hard cut off at low energy for the neutrinos and muons is due to the model having no data below 50 GeV/nucleon cosmic ray - air interactions. This limits the accuracy of the prediction at the lowest energies.

As a general guide, the cosmic ray primary energy is approximately an order of magnitude higher than the energy of the neutrino it eventually produces (see figure 2.2). Cosmic rays occur over a very broad range and IceCube uniquely provides sensitivity over nearly 8 orders of magnitude (see figure 2.3).

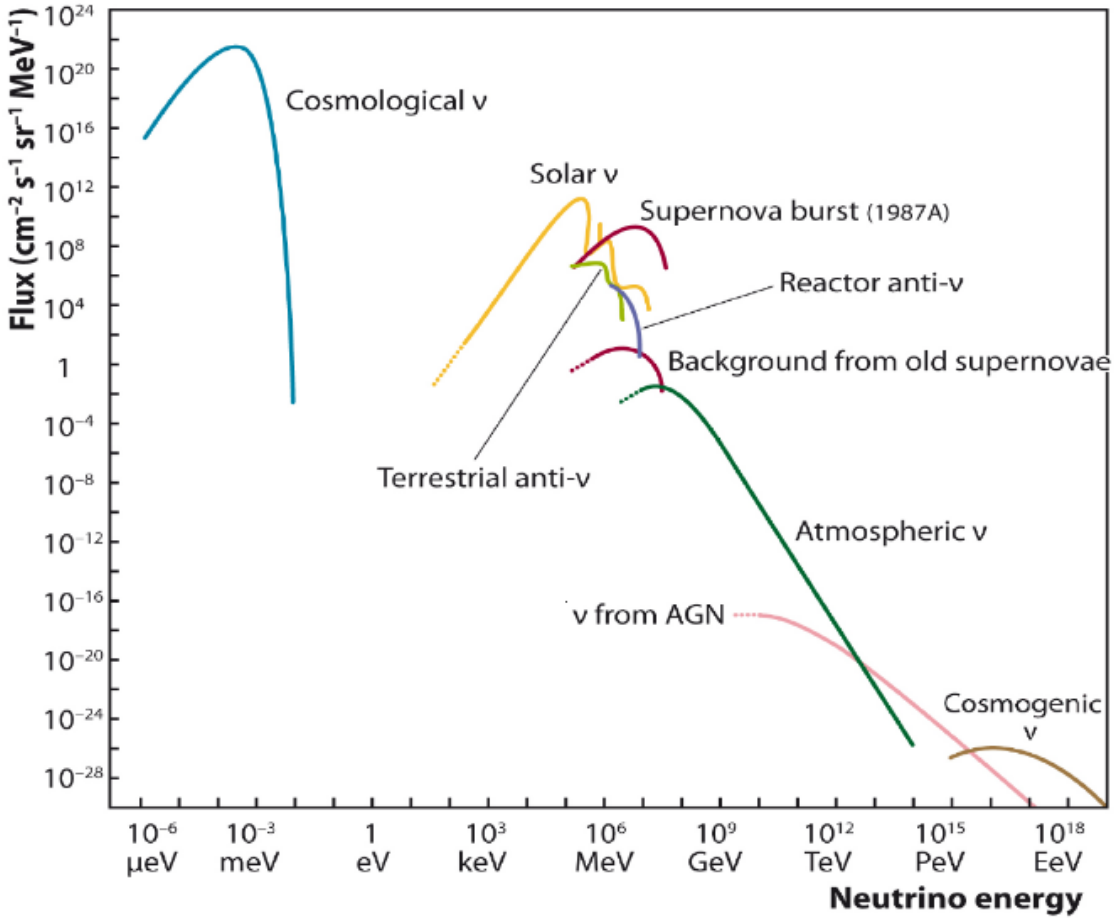

Figure 2.3: Showing the expected flux of neutrino sources for various energy ranges [20].

2.2 Atmospheric Neutrinos

2.2.1 Creation of Atmospheric Neutrinos

An atmospheric neutrino is that produced in on atmospheric interaction of a cosmic ray particle or 'primary'.

The resultant hadronic shower from the interaction produce mesons which then ultimately decay into muons and atmospheric neutrinos. The relevant (dominant) channels for this are:

$$CR(p,n,etc) + AirNuc \rightarrow \pi^{+/-} + X, K^{+/-} \tag{2.1}$$

$$\pi^+, K^+ \rightarrow \mu^+ + \nu_\mu$$

$$\mu^+ \rightarrow e^+ + \nu_e + \bar{\nu_\mu} \tag{2.2}$$

or:

$$\pi^-, K^- \rightarrow \mu^- + \bar{\nu_\mu}$$

$$\mu^- \rightarrow e^- + \bar{\nu_e} + \nu_\mu, \tag{2.3}$$

where 'p, n, etc' is a cosmic ray (CR) consisting of a proton or a heavier element and $AirNuc$ is a nucleus in an air molecule in the atmosphere. From this chain, one can see the expected flux ratio of the three flavours of neutrinos is $(\nu_e : \nu_\mu : \nu_\tau) = (1 : 2 : 0)$. There are no ν_τ produced as atmospheric neutrinos except for a small contribution from charmed mesons (D) at the highest energies.

2.3 Atmospheric Neutrino Spectrum

The atmospheric neutrino spectrum may be modelled in a simple way by modifying the relative abundance of pions and kaons produced in the air showers [21].

$$\Phi_\nu(E,\theta) = \Phi_N(E)X(w_\pi + w_K) \tag{2.4}$$

$$w_\pi = \frac{A_\pi}{1 + B_{\pi\nu}Ecos\frac{\theta^*}{\eta_\pi}} \tag{2.5}$$

$$w_K = \frac{A_K}{1 + B_{K\nu}Ecos\frac{\theta^*}{\eta_K}} \tag{2.6}$$

where $A_{\pi,K}$ are related to the production of pions and kaons, and $B_{\pi\nu,K\nu}$ corresponds to the decay kinematics and attenuation lengths. This simplified analytic approxima-

tion of the spectrum follows a power law, much like the cosmic ray spectrum. This is expected since the atmospheric neutrino spectrum is the convolution of the cosmic ray spectrum at the Earth's atmosphere with the neutrino yield from the cosmic ray hadronic interaction. From this model, the relative contribution fraction of kaons (K) and pions (π) contributing to that atmospheric neutrino spectrum may be estimated as a function of neutrino energy (see Figures 2.4, 2.5), where the first figure uses the simplified approach shown here and the latter figure shows a similar plot using a full numerical solution of the matrix cascade equations [18].

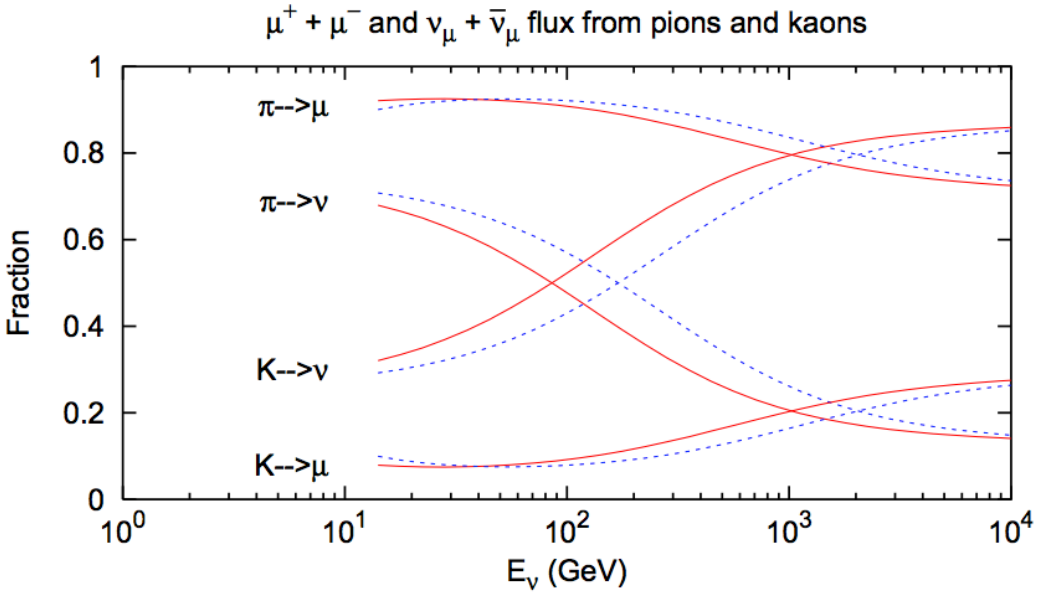

Figure 2.4: Showing the fractional contribution of first produced parent particles to the flux of atmospheric neutrinos. The bottom curve for pions (red solid) is vertical (zenith angle 90°) and the blue dotted line is for zenith angle of 60°, which can be taken as the average value [21].

The energy and zenith distribution of the kaon and pion neutrino parent leptons contain information about the primary cosmic rays and the atmospheric hadronic

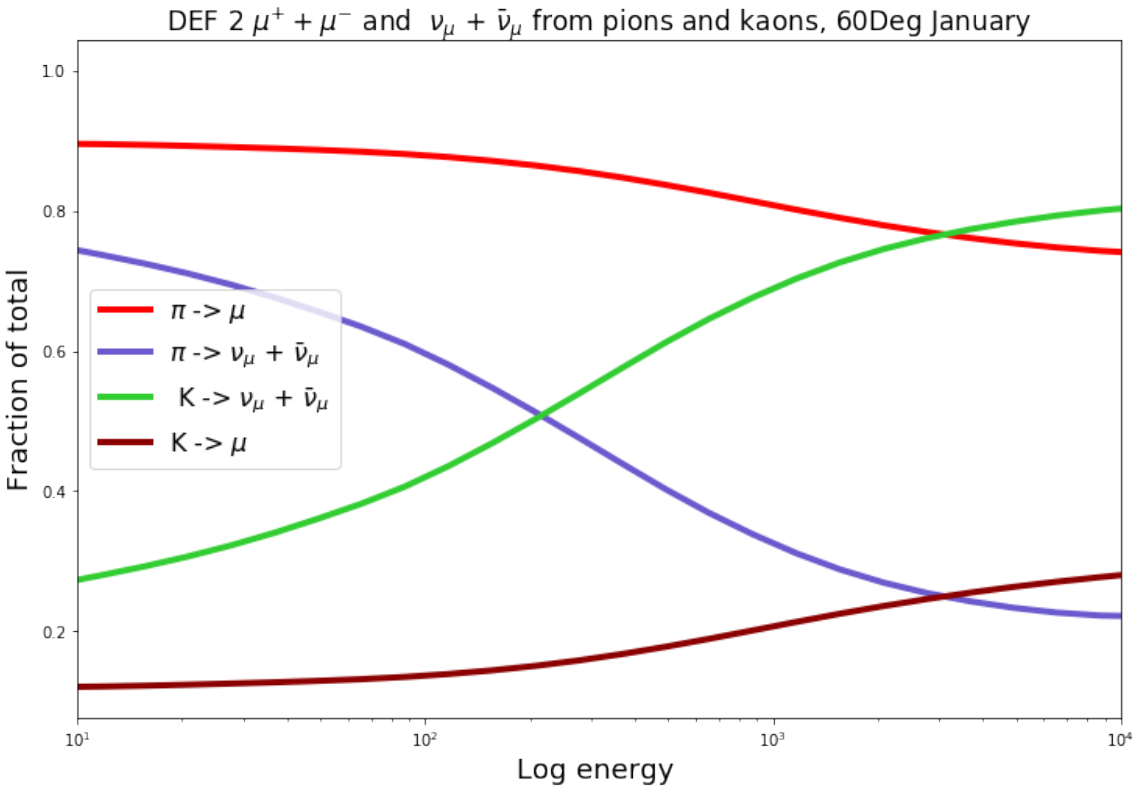

Figure 2.5: Showing the fractional contribution of first produced parent particles to the flux of atmospheric neutrinos, zenith angle 60°. The primary (cosmic ray) spectrum is Gaisser-Honda [21] and the interaction model is DPMJET-III-2017.1 [22].

interactions.

Here, the ν_μ flux is dominated by contributions arising from the decay of charged pions ($\pi^\pm$) (at low energies) and kaons ($K^\pm$) (above $\sim$ 80 GeV, depending on the zenith angle and choice of hadronic interaction model). For ν_e, the flux is dominated by contributions from the decay of muons (created from the decay of charged pions and kaons), K^0_L and $K^\pm$.

The kaon-to-pion ratio (K/π) is used in parameterizations of the ν_μ flux and is defined as the quotient of the fraction of leptons coming from kaon decay over the fraction of leptons coming from pion decay. It depends on branching ratios and energy distributions of a given decay and is a function of zenith. A good knowledge of these processes is needed to obtain a robust understanding, with associated uncertainties,

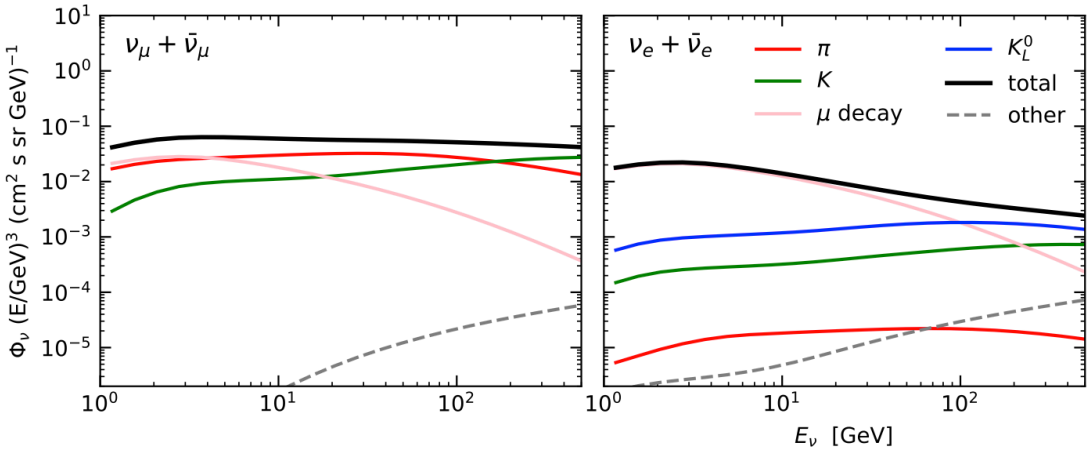

Figure 2.6: Partial contribution of mesons to the flux of atmospheric neutrinos, muon neutrinos (left) and electron neutrinos (right) at a zenith angle of 60°. The primary (cosmic ray) spectrum is Gaisser-Honda [21] and the interaction model is DPMJET-III [23, 22]. This plot is created with MCEq [18]. This plots shows the contributions from the most recent meson. See Appendix D.2.5 for plots showing how this change in definitions effects the fractional contributions.

of the spectrum at higher energies. This knowledge is critical for atmospheric neutrino studies of fundamental neutrino properties and to determine backgrounds for astrophysical neutrino searches.

In the electron neutrino channel, the K/π is primarily dependent on the muon distribution and is otherwise not well defined, as pions effectively do not decay directly to electron neutrinos (branching ratio is at 10^{-4}).

The atmospheric ν_μ flux produced by pions has a notable zenith and energy dependence (see figure 2.7). This leads to a zenith and energy dependence for the K/π ratio. The zenith angle dependence arises from the variation of the atmosphere traversed by the mesons and the difference in their lifetimes. The angular dependence of the pions component creates zenith dependent rate changes observable by IceCube, providing sensitivity to the K/π ratio. This becomes important as a calibration input to interaction models and for the benchmarking of flux models.

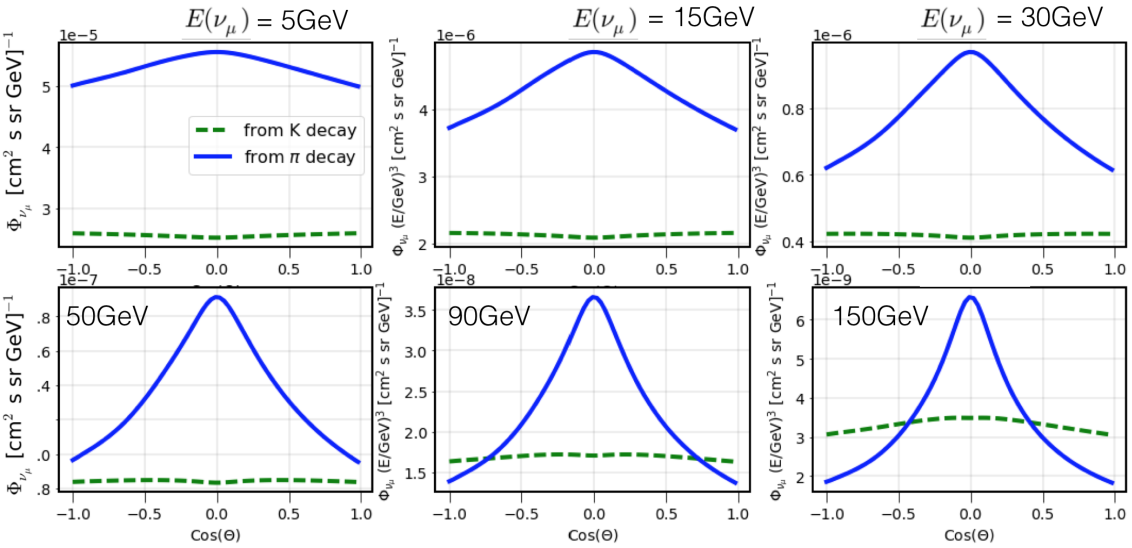

Figure 2.7: Showing the atmospheric muon neutrino flux dependence on zenith-angle, and to a lesser extent, energy; here shown for a variety of energies over the analysis range. As well, one can see the kaon contribution slowly rising with energy. The zenith angle shown is relative to the IceCube detector coordinate system, where -1 corresponds to 'upward going' events, i.e. events travel up into the detector (*i.e.* coming up from below the detector, having traveled through the earth).

Chapter 3

Large-scale Neutrino Detectors and the IceCube Observatory

Detecting neutrinos is challenging because of their tiny interaction probability (cross-section). Huge volumes are typically instrumented to detect enough neutrinos to perform statistically significant measurements. For the study of atmospheric neutrinos, detectors in the many kiloton range are needed, while for astrophysical neutrinos, which have an even lower flux, detectors in the gigaton range are required [15]. The IceCube neutrino observatory was the first such gigaton detector, instrumenting 1 km^3 of the glacial ice sheet at the geographic South Pole.

This chapter provides an overview of Cherenkov detectors with a focus on the IceCube Neutrino Observatory.

3.1 Large-scale Neutrino Detection Principles

3.1.1 The Cherenkov Effect

Large-scale neutrino detectors, exceeding 10s of kilotonnes active fiducial volume, have utilized water Cherenkov techniques. These detectors equip large volumes of water with optical sensors (photosensitive devices such as photomultiplier tubes) and detect Cherenkov light emission from the charged leptons produced by neutrino interactions with nuclei in the target medium. Cherenkov radiation, discovered by Pavel Cherenkov in 1934 [24], is produced when the velocity of a charged particle exceeds the phase velocity of the EM fields (the 'speed of light') in a given media [25]. That is

$$v \geq \frac{c}{n} \tag{3.1}$$

$$\beta = \frac{v}{c} \geq \frac{1}{n} \tag{3.2}$$

where n is the index of refraction in a media.

The charged particle polarizes the atoms in the medium as it traverses its path. The medium then emits light during the relaxation of the atoms. Since the particle travels faster than light in the medium, the light from the relaxation interferes constructively, resulting in a wavefront that appears cone-like moving out away from the particle's track (see Figure 3.1). This 'shock front' manifests as the emission of Cherenkov photons at a fixed angle (the opening angle of the cone), characteristic for a given media:

$$cos\theta_c = \frac{c/n}{\beta c} = \frac{1}{\beta}, \tag{3.3}$$

where β = v/c, and c is the speed of light in a vacuum with wavelength dependent index of refraction, n.

The Cherenkov light radiated along the charged particle's path will receive a boost with respect to interaction light where a small cascade of short of lived hadronic particles are created.

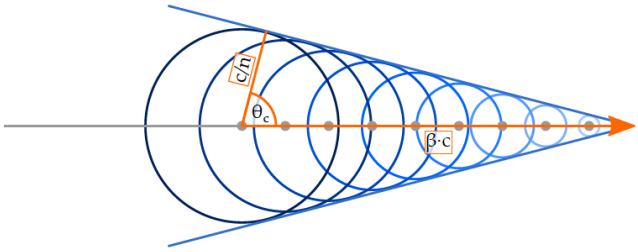

Figure 3.1: Cherenkov radiation and an illustration of the Cherenkov angle.

The number of photons produced by the charged particle can be estimated with the Frank-Tamm formula [26], which is defined per wavelength ($d\lambda$) and length traversed (dx) as

$$\frac{d^2N}{dxd\lambda} = \frac{2\pi\alpha}{\lambda^2}\left(1 - \frac{1}{n^2\beta^2}\right), \tag{3.4}$$

where α is the fine structure constant, $\alpha \approx \frac{1}{137}$.

Note here that the intensity of the Cherenkov light increases with decreasing wavelength, resulting in most photons being produced in the ultraviolet region. In the wavelength range of 300-500 nm (blue-green), where a photomultiplier tube (PMT) typically has greater sensitivity, a muon in, *e.g.*, the ice produces close to 250 photons per cm [27]. The range of a muon in ice, $R_\mu \approx 0.23$ GeV/meter [28]. This means a 50 GeV muon would travel ≈ 250 meters in ice. Note, only a certain percentage of the event energy goes to the muon.

3.2 Energy Loss of Charged Particles

The amount of energy lost by a particle through Cherenkov radiation is relatively small; far less than through ionization [29]. The Bethe-Bloch equation describes

electronic stopping power *i.e.* energy loss of a charged particle due to the ionization and excitation of nuclei in a given material [29]. A general version of the equation is

$$-\frac{dE}{dx} = 4\pi N_A r_e^2 m_e c^2 z^2 \frac{Z}{A}\frac{1}{\beta^2}\left(\ln\frac{2n_e c^2\gamma^2\beta^2}{I} - \beta^2 - \frac{\delta}{2}\right), \tag{3.5}$$

where z is the charge of the particle in units of e, Z is the atomic number of the medium, A is the atomic mass number of the medium, m_e is the electron mass, r_e is the classical electron radius, $\frac{e^2}{4\pi\epsilon_0 m_e c^2}$, and N_A is Avogadro's number. Here I is the mean excitation energy of the medium, which can be approximated by $I = 16\cdot Z^{0.9}$eV for Z >1. Finally, the δ term is known as the density correction.
For particle detection there exists a predicted region near the minimum where the stopping power of a given particle in a given medium is approximately linear (see Figure 3.2). Particles in this energy range are known as minimum ionizing particles (MIPs). With a well predictable energy loss, minimum ionizing atmospheric muons are often used as a calibration source of a detector.

If we define a be the electronic stopping power of a given medium, from equation 3.5, then the average rate of energy loss for muons can be described as:

$$\left\langle -\frac{dE}{dx}\right\rangle = a(E) + b(E)E, \tag{3.6}$$

where E is the energy of the traversing particle, and the new term b, describes the radiative processes involved (bremsstrahlung, pair production, photo-nuclear interactions), i.e. $b = b_{brems} + b_{pair} + b_{nucl}$.

These energy loss processes are defined as:

- Bremsstrahlung - occurring when a charged particle is decelerated by an electric field and loses energy through photon emission.
- Pair production - occurring when a particle passes through a material's nuclear electric field loses energy through the production of an e^+e^- pair via a virtual

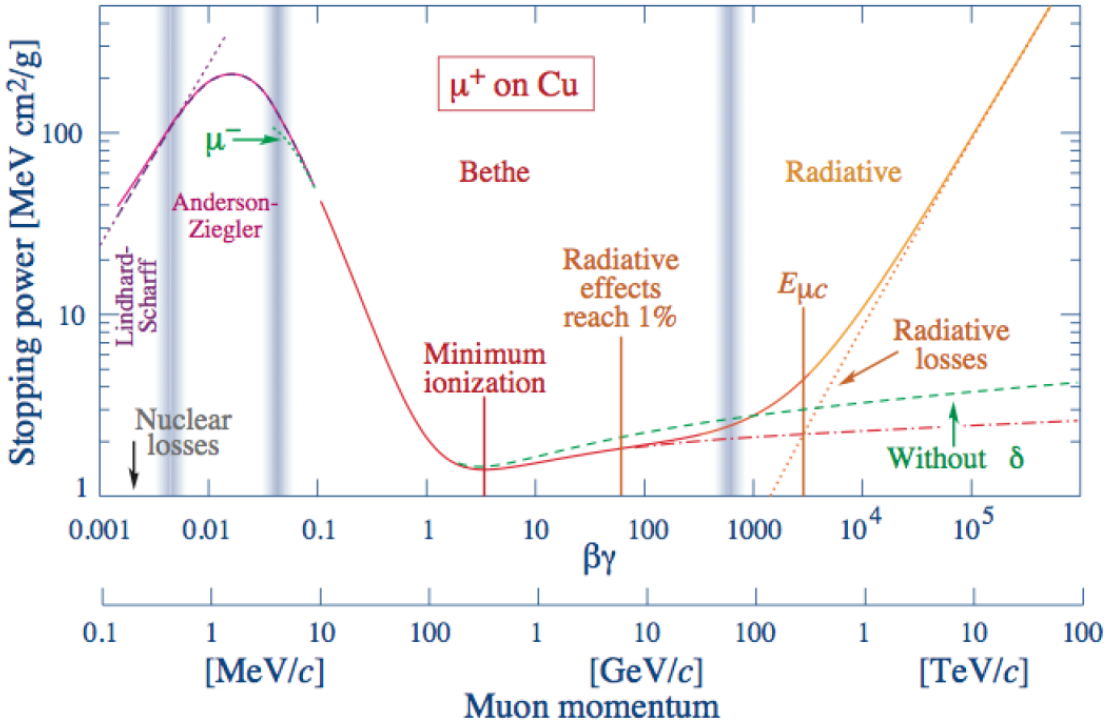

Figure 3.2: Shown is the expectation of muon energy loss in copper for the Bethe-Bloch equation [29].

photon.

- Photo-nuclear interactions - occurring when a particle passing through a material loses energy via inelastic collision with a nucleus in the material.

Figure 3.3, for example, shows the relative contributions of b_{brems}, b_{pair} and b_{nucl} in water.

As the muon energy increases, radiative losses (b) increase in importance; however, this is typically less than 1% of the total average energy loss for energies $E \leq 100$ GeV for the majority of materials [29].

Electrons lose energy primarily through bremsstrahlung radiation, and this may be described by:

$$\left\langle -\frac{1}{\rho}\frac{dE}{dx} \right\rangle = \frac{E}{X_0}, \tag{3.7}$$

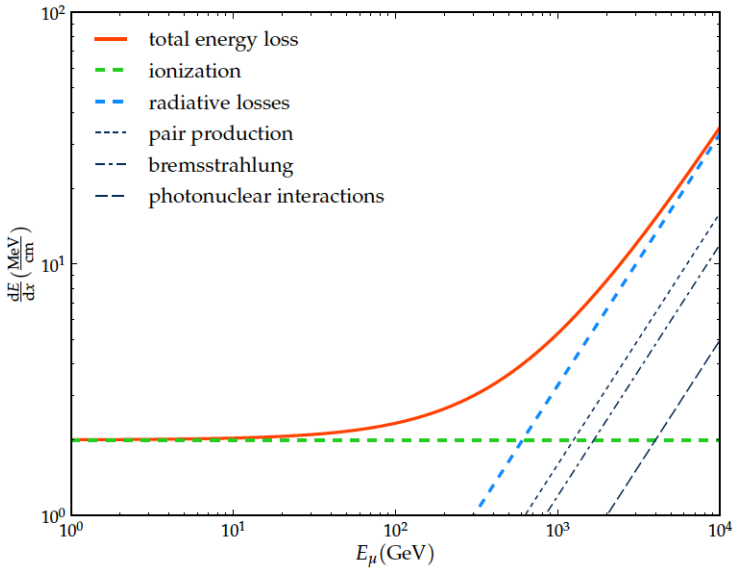

Figure 3.3: The relative contributions of b_{brems}, b_{pair} and b_{nucl} in water [29].

where X_0 is the radiation length. For water or ice $X_0 \approx 36.08$ g/cm^2 [29]. The total energy of the electron is typically lost within 30 cm to a few metres.

3.2.1 Detection Principle of Cherenkov Detectors

Cherenkov detectors detect neutrinos via the charged leptons that result from CC weak interactions and the hadronic showers that result from both neutral (NC) and charged-current (CC) interactions with nucleons in the medium. The important reactions are defined as:

$$\nu_l(\bar{\nu}_l + N) \rightarrow l^-(l^+) + X \qquad \text{(CC)} \tag{3.8}$$

$$\nu_l(\bar{\nu}_l + N) \rightarrow \nu_l(\bar{\nu}_l) + X \qquad \text{(NC)} \tag{3.9}$$

where the resultant general Feynman diagram is shown in Figure 3.4. The neutrino and the interaction type defines the resultant energy deposition in a detector (see

Figure 3.5). The visual topology of these event signatures are distinguishable in water-Cherenkov detectors depending on the detector layout.

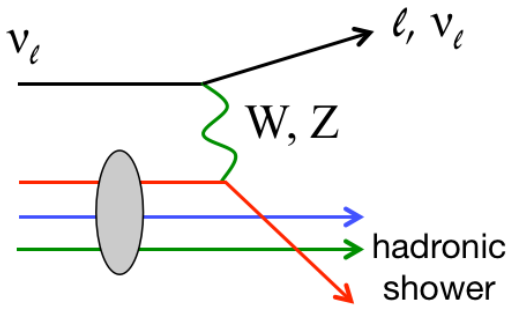

Figure 3.4: Generalized Feynman diagram of CC and NC weak interactions [30]. A neutrino of flavour l exchanges a weak boson with a nucleus, resulting in hadronic shower, a lepton, and neutrino, conserving the lepton number.

Interaction		Secondary particles	Detector signature
CC ν_μ		μ track and hadronic cascade	Track with cascade
CC ν_τ	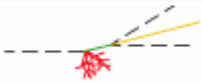	τ decays into μ ($\sim 17\,\%$ b.r.)	
	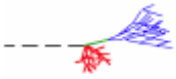	τ decays into e / hadrons	
CC ν_e	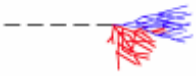	Hadronic and EM cascades	Cascade
NC ν_α		Hadronic cascade	

Figure 3.5: Detector event signatures for the possible neutrino interactions in DeepCore. Figure is taken from [31]. The dashed lines are neutrinos, orange lines are muons, red lines are particles produced in a hadronic shower, and blue lines are particles produced in an electromagnetic shower.

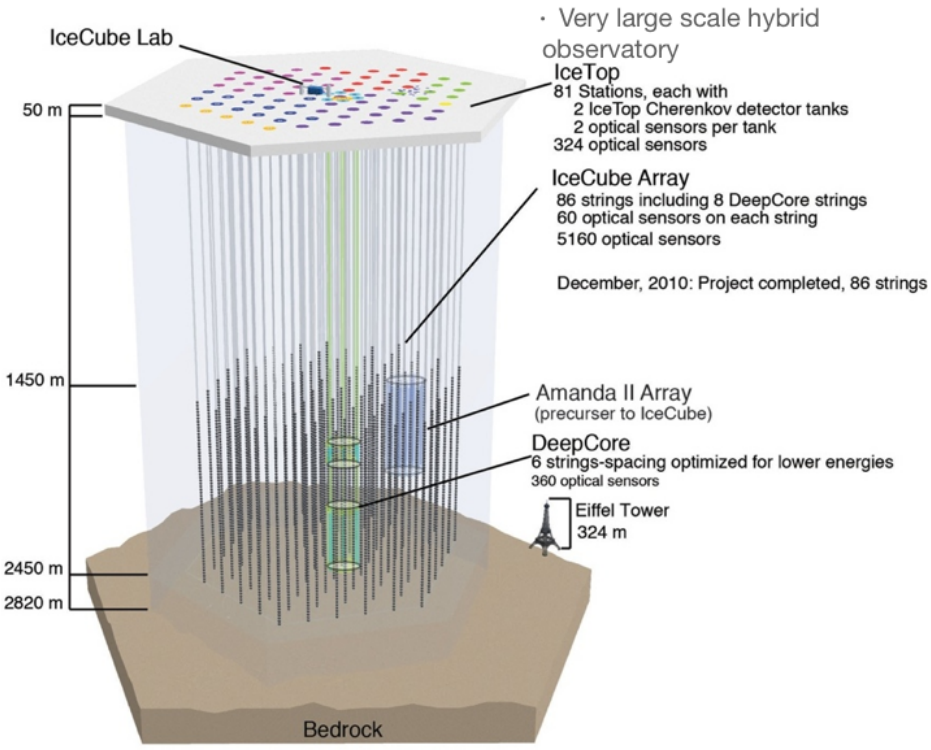

Figure 3.6: Artists image of the IceCube Neutrino Observatory [32]. The IceCube observatory is hybrid detector with a primary in-ice array, a dense infill (DeepCore) for the low-energy science program, and a surface array (IceTop) deployed on the ice over the detector for cosmic ray measurements. With such an instrument one has sensitivity to neutrinos over nine orders of magnitude.

3.3 The IceCube Neutrino Observatory

The IceCube Neutrino Observatory (IceCube) pictured in Figure 3.6 is a frozen water Cherenkov detector located at Amundsen-Scott South Pole Station, Antarctica. IceCube consists of more than a cubic-kilometre of clear glacial ice infilled with PMTs deployed in a hexagonal 3D array (see Figure 3.7). The ice-sheet, which is 3 km deep at South Pole station, is an excellent Cherenkov medium for neutrino detection due to its large accessible volume and pristine optical clarity [33].

The digital optical model (DOM) is the smallest autonomous unit of the IceCube detector (see Figure 3.8) [34] [35]. Each DOM contains one 25 cm PMT (Hamamatsu model R7081-02) and associated electronics, including a main board, a delay board, a

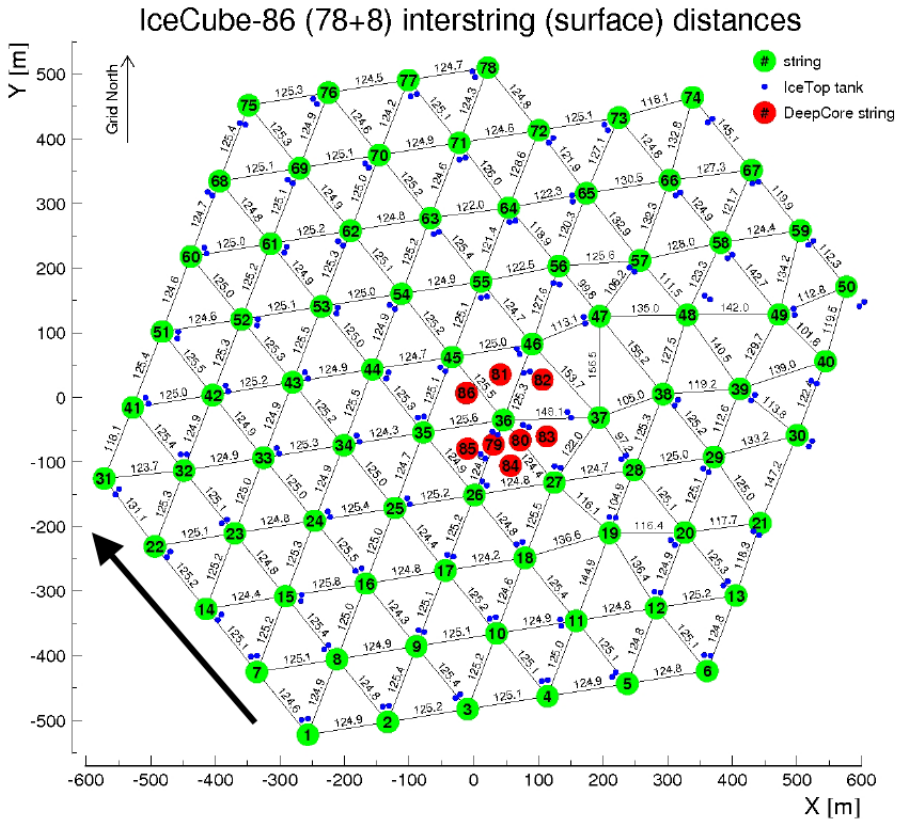

Figure 3.7: Top view of the IceCube neutrino observatory. The green dots represent IceCube main array strings and the red dots represent DeepCore strings [32]. The black arrow shows the direction of the surface flow of the ice sheet.

LED flasher (calibration) board, and a 2 kV high voltage power supply [34] [35]. These components power and control the PMT, as well as provide onboard amplification, filtering and digitization of the signal. The PMT and associated electronics, as well as a mu-metal magnetic shield for the PMT, are housed within a 35.6 cm diameter, 1.3 cm thick pressurize glass sphere; where the PMT is optically coupled to the glass sphere with a silicone gel.

The IceCube hexagonal array is composed of 86 cables or 'strings', each deployed with 60 DOMs per string, for a total of 5160 sensors. The observatory can be divided into three distinct detector elements, each utilizing the same DOM technology. On the surface, is the 'IceTop Array', consisting of 81 ice Cherenkov detector tanks with two DOMs per tank, for a total of 324 sensors. The IceTop Array is optimized for

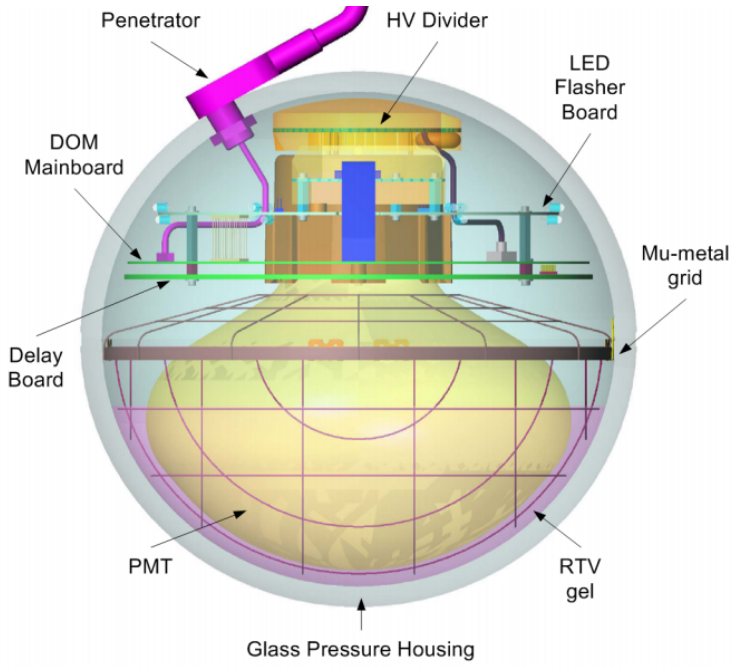

Figure 3.8: The digital optical module (DOM) [34] [35].

measurements of cosmic ray air showers above a few hundred TeV. The IceCube main array is 78-strings deployed ∼1500 m below the ice surface, and extends down to 2520 m. The DOMs in the IceCube main array are vertically spaced 17 m from their neighbours on the same string, and each string of DOMs has a horizontal spacing of 125 m from the next. This array is designed for very high energies (∼100s GeV to EeV scale), with a vast particle and astrophysics scientific program. Finally, the DeepCore array, located at the bottom centre of the detector in the deepest, clearest ice, facilitates IceCube's core particle physics program at energies from ∼ 5 GeV - ∼ 100s GeV, including: atmospheric neutrino oscillations; atmospheric neutrino flux measurements; indirect dark matter; and sterile neutrino searches.

The DeepCore array DOMs utilize high quantum efficiency PMTs with ten of the DeepCore DOMs deployed at depths between 1750 m and 1850 m at 10 m vertical spacing to make a veto 'cap'. The remaining 50 sensors on the DeepCore strings are deployed with 7 m vertical spacing below a depth of 2100 m, where the Antarctic ice is the clearest (see figure 3.9). The horizontal spacing in DeepCore is 72 m instead

of 125 m horizontally.

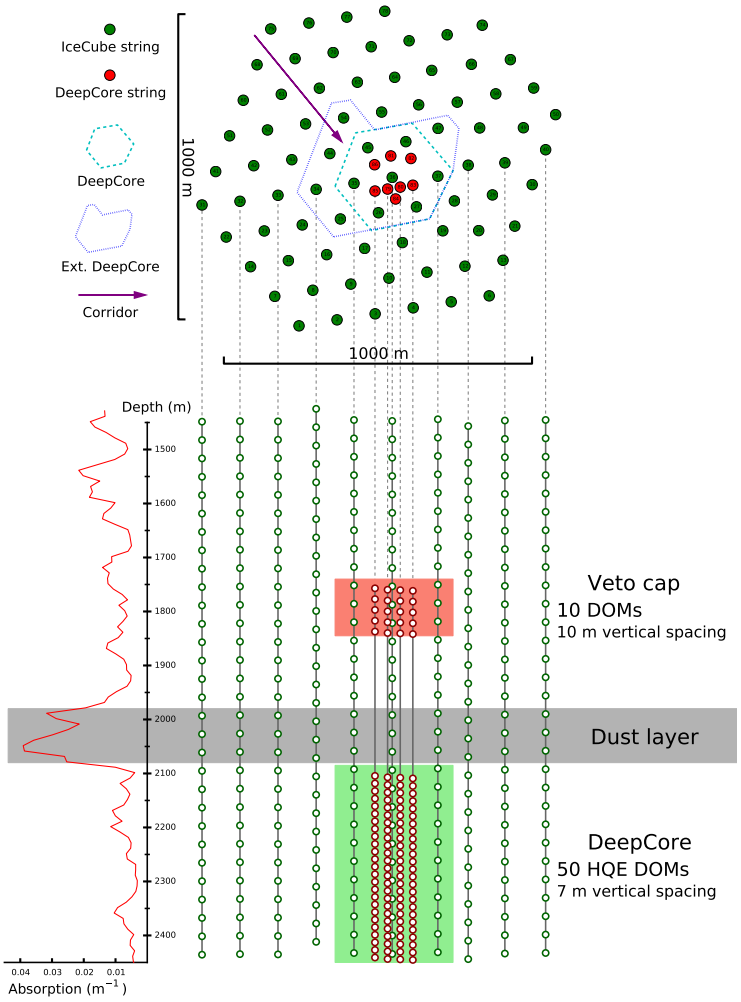

Figure 3.9: Showing the geometry of DeepCore [36] with top and side views of IceCube. Circles indicate the positions of DeepCore DOMs in red and IceCube DOMs in green. The DeepCore DOMs were deployed primarily > 2100 m below the surface (green filled rectangle). A lesser amount of DeepCore DOMs were also deployed $\sim$1800 m below the surface. These DOMs form part of a veto "cap" (red filled rectangle) which aids in rejection of atmospheric muons. The purple arrow in the top view shows an example of a "corridor" path along which dim atmospheric muons may avoid detection due to gaps in the instrumentation. The bottom left panel shows the absorption length (for blue light) vs. depth in the detector. The grey band indicates a dust layer, a region of higher scattering and absorption due to sediment (dust) in the ice present at these depths.

With this 3D array of optical detectors the direction, energy and interaction neutrino type can all be determined. For TeV to EeV events, the charged lepton produced in the neutrino - nucleon interaction is collinear with the interacting neutrino, allowing IceCube to point back to the emission source with $\sim$ one degree accuracy. For events in DeepCore, with typical energies of 30 GeV, the angular resolution is $\approx$ 20 degrees for CC ν_μ events (see Chapter 6.4 for details).

3.3.1 Event Signatures in IceCube

In IceCube, with its uniform detector coverage, CC ν_μ events appear as long tracks; the muons produced are long lived in the lab frame and can deposit light in the detector for hundreds of meters depending on the energy of the event. These resultant muons provide directional as well as kinematic information from the neutrino. In IceCube these are called 'track-like' events (see Figure 3.10). The CC ν_e and NC ν_l events (NC any flavour) produce particle cascades (via hadronic and EM interactions), that appear as a quick burst of light. In IceCube these are called 'cascade-like' events (see Figure 3.11).

These 'cascade-like' type events, effectively appear as low eccentricity ellipses in the detector due to the short distance of travel for the resulting electron before all of its energy is deposited. The CC ν_τ events are characterized by a hadronic cascade at the initial neutrino interaction, a track from the τ lepton, and another cascade from the decay of the τ. This topology may be clearly identified at PeV energies by the distinctive charge deposition and is called a double-bang (see Figure 3.12).

While IceCube cannot directly determine the flavour of a neutrino in a given event, it is possible to separate between track-like (ν_μ CC events) and cascade-like (ν_e CC, ν_τ CC, and all NC events). The topologies of these events are more distinct above 100 TeV then the $\sim$ GeV scale (see Figure 3.13).

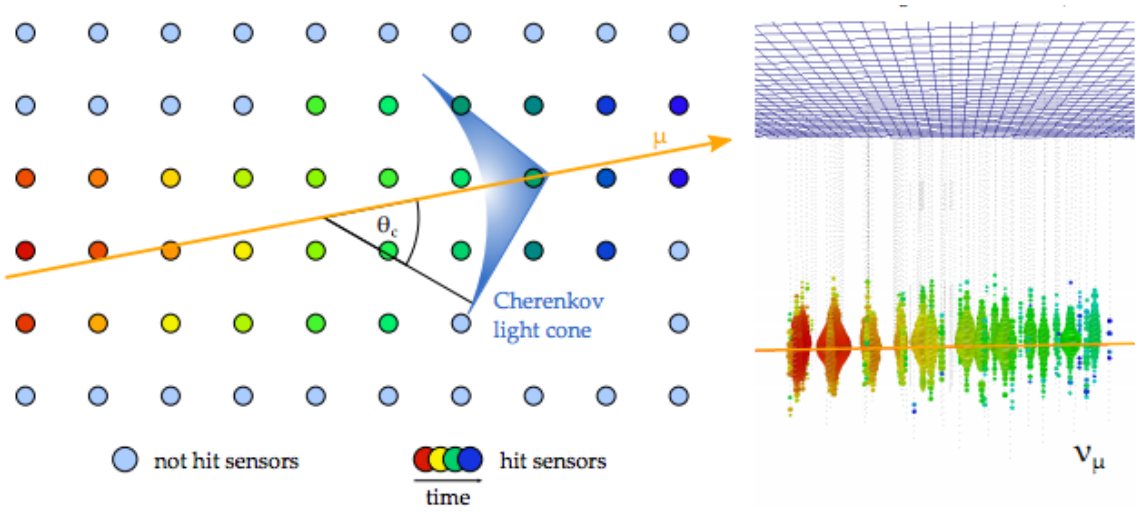

Figure 3.10: An event resulting from a simulated muon neutrino event, or 'track-like' event, is shown on the right, with a pictorial diagram of a photosensor array and a Cherenkov cone shown on the left [37]. The spheres represent IceCube DOMs, where the colouring of the sphere represents the timing of the hit, with red light being earlier and blue later (i.e. the blue light is the most recent). This is the topology that the IceCube detector sees for track-like (ν_μ charged current (CC) events).

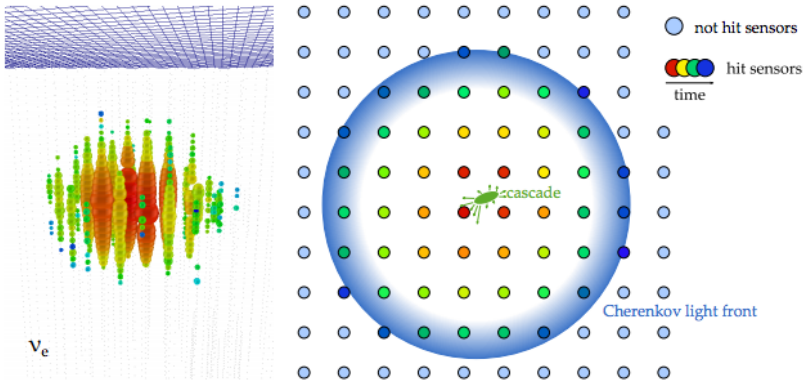

Figure 3.11: Showing a simulated IceCube cascade event is shown on the left and on the right we see a pictorial representation. The spheres represent IceCube DOMs, where the colouring of the sphere represents the timing of the hit, with red light being earlier and blue later (i.e. the blue light is the most recent). This is the topology IceCube detects for cascade-like (ν_e CC, ν_τ-CC, and all neutral current (NC) events) [37].

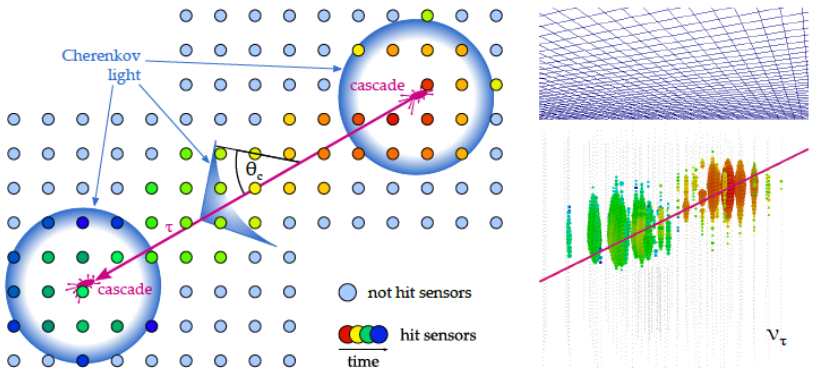

Figure 3.12: A simulated composite ($\nu\tau$) event. The spheres represent IceCube DOMs, where the colouring of the sphere represents the timing of the hit, with red light being earlier and blue later (i.e. the blue light is the most recent). This is the topology IceCube detects for high energy 'tau-like' (double-bang) events.

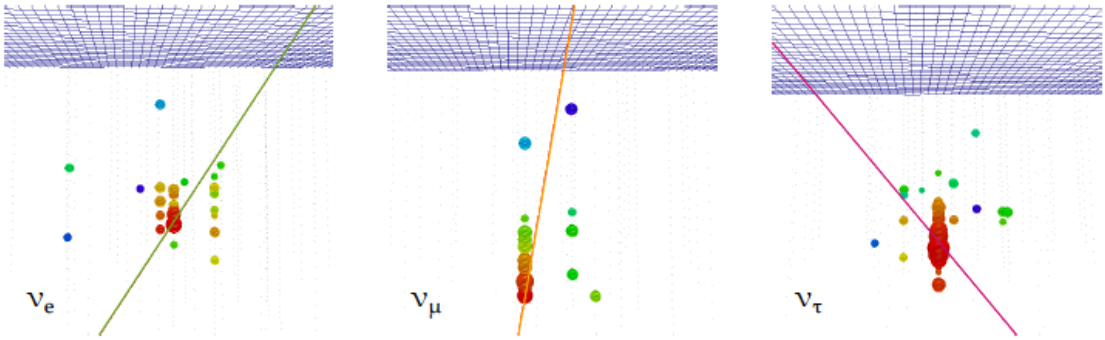

Figure 3.13: An example of event views for low-energy events [37]. Events here have $\approx$ 50 GeV neutrino energy.

3.3.2 Ice Properties

As a natural medium, the properties of the deep glacial ice sheet become a key element of the detector operation. The ice at the South Pole is formed from compressed snow. Each year new layers form and bury older layers. The accumulating pressure causes the lower layers to break down and pack more closely, slowly transitioning into ice. The deep glacier at the bottom of IceCube (~2,500 m) is estimated to be 160,000 years old [38].

The glacial ice is made up of hexagonal crystals and, due to the approximately

isotropic pressure conditions deep in the ice, the ice crystals are formed with random orientation. Thus, although there is some elastic sliding in the basal plane of the crystals, the general flow is plastic and non-Newtonian in nature and basal sliding plays a limited role [39]. This means that although the surface of the glacier is moving at a rate of $\sim$10 m/year [40], the DOMs at depth are expected to be moving very little or not at all.

The optical properties of the glacial ice in which the detector is embedded are described with absorption and effective scattering coefficients describing extracted ice properties in 10 m thick layers. These properties are determined with a dedicated calibration effort performed annually with *in-situ* light emitting diode (LED) flasher measurements. For the creation of the South Pole ice model, all DOMs on string 63 were operated in 'flasher' mode, i.e. set to emit light from the onboard DOM LEDs [41]. This was done in an approximately azimuthally symmetric pattern, which was then observed by the DOMs on the surrounding strings [41]. The optical coefficients of the could then be extracted via a global fit [41].

The ice is found to have an anisotropy, *i.e.* there is a preferred direction of the scattering. The current IceCube ice model (SPICE-LEA - see Figure 3.14) incorporates this effect.

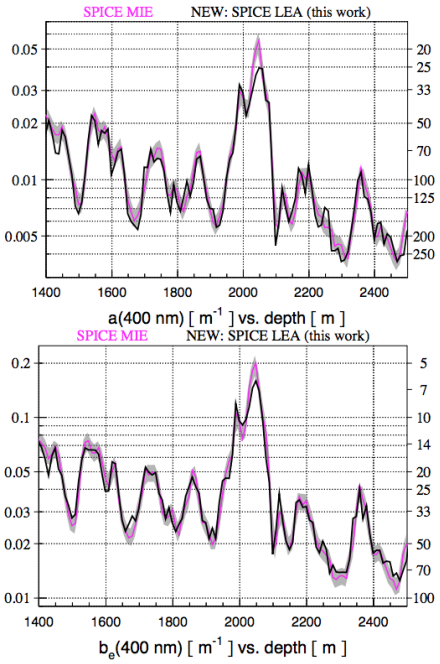

Figure 3.14: Showing the scattering vs depth of a previous ice model (SPICE-MIE) and for the ice model (SPICE-LEA) used in this analysis. For the creation of the South Sole ice (SPICE) LEA model used in this analysis, all DOMs (optical sensors) on string 63 were operated in 'flasher' mode, i.e. set to emit light from onboard LEDs. SPICE-MIE, the previous iteration ice model is also shown.

Chapter 4

IceCube Data Handling and Event Selection

Here we briefly outline the data acquisition process for the IceCube neutrino observatory. The triggers and filters as they apply to the data sample selection for the analysis considered in this work are described. The Chapter concludes with an overview for the final event-level data sample.

4.1 Data Acquisition

IceCube's data taking is subdivided in to runs with a duration of up to 8 hours. In addition to physics quality data taking, the runs may be used to test new firmware, check noise rates, or flash the LEDs onboard the DOMs for calibration runs. In the physics data runs the detector has a raw data rate of 3000 Hz, most of which are from atmospheric muons; this gives an approximate signal to background ratio of $1 : 10^6$ in our detector [36]. Given this, the detector cannot be read out continuously, and an event has to fulfill one of several trigger conditions in order to be recorded (see section 4.1.1).

In a recorded event, a DOM with a measurable signal is called a 'hit'. A hit on a given DOM is stored when the measured charge exceeds a threshold of 0.25 photo-electrons [32]. The full waveform from the onboard electronics is only stored when there are (at minimum) two other adjacent DOM with a hit recorded within 1 μs. This condition is called a Hard Local Coincidence or (HLC) hit, and is in place to reduce the overall data volume from spurious noise in a given DOM. The signals on all of the DOMs are then digitized, collected and processed in the IceCube Lab located on the ice surface and sent to the north for further analysis. IceCube also keeps limited information for so called Soft Local Coincidence (SLC) hits; isolated hits that are much more likely to be caused by PMT noise. For these events, a time stamp and the bin from the waveform with the highest amplitude, and the immediate neighbours of that bin, are stored.

4.1.1 IceCube Trigger Conditions and Filters

The low-temperature of the instrumented ice sheet generally reduces the thermal PMT noise component of the DOMS, giving a relatively low average noise rate of $\sim$650 Hz in the high quantum efficiency (HQE) DOMs, which are mainly placed on DeepCore strings, and an average noise rate of $\sim$540 Hz for standard QE DOMs. In IceCube, the dominant sources of noise are: thermal produced from the internal components of the PMT; and from the decay of radioisotopes in the glass of the DOM pressure housing. Given this noise rate, in addition to the local coincidence conditions discussed above, a number of pre-defined triggers are applied to the raw data. The two primarily considered for the analysis presented here are based simple multiplicity (SMT) hits in the defined active detector region:

- Simple Multiplicity Trigger (SMT8)

  This is the IceCube detector's main trigger condition, having a threshold of 8 hits within a time interval of 5 microseconds. The trigger requires that all hits above threshold be HLC.

- Simple Multiplicity Trigger (SMT3)

  For the detection of low-energy events, a lower trigger threshold of 3 HLC hits (2.5 μs window) is applied in the DeepCore active detection region; defined as the lower 50 DOMs of DeepCore strings and the lower 22 DOMs of the seven IceCube main array strings in and around the DeepCore array (see Figure 3.9).

Beyond the trigger conditions, decisions to send data in real time to the north via satellite for analysis are made with dedicated filter algorithms. Here we describe in detail the DeepCore Filter that is employed for the data in this analysis. The filter is optimized for neutrino events. It is applied online during data taking and is considered the first stage in event selection.

In a typical IceCube event (travelling 1000 m,with a time length of 3 μs and a readout window of 10 μs), the HLC hits are noise free, where as $\sim$90% of the SLC hits in the same time window are due to noise hits [42]. However, since low-energy events (below 100 GeV) typically produce relatively few hits, it is often the case that the information from the HLC hits alone is not sufficient to provide a good reconstruction. SLC hits are therefore used to provide the information needed to reconstruct this event set and are used directly in the DeepCore filter algorithm:

- For every event, the filter estimates the center of gravity (COG) of the hits inside DeepCore (see figure 4.1) by calculating the average position and time of all hits. This provides a first guess vertex position (x,y,z) and time (t) for an event.

- A second pass calculation considers only those hits within one standard deviation of the previously estimated average times, providing a new estimate of the position of the vertex (x, y, z) of the event in the detector, called $\vec{r}_{COG}$.

- A refined time estimate is also calculated, called t_{COG}, that is the average of the 'corrected hit times' (time residual) for the event. This is calculated by subtracting the time it would take for direct (un-scattered) light to travel from

r_{COG} to a given hit, from the recorded time of the hit.

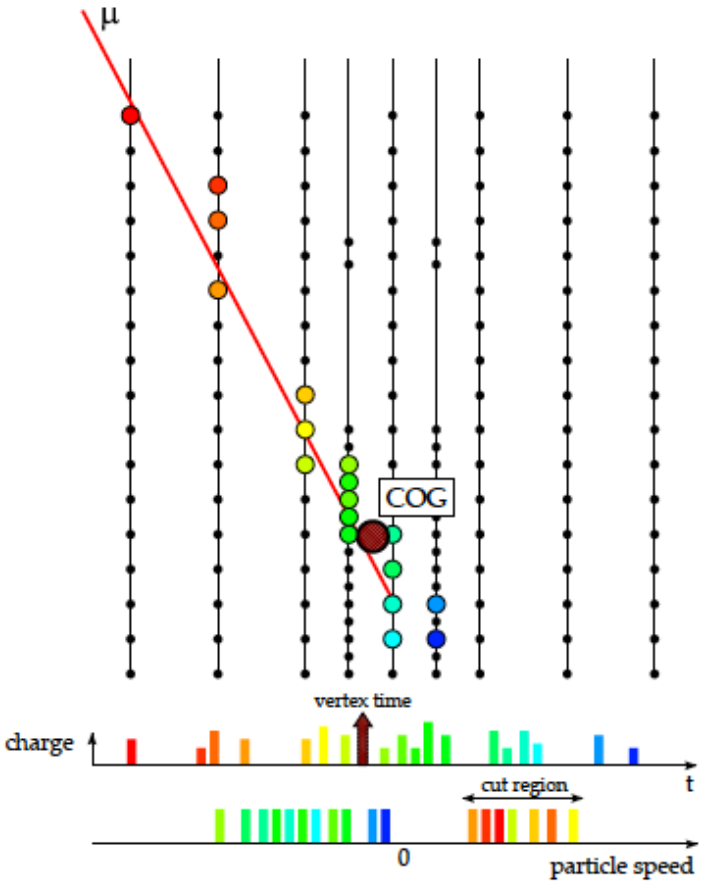

Figure 4.1: Showing an artist impression of the DeepCore filter principle [28]. Pictured are two DeepCore strings with an IceCube standard string in the centre, surrounded by IceCube standard strings. The coloured dots represent the time that a hit occurred, with red being early and blue being later with respect to the vertex time, as shown on the upper axis. The lower axis shows the calculated particle speed and the cut region, that is selected for high speeds and early light. Particle speeds between 0.25 m/ns and 0.4 m/ns are rejected.

- Relative to the COG, a particle speed (v) is calculated for all hits outside the DeepCore volume,

$$v = \frac{|\vec{r}_{COG} - \vec{r}_{hit}|}{|t_{COG} - t_{hit}|}. \tag{4.1}$$

From this definition, positive particle speeds are associated with hits before the COG, *e.g.* the hits produced by an incoming muon will have positive particle

speeds with typical values of v = 0.3 m/ns. To remove atmospheric muons, all events with at least one hit with a particle speed between 0.25 m/ns and 0.4 m/ns are rejected (see figure 4.1).

Applying the filter particle velocity rejection criteria above, the DeepCore filter reduces the data rate from 185 Hz (the SMT3 trigger rate) to 17.5 Hz, achieving a background rejection of one order of magnitude while keeping about 99.4% of the neutrino-induced events [36].

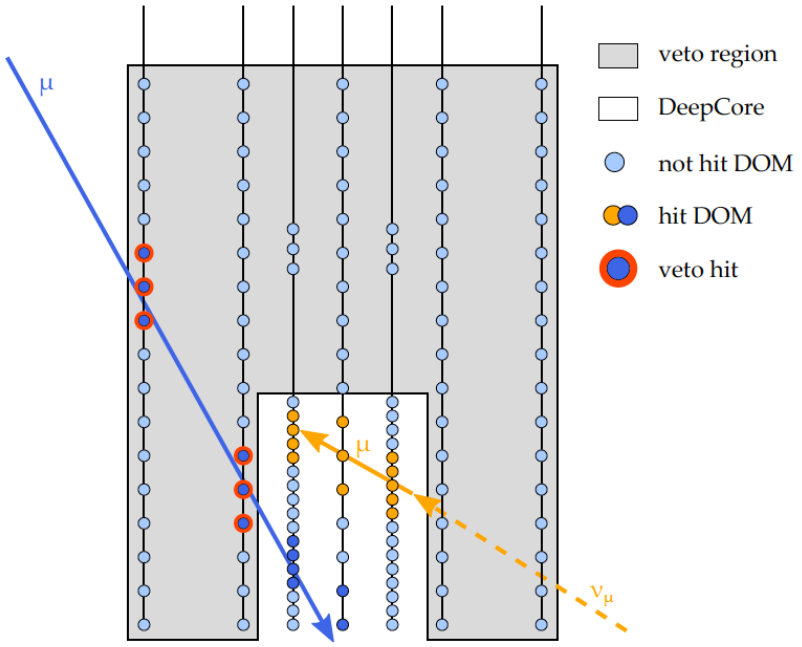

Figure 4.2: Atmospheric muons lose energy from their point of creation until their point of absorption. This means they must be created outside the detector and already be emitting light when they enter the active detector volume. In contrast, a muon induced neutrino will seem to suddenly appear in the detector volume. In such an event (the signal!) a neutrino (which gives off no light in the ice) travels into the detector and IceCube detects the light from the interaction that produced the muon and then from the muon as it traverses the ice emitting Cherenkov radiation.

4.1.2 DeepCore Veto

The next steps in the data selection uses an active *in-situ* veto technique that subdivides the detector into veto and fiducial regions (see Figures 3.9 4.2). As previously discussed, the fiducial region of DeepCore utilizes the SMT3 trigger on the 50 DOMS below the dust later on the six dedicated DeepCore strings and the seven interspersed IceCube main array strings (see Figure 3.9 side view). The remainder of the in-ice detector array (all outer strings and the top 10 DOMs of DeepCore strings) form the veto region. The veto has a threshold condition of one SLC hit. In order to ensure efficient background rejection, hit cleaning on noise events is crucial.

As noted, in a given event that passes a trigger condition, a large number of the SLC hits in that event may arise from noise. When the number of noise hits is similar to or greater than the number of physics hits, hit cleaning is required to ensure quality reconstructions. A hit cleaning algorithm must be balanced between having too strict cleaning, removing too many physics hits, and too relaxed cleaning, keeping too many noise hits. This step is particularly critical when using the SMT3 trigger in combination with the atmospheric muon veto due the high amount of noise events in the SLC hits.

The collaboration has developed two noise cleaning algorithms outlined below:

- classicRT cleaning:

  This cleaning algorithm is applied to the veto region. It leaves HLC hits untouched, considering only the SLC hits to determine if a second hit (SLC or HLC) is located within a radius R = 150 m and a time difference T = 100 ns. The hit is discarded if the condition is not satisfied. This cleaning keeps about 96% of the physics hits, and about 18% of the noise hits [36].

- seededRT cleaning:

  This hit cleaning iteratively checks for nearby SLC and HLC hits. Instead of simply removing hits that do not fulfill the RT-criterion, this algorithm starts

with a seed of hits (typically the result of the classicRT cleaning algorithm) that are already believed to be physics hits, and then adds nearby hits fulfilling the RT-criterion. This subset of hits is kept and is then used as seed for the next iteration. When no more hits can be added, or the chosen number of iterations is reached, all other hits are discarded. This approach is more effective than the classicRT cleaning: it discards all but 3% of the noise hits, and keeps almost 92% of the physics hits [37]. The seededRT-cleaned subsets of hits are then used for the initial directional reconstructions.

Remaining muon background

The remaining muon background is challenging to remove. As shown in Figure 3.9, DeepCore strings are slightly offset from the IceCube main strings. This allows us to infill a greater volume with fewer strings but also introduces a new challenge; corridors where there is little to no instrumentation, creating blind spots in the detector where a muon can travel undetected. These dim events can leave strong signal in the DeepCore fiducial volume, mimicking a signal event. To solve this problem, a search for isolated pulses from these blind directions, named the corridor cut, was introduced in [43]. The corridor cut starts by identifying the DeepCore string with the largest deposited charge. The arrival time and vertical location of the charge is used to point back along a hypothetical track. This track is fixed in z (vertical position) but rotated around its azimuth and zenith directions through the blind corridors. DOMs that contain a causal hit on this track are summed; if two or more are found, the event is flagged and removed from the analysis. These background events are then processed to the final analysis level and used as a background estimate template, which we call the 'inverted corridor cut' (icc) (see figure 7.5).

Due to the success of our atmospheric muon rejection algorithms, a daunting amount of computing power would be required to produce a statistically significant final sample of simulated atmospheric muon events that pass all selection criteria. Therefore,

for the final analysis computation, the data-driven method described above is used to estimate the shape of the remaining background atmospheric muons and to assess the full impact of the muon background. This method applies a normalization factor to the data-driven muon template and this factor is allowed to float in the fit (see section 7.2).

4.2 High-level Event Selection

The selection of a final physics event sample is implemented in a series of cuts or 'levels' that sequentially improve the single-to-background ratio. The analysis presented here, utilizes six cut levels. The first three levels are generally common to all DeepCore analyses and are unchanged here (see Appendix C.1 for details).

Beyond level 3, the sample has been refined for an oscillation analysis, where ν_μ events were the signal of interest [31] [3]. This is reflected in cut levels 3-5, which remain unchanged here (see Appendix C.1, C.3 - C.5). Specifically for this analysis, changes were introduced to the existing selection criteria at the final level (L6) (see Appendix C.6). Here, the sample maintains the events in the energy range between 56 GeV – 180 GeV in reconstructed neutrino energy.

In addition, a stopping containment cut was relaxed to retain more events above ∼56 GeV. Table 4.1 shows the resultant event rates of the sample through each selection level. The neutrino rates are the combination of the NC+CC channels and use the atmospheric neutrino flux predictions from [5] with global best fit values for the oscillation parameters. At the final level, the rate of atmospheric muons is reduced by a factor of $\sim 10^8$, and neutrino events contribute to $\sim 95\%$ of the sample with a final level neutrino event rate of 0.5 mHz.

A full verification of this final extended data sample was then preformed via cross checks with the MC simulation, and discussed in the next chapter.

Type	Filtering		Analysis				
	Total	DeepCore	L3	L4	L5	L6	L6 LE
atm. μ	991000	9180	1310	44.7	0.163	0.0297	0.0259
Noise	35900	8120					<0.0006
ν_e	1.84	1.72	1.29	0.278	0.180	0.149	0.126
ν_μ	11.3	6.36	4.93	1.02	0.558	0.396	0.342
ν_τ	0.293	0.270	0.210	0.052	0.038	0.031	0.028
MC Total	1030000	17300	1320	45.8	0.939	0.605	0.522
Data	1150000	19100	1280	39.6	0.845	0.504	0.432

Table 4.1: The event rate in mHz for the common filtering and the subsequent event selection levels [3] for the analysis.

Chapter 5

MC Generation and Checks on the Final Sample

The analysis presented in this thesis ultimately relies on a comparison of experimental to simulated data. The data selection, described in the previous chapter, was primarily developed with simulated data. An accurate simulation of the physics interaction and detector response is therefore key. In this chapter we briefly describe the IceCube Monte Carlo (MC) simulation chain. We then describe in detail the verification steps for selecting the energy range of the extended (L6) data sample utilizing the full MC.

5.1 Signal and Background Simulation

Neutrino interactions and hadronization processes are simulated by GENIE [45]; using a combination of theoretical predictions and tuning to match experimental data. Resultant muons from the neutrino interaction are then propagated with PROPOSAL [46]. For hadrons and the particles producing electromagnetic showers, with energies up to 1 TeV, simulation is performed with GENIE and propagation with

GEANT4 [47]. Particles with higher energies utilize propagating templates developed by the IceCube collaboration [48]. The photon propagation code Clsim [49] is used to simulate the process of the resulting photons. For the photons intersecting a DOM, the acceptance in terms of arrival angle and wavelength is considered, including a measure of the relative variation of the optical efficiency. Hits caused by thermal noise, decaying radioactive isotopes in the PMT and DOM glass, and scintillation are also added. Finally, the PMT response and readout electronics are simulated and trigger algorithms are applied across the full detector in order to produce simulated neutrino events. A total of 30 years of detector operation livetime is simulated for each neutrino flavour, ensuring that the Poisson fluctuations due to the Monte Carlo statistics are much smaller than statistical uncertainties in the data.

For consideration of the principle backgrounds in this analysis (the rejection algorithms for atmospheric muons described in the previous chapter) were developed using MC simulations produced with CORSIKA [50]. The resultant muons are then propagated with PROPOSAL [46], just as for signal muons, and follow the full simulation chain described above.

5.2 Simulation Verification of the Extended L6 Data Sample

The original oscillation analysis for which this data sample was developed was limited to events below 56 GeV due to restrictions in the legacy simulation available [51] [3]. The existing GENIE simulation used in this analysis reaches the 1 TeV scale, permitting an extension to the energy range of the sample. In addition, the L6 stopping containment cut (see Appendix C.6) was removed in order to retain the signal events above 56 GeV. The upper limit of the extended data sample range is derived from the simulation set below.

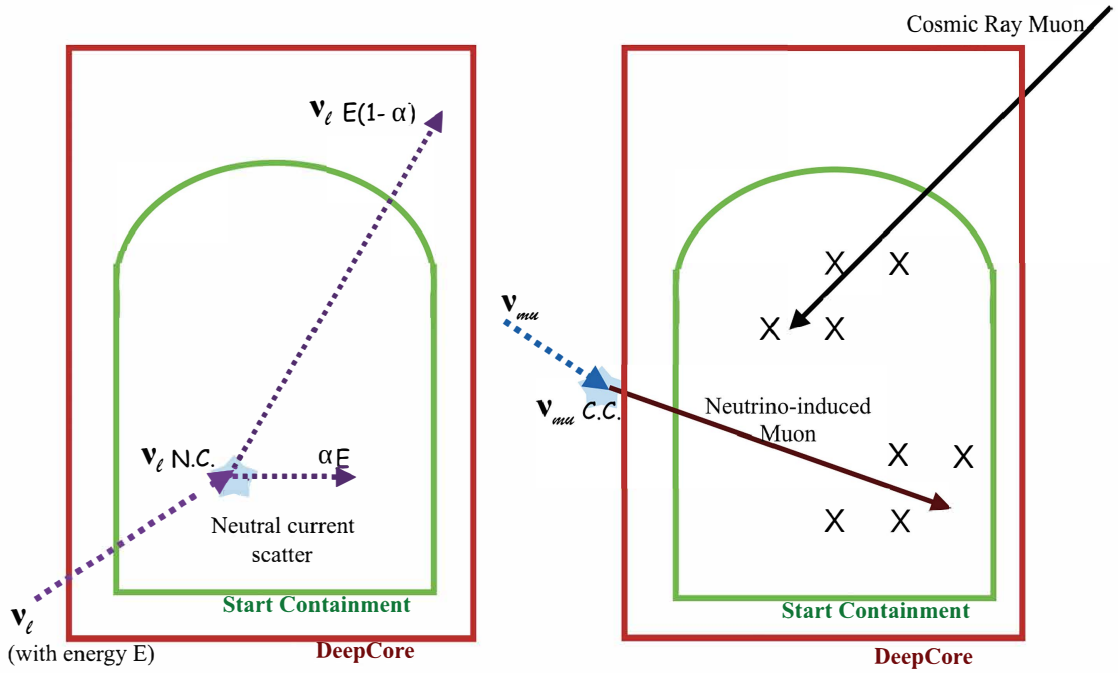

Figure 5.1: (Left) A NC scatter event, any lepton flavour (l), taking place in the start containment region. (Right) A CC ν_μ event that appears to start (interact) inside the containment region and therefore is accepted into the analysis data sample.

5.2.1 Potential Leakage of High Energy Events into Sample

The extension of the data sample (for the applied event selection beyond 56 GeV reconstructed energy) required a method to determine the upper limit for the analysis.

It is possible that events above 1 TeV may "leak" into the lower energy region of the data sample. Such events include: NC event interactions and CC ν_μ events that have entered into the containment region undetected (see figure 5.1). NC events arising from high-energy neutrinos can appear to be a lower energy event when some of their light is emitted in a NC scatter. For CC ν_μ events, much like a background atmospheric muon, it is possible they may enter the containment region undetected and

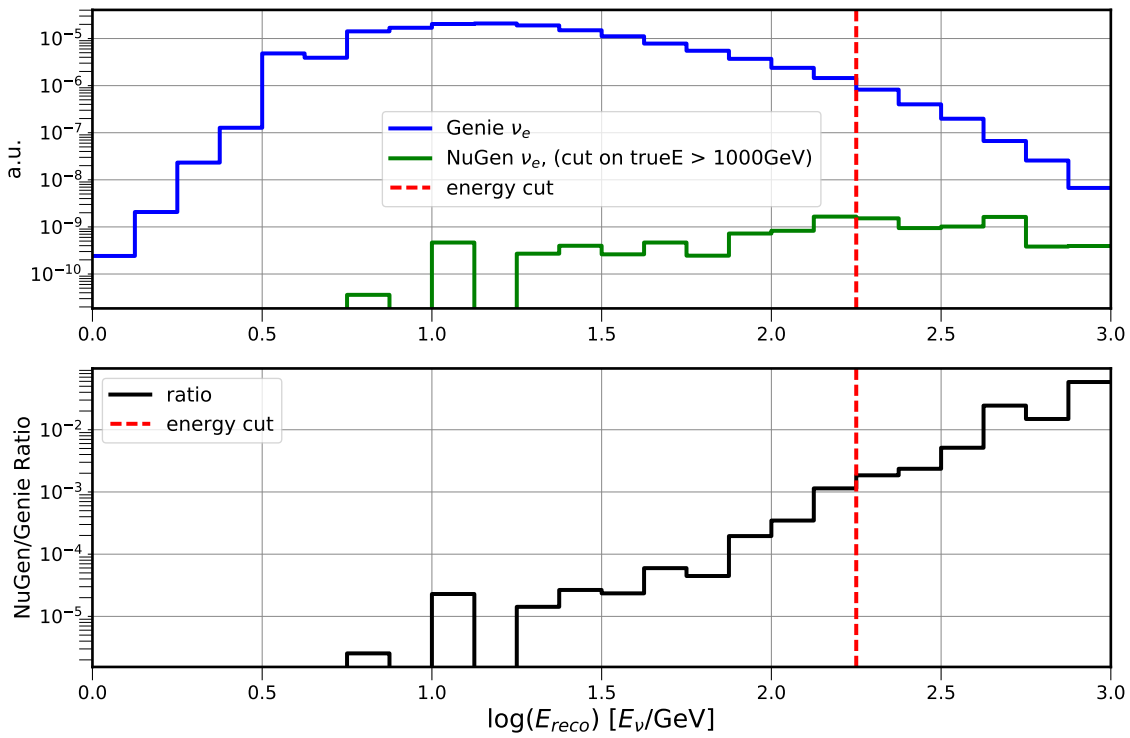

Figure 5.2: (Top) Showing the energy distribution for reconstructed ν_e MC events. The events from the simulation used in this analysis (GENIE) are shown in blue, that from NuGen in green. The NuGen simulation shown has a cut applied demanding true neutrino energy be greater than 1000 GeV; therefore the events that remain and are shown on the plot (with reconstructed energy below 1000 GeV). These events would not be simulated in GENIE, as those sets reach only to 1000 GeV. These NuGen events, therefore, represent those that should be in our sample but are not simulated directly. This rate needs to be kept low and restricts the reconstructed energy range of the sample when using only GENIE simulation. (Bottom) The ratio of the reconstructed NuGen events over the GENIE situation. We apply a cut at $\log(E_{reco}) = 2.25$ ($\sim$ 180 GeV) so as to have 2% or less uncertainty in high-energy event leakage rate from this potential source of error.

mimic a neutrino event for this analysis. For example, a CC neutrino-induced-muon of a higher energy can sometimes find a "corridor" in the detector (see Figure 3.9) or enter through the dust layer or have late initial light detected.

We use a set of higher energy events from NuGen [52], processed through the regular analysis chain, to address potential leakage of events beyond 1 TeV. The simulated events passing the extended L6 selection are histograms to evaluate the potential

leakage (see Figure 5.2 and Figure 5.3).

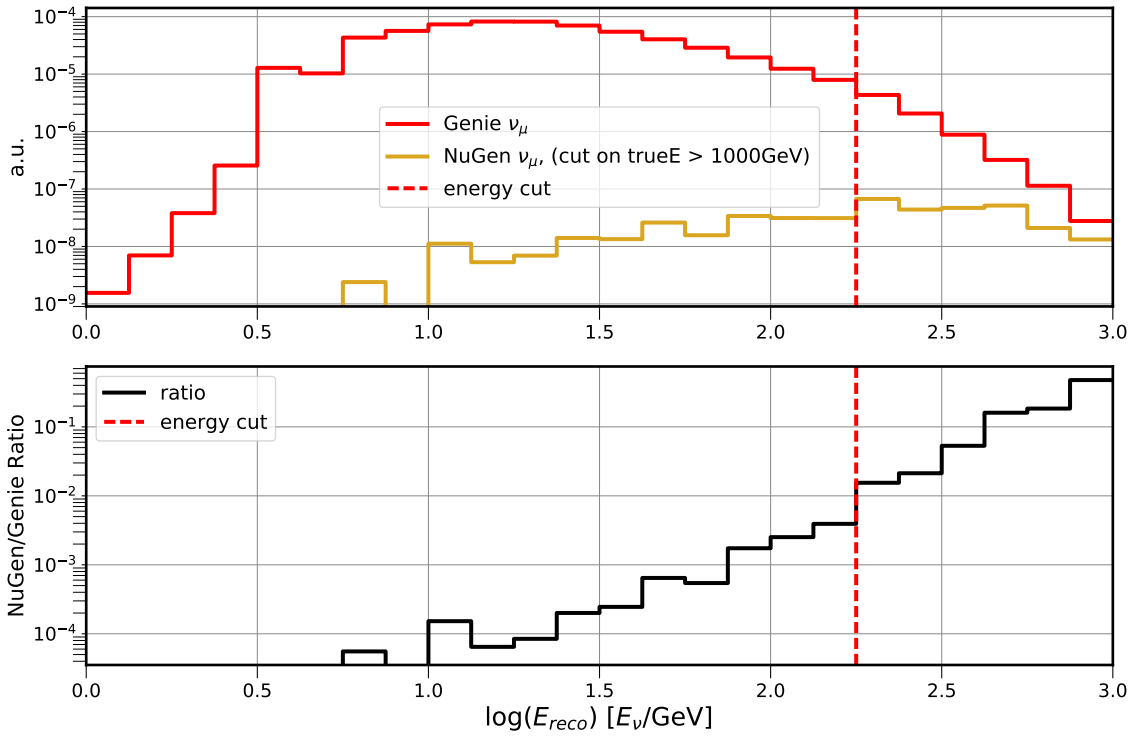

Figure 5.3: (Top) Showing the energy distribution for reconstructed ν_μ MC events. The events from the simulation used in this analysis (GENIE) are shown in red, that from NuGen in yellow. The NuGen simulation shown has a cut applied demanding true neutrino energy be greater than 1000 GeV; therefore the events that remain and are shown on the plot (with reconstructed energy below 1000 GeV). These events would not be simulated in GENIE, as those sets reach only to 1000 GeV. These NuGen events, therefore, represent those that should be in our sample but are not simulated directly. This rate needs to be kept low and restricts the reconstructed energy range of the sample when using only GENIE simulation. (Bottom) The ratio of the reconstructed NuGen events over the GENIE situation. We apply a cut at $\log(E_{reco}) = 2.25$ ($\sim$ 180 GeV) so as to have 2% or less uncertainty in high-energy event leakage rate from this potential source of error.

We chose our sample energy range to be log[0.75,2.25], *i.e.* $\sim 6 - 180$ GeV. In this range there we expect 2% or less potential rate error from unstimulated events.

Chapter 6

Measurement of the Atmospheric Neutrino Flux

This chapter begins with a discussion of the detector livetime used in this analysis and then details the energy and direction reconstructions applied to the sample. The event classification algorithm (known as a particle identification or PID) is introduced and the data sample is separated into particle flavour type. The chapter concludes with a discussion of the analysis binning in reconstructed energy and reconstruction direction (zenith), and the event distributions are shown.

6.1 Livetime

Although the IceCube detector has $> 99\%$ livetime, not all of those runs are useful in this analysis. In order for a run to be considered good in the context of this analysis, a run must meet the following criteria:

Good Runs:

Run livetime $\geq$ 1 hour

Active strings = 86

Active DOMs $\geq$ 5380

These requirements result in approximately 90% detector good livetime over the three year period of the considered data set. Please see the Table 6.1 for details of data considered in this analysis.

Table 6.1: Data Sample Detector Livetime

IceCube Analysis Year	Livetime (s)	Fraction of nominal year [%]
IC86-2012 (starting May 2011)	2.80×10^7	89
IC86-2013 (starting May 2012)	2.96×10^7	94
IC86-2014 (starting May 2013)	3.07×10^7	97

This gives a total of 8.83×10^7 s (using IC86-2 to 4) = 2.799(9) years using IC86-2012 - IC86-2014.

6.1.1 Livetime Correction: Coincident Events

It is possible for a muon event to occur during a neutrino event window. Once the event has triggered the detector, the muon may also be recorded. A toy Monte Carlo was created for this analysis to determine the rate at which this might occur, providing an upper limit on coincident events expected in the sample. If we assume muon rate of 3 kHz (related to the detector trigger rate) and use the DeepCore filter trigger time window and average rate over the analysis years, at the lowest analysis level we can expect $\sim$2.8% of the events to have coincident muons in the event information. Conservatively rounding this up to 3%, this is 0.0837 years of our livetime. Assuming that these events are successfully removed by higher level cuts, the resultant livetime is 2.799997 livetime - 0.08367 $\approxeq$ 2.70 years livetime used in this analysis.

At the time of the analysis only limited coincident particle simulation existed; (the GENIE simulation used by DeepCore analyses does not contain coincident events. It was therefore not possible to directly determine how many coincident events survive to the final analysis level of the sample, contributing on uncertainty in the livetime.

With the final event sample set in hand, the next step is to evaluate the event-wise information in terms of physical parameters via reconstructions.

6.2 Event Reconstruction

The event reconstruction used the analysis is a likelihood based method. It compares the observed pattern of hits (photon counts) from all active DOMs in an event to that of a given hypothesis [53]. The detection of photons is by nature a discrete process. As such, the comparison is based on Poisson statistics. The predicted number of photons in each DOM depends on the properties of the particle interaction of the hypothesis, where the hypothesis applied consists of a cascade aligned at the primary vertex and a finite, minimum-ionizing track. This hypothesis can described by eight parameters: the particle in-ice interaction vertex position and time (x, y, z, t), the direction of the neutrino (given by the zenith angle θ_{zen} and the azimuth angle ϕ), the energy of the primary cascade, E_{cscd}, and the length of the minimum ionizing muon track, L_μ.

The minimum ionizing track hypothesis is discretized into constant length segments to reduce computational burden. The primary cascade energy and the muon track segments are treated as independent energy depositions along the path of the muon. The expected charge, μ_i, in each DOM i is estimated with

$$\mu_i = \Lambda_i^{cscd} \cdot E_{cscd} + \sum_j^{N_{\text{seg}}} \Lambda_{ij}^{track} + n_i, \tag{6.1}$$

where E_{cscd} is the energy deposition in the primary cascade, N_{seg} is the number of track segments obtained for a given length of the finite track L_μ and n_i describes the residual expected uncorrelated noise in the DOMs. A linear relation is assumed between deposited cascade energy and observed charge. The track length L_μ can is linked to the energy of the track as follows: $E_{\text{track}} = L_\mu \frac{\mathrm{d}E\mu}{\mathrm{d}x}$, where $\frac{\mathrm{d}E\mu}{\mathrm{d}x} \approx 0.22\,\text{GeV/m}$

is the expected differential energy loss of a minimum ionizing particle (MIP) in ice. The Λ terms in Eq. 6.1 estimate the expected charge due to Cherenkov photons and depend on the hypothesis and the optical properties of the ice. These constants take into account the cascade or track segment location and direction, as well as the optical effects from scattering and absorption. Large tables of pre-computed Λ values for all possible configurations were obtained from full-detector simulations, including the depth-dependent optical properties of the ice and the DOMs' angular acceptance.

Finding the maximum likelihood hypothesis for an event is an optimization problem with eight dimensions. The likelihood space often contains local minima and is not smooth. The MultiNest algorithm [54] is used to find the global minimum to contend with these challenges. The resultant resolutions for the key observables in this analysis ($\cos\theta_{zen}$ and energy) are shown in section 6.4.

6.3 Event Classification (Particle Identification)

In this analysis energy range, DeepCore can distinguish events most events with tracks from those without. A track-like event topology is generally produced by a CC ν_μ interaction with a sufficiently energetic daughter muon that deposits Cherenkov light uniformly along most of its trajectory. Other neutrino interactions typically do not produce distinguishable muons. The Cherenkov light that these interactions produce arises from numerous charged particles created in electromagnetic and hadronic showers at the interaction vertex. The resulting cascade-like topology has a Cherenkov light pattern that is more localized and isotropic (but nevertheless retains directional information from the parent neutrino). Essentially all NC and CC ν_e interactions produce cascade-like events.

To decide if an event is cascade-like or track-like, an additional reconstruction is performed with the track length forced to zero, and the log-likelihood ratio of the cascade-and-track to the cascade-only reconstruction, $\Delta \log \mathcal{L}_{\text{reco}}$, is used. Events

with $\Delta \log \mathcal{L}_{\text{reco}} > 2$ are classified as track-like, while events with $-3 < \Delta \log \mathcal{L}_{\text{reco}} < 2$ are classified as cascade-like (see [31] for further details).

Applying the PID to the extended sample in MC provides the breakdown of events into the following categories (see Table 6.2).

Table 6.2: Event flavour breakdown from the reconstructed PID application to the dataset.

	PID cascade-like	PID track-like	Total
Number ν_μ CC	15 204	15 513	30 718
Num. ν_e CC	7 256	2 284	9 550
Num. ν_τ CC	1 247	472	1 719
Num. all NC	3 386	1 139	4 525

In Tables 6.3 and 6.4, the fraction of events identified as track-like and cascade-like (including the mis-identification) are shown, respectively. Figures 6.1 and 6.2 show the energy distribution of the same MC event set as identified by the PID algorithms for the true and reconstructed neutrino energy, respectively.

Table 6.3: Event flavour breakdown percentage for track-like events

Track-like purity breakdown:	[%]
Percent Events of PID track-like that are actually ν_μ	79.9 %
Percent Events mis-identified as 'track-like'	20.1 %

Table 6.4: Event flavour breakdown percentage for cascade-like events

Cascade-like purity breakdown	[%]
Percent Events of PID cascade-like that are ν_e CC + All NC	39.3 %
Percent Events mis-identified as 'cascade-like'	60.7%

Note, in Table 6.4 the percent PID cascade-like that are CC ν_e is 71.8% (of those correctly identified as 'cascade-like').

Tables 6.2, 6.3, 6.4 show the sample averages and figures 6.1 and 6.2 for the fraction of events by true and reconstructed neutrino energy distributions.

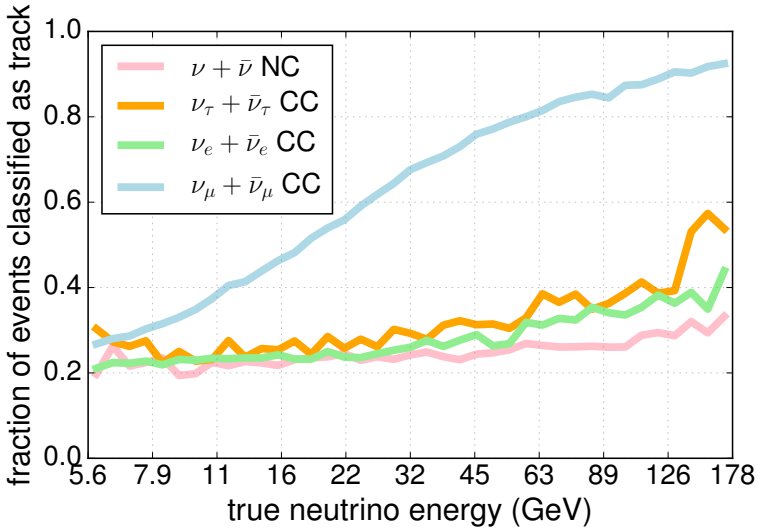

Figure 6.1: Fraction of MC events correctly identified by the PID algorithm, in true neutrino energy for reconstructed PID.

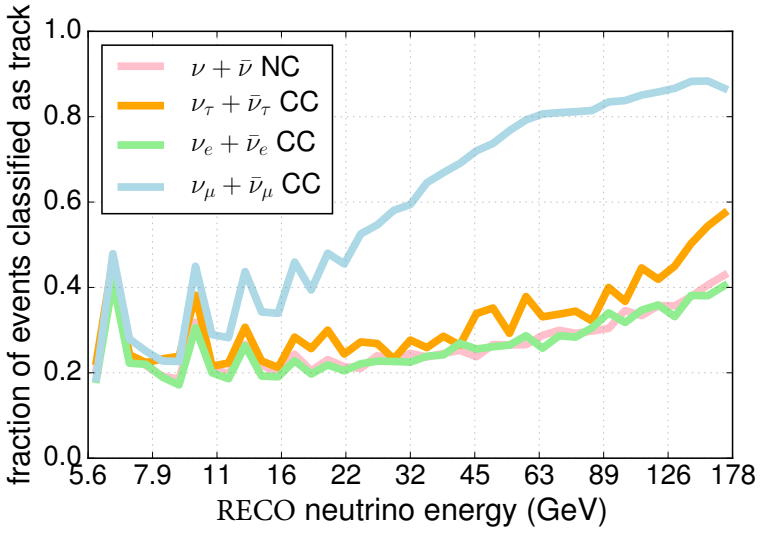

Figure 6.2: Fraction of MC events correctly identified by the PID algorithm, in reconstructed neutrino energy for reconstructed PID.

6.4 Sample Parameter Resolutions

For this analysis the primary observables for a given event are reconstructed energy, reconstructed zenith, and identified particle type (PID) which were detailed in the previous sections. The energy resolution plots show, for each flavour, the reconstructed energy and zenith resolution for the case where the neutrino event flavour is correctly identified and for the case where it is misidentified.

6.4.1 Extended Sample Resolutions

The reconstruction resolutions of the extended sample were then calculated, as shown in the following Figures. In these figures, the reconstructed energy and reconstructed $\cos(\theta_{zen})$ are shown for reconstructed PID cascade-like and track-like. In general, the resolutions are improved in cases where the PID assigned the correct particle type category. The true particle flavour is listed in the top right in each plot.

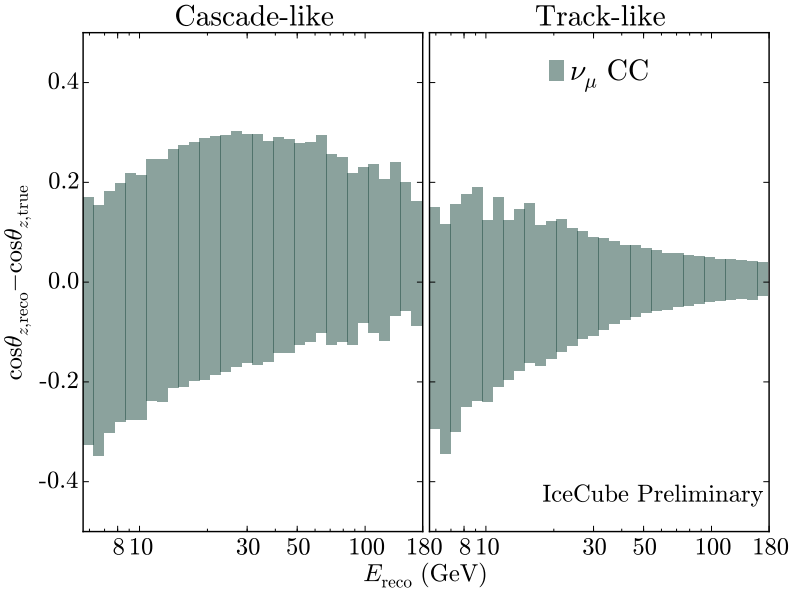

Figure 6.3: Shown is the 50% central region of the $\cos(\theta_{zen})$ resolution for ν_μ CC with weights from best fit in [3], plotted as a function of reconstructed energy.

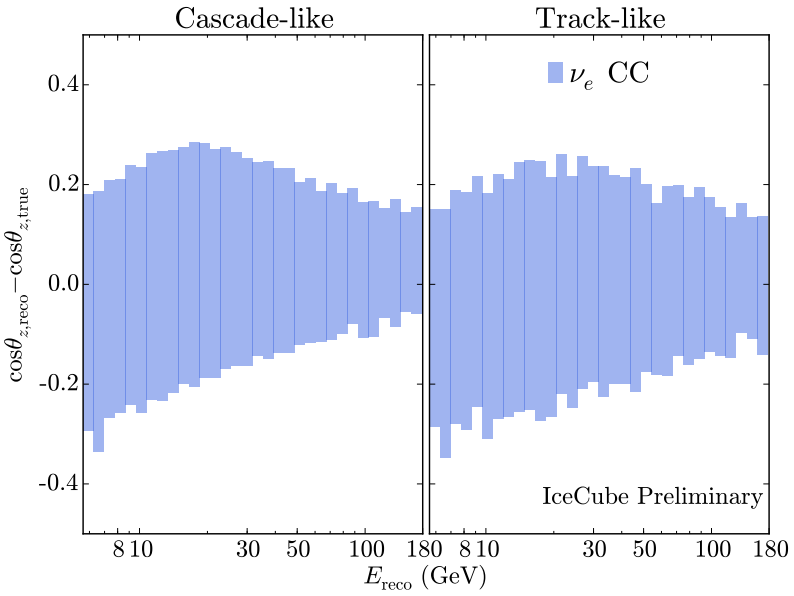

Figure 6.4: Shown is the 50% central region of the $\cos(\theta_{zen})$ resolution for ν_e CC with appropriate weights from best fit in [3]; plotted as a function of reconstructed energy.

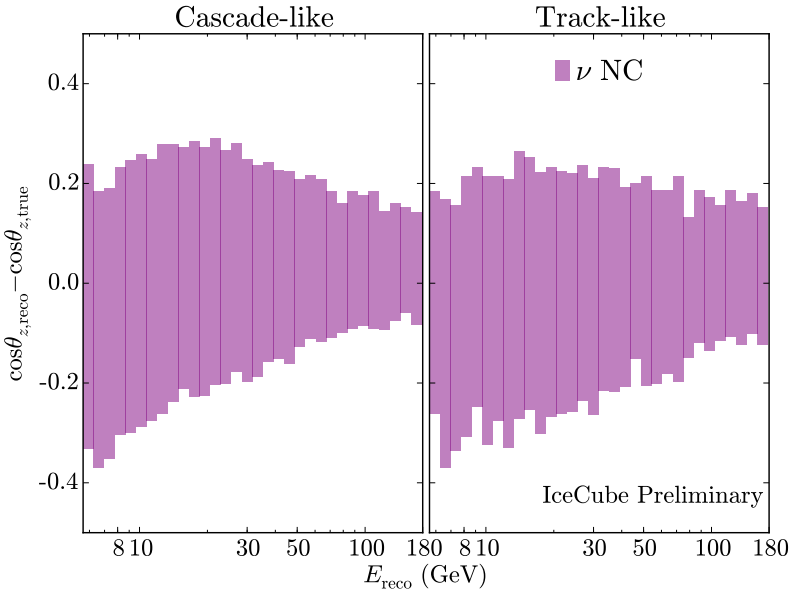

Figure 6.5: Shown is the 50% central region of the $\cos(\theta_{zen})$ resolution for ν NC with appropriate weights from best fit in [3], plotted as a function of reconstructed energy.

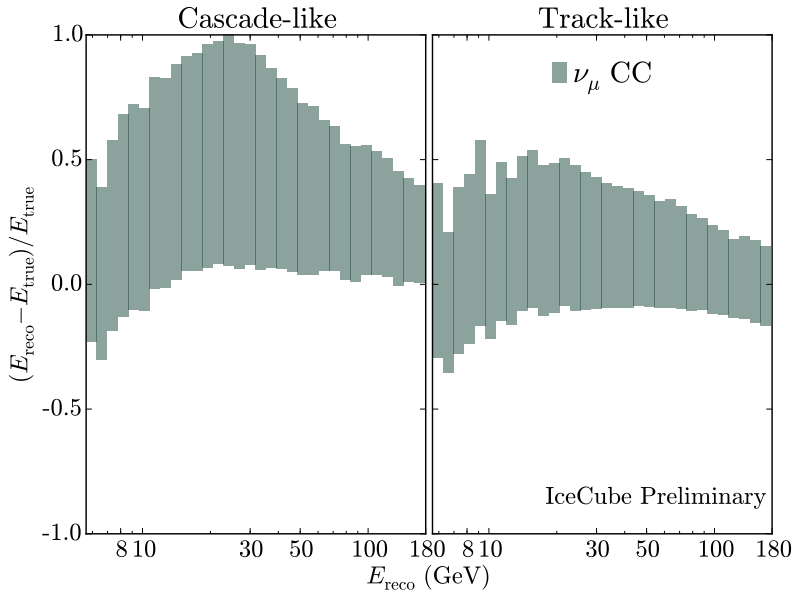

Figure 6.6: The 50% central region of the energy resolution for ν_μ CC with appropriate weights from best fit in [3], plotted as a function of reconstructed energy.

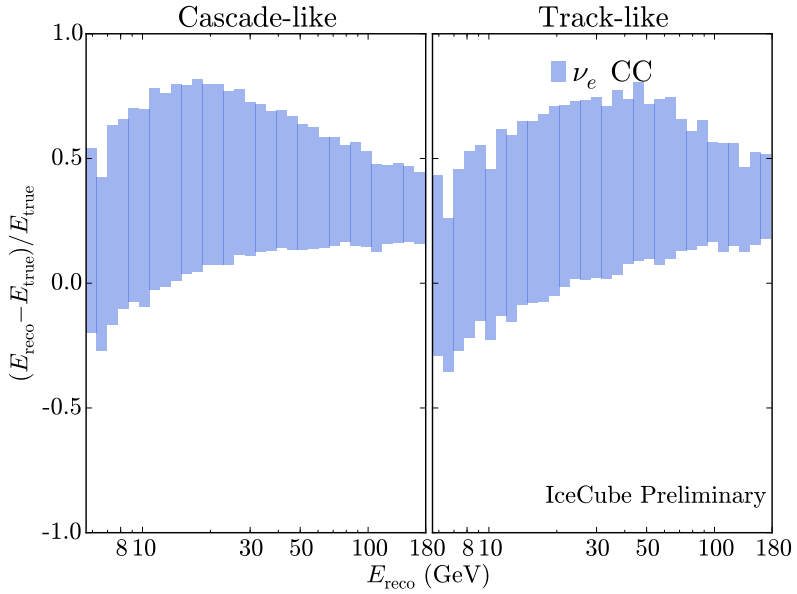

Figure 6.7: The 50% central region of the energy resolution for ν_e CC with appropriate weights from best fit in [3], plotted as a function of reconstructed energy.

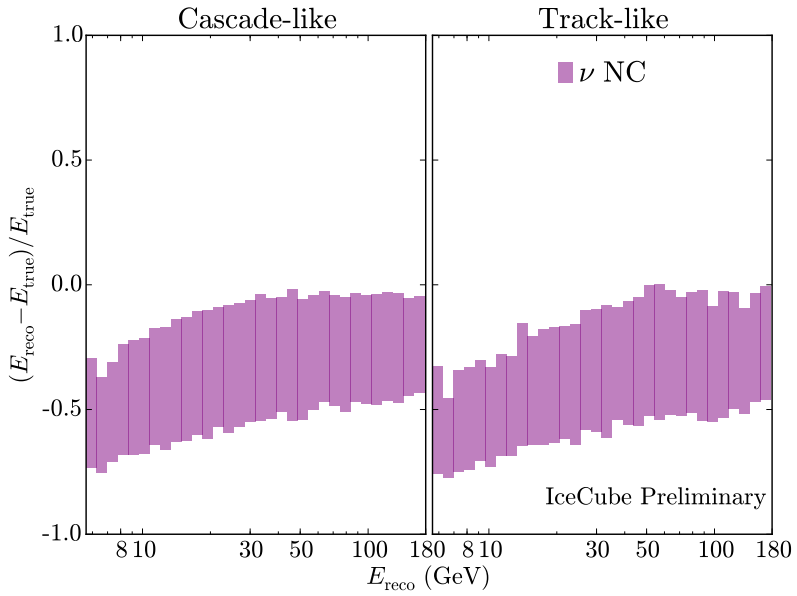

Figure 6.8: The 50% central region of the energy resolution for ν NC with appropriate weights from best fit in [3]; plotted as a function of reconstructed energy.

6.5 Final Analysis Level Parameter Binning

The data and MC are then binned in an 8×10 histogram 2D in $\log(E_{reco})$ and reconstructed $\cos(\theta_{zen})$. There is one histogram for PID track-like and one for PID cascade-like, for a total of 160 bins. These histograms are then evaluated bin-by-bin with the analysis test-statistic (discussed in later chapters) and the MC parameters are adjusted to find the best fit with the data.

Cos(θ_{zen})

The zenith binning was chosen to be in $\cos(\theta_{zen})$ so that an equal amount of phase space, and therefore weighted flux, would be included in each bin zenith bin. In addition, the zenith resolution of our detector at the energies was taken into account in the bin division. Tests were performed by the data sample group [3] (internally called DRAGON) to show that there was no statistical gain by including more zenith bins, due to the detector's angular resolution [3].

Energy

The binning in energy is performed in log(energy), which was chosen so as to have roughly equal statistics in each bin. This choice in binning was further motivated roughly by sample energy resolution in ν_μ (the dominant sample component at $\sim$ 70%); close to flat over the energy range of interest in the log energy scale except at the lowest energies (see figure 6.6). Note that events present in the previous analysis at lower energies [3], are retained here.

Table 6.5: Final level sample analysis binning; In this analysis the observables for a given event are: reconstructed energy, reconstructed zenith, and calculated particle identification (PID), *i.e* event classification.

Detector Variable Observable	Number of bins	Range
Neutrino Energy ($\log_10$ E_ν/GeV)	10	[0.75, 2.25]
Neutrino zenith angle ($cos(\theta_\nu)$)	8	[-1,1]
Neutrino Flavour PID	2	Track-like or Cascade-like

The final data sample, binned as per the criteria in Table 6.5, are shown in Figure 6.9. One finds 80 bins per PID, for 160 bins total. The resultant distributions are used in the next steps to extract the model tests and characterization of the atmospheric neutrino flux (see Results Chapter 8).

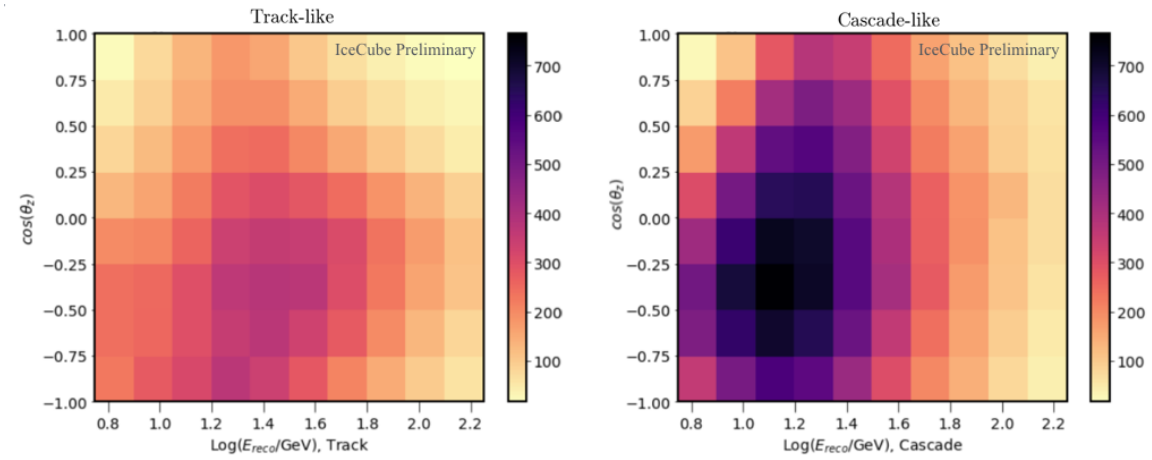

Figure 6.9: Showing the binning observables for the final extended data sample which are. For (Left) PID 'Track-like' (Right) PID 'cascade-like'. Note: The zenith angle shown is relative to the IceCube detector coordinate system, where -1 corresponds to "up-going events".

Chapter 7

Systematic Uncertainties and Atmospheric Neutrino Flux Characterization

This analysis may be cast as two distinct parts: the first tests models of the atmospheric neutrino flux against our data sample (as discussed in section 7.3.1); the second characterizes the atmospheric neutrino flux, including a model-independent measurement of the atmospheric neutrino energy spectrum, and a (quasi) model-independent measurement of the kaon-to-pion fraction for the data sample (discussed in section 7.3.2). To fully evaluate these elements, the full suite of systematic uncertainties impacting the measurement must first be considered, as described in section 7.1. Note that detailed descriptions of the flux models described throughout the chapter are available in Appendix D.1.

7.1 Systematic Uncertainties (Nuisance Parameters, s_j)

The systematic uncertainties affecting this analysis (all treated as nuisance parameters, s_j in the fit (see equation 7.1)) may be described via three primary categories: those from input models; those from the detector itself; and those from backgrounds that that may contaminate the signal. Each are described in turn in the next subsections.

7.1.1 Detector Systematics Uncertainties (Nuisance)

The detector systematics described here are the dominant set of of uncertainties in the analysis, and for the low-energy DeepCore analyses in general. They are handled through linear parameterization of simulation sets, as detailed below.

Overall DOM Efficiency

To estimate the impact of the overall optical efficiency of the detector deployed in the ice, seven discrete Monte Carlo sets spanning the range of 85% - 115% (in 5% steps) were generated. All seven sets were processed using the full event selection, and the final level events were binned for the analysis observables following the criteria in Table 6.5. The impact of varying the detector optical efficiency is estimated by fitting a linear polynomial to the event rate obtained from the discrete sets in each analysis bin. A Gaussian prior, centred at the nominal efficiency of 100% with a $\sigma = 10\%$ is applied.

DOM Angular Acceptance of Photons (Lateral and Head-on)

An ice-based systematic is the angular acceptance of the deployed DOMs (see figure 7.1). Specifically, the optical effect of bubbles in the re-frozen deployment holes where the strings of DOMs are situated must be considered.

The holes are melted with a hot-water drill and the refreezing process is completely unlike the process under which the glacier formed. As such, these holes have different ice properties than the rest of the detector medium (called the bulk ice). Where the glacier at these depths is extremely optically transparent (with an average scattering length of 70 m and absorption length of 90 m) the hole ice has an estimated scattering length of 20 cm. This results in changes to the angular acceptance of the DOMs and impacts DeepCore analyses, in particular as low-energy neutrinos leave such a small signal in the detector. To measure these effects, onboard DOM LEDs ("flashers") are used to illuminate nearby ice with known amounts of light. The calibration LED

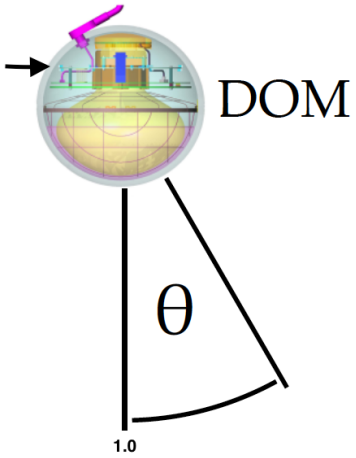

Figure 7.1: Showing an artist's illustration of the DOM, where 'head on' corresponds to a photon incoming at 1.0 (*i.e.* into the PMT face). This photon direction has the highest uncertainty. This is due to the horizontal (0.0) placement of the calibration board which houses the LEDs on each DOM (location marked by the black arrow). This results in our ice models being most effective at lateral angles.

flashers emit light primarily laterally that is generally absorbed by the neighbouring DOMs in dominantly horizontal incoming angles. These means that while there is

relatively good calibration data for light that passes through the glacier and then enters a re-frozen hole ice area lateral to a PMT, there is virtually no mechanism to determine the effect of the hole ice on directly up-going light (perpendicular the PMT face). Due to these differences, the effects of hole-ice are broken into two detector systematic uncertainties, relative optical efficiency - lateral, and relative optical efficiency - head-on.

These systematics are treated in a similar way to the overall optical efficiency (see previous). Ten discrete systematics sets with different effective scattering coefficients between 0.010 cm^{-1} and 0.033 cm^{-1} are used. Each MC set is processed to the final analysis level. A bin-by-bin effect on the event rate is determined by comparing the MC histogram to the analysis data histogram distributions in the analysis binning (160 bins total). Intermediate values are estimated with a linear parameterization between discrete simulation sets. A Gaussian prior of 0.020 ± 0.010 cm^{-1} is applied. The central values were determined with camera calibration runs [3].
The head-on optical efficiency effect on the angular acceptance is not well constrained [3] and so it is allowed to vary from the level measured in the lab (*i.e.*, no modification by the local ice) and no prior is placed on it. Please see [51] for details on the implementation. The uncertainty in these two parameters, and how they modify the photon detection, can be seen in figure 7.2.

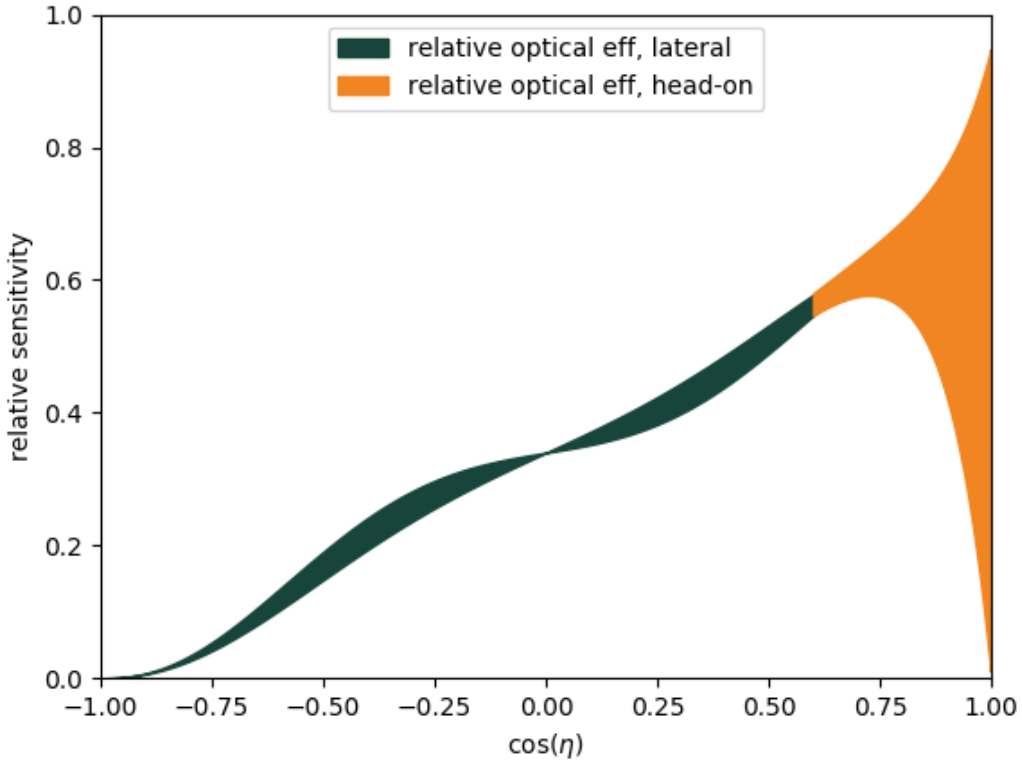

Figure 7.2: The relative sensitivity of photon detection as a function of the incoming photon direction [3]. The $\cos(\eta)$=-1 corresponds to photons perpendicular to the base of the PMT, while $\cos(\eta)$=1 corresponds to photons perpendicular to the face of the PMT, or bottom of the DOM (see figure 7.1). The dark green filled region shows the 1σ range for the relative optical efficiency, lateral, while the orange filled region shows the allowed range of the relative optical efficiencies, head-on. The angular dependence of the detector response has been extensively studied over twenty years of operation of the IceCube and AMANDA detectors. The DOM response to Cherenkov photons at lateral angles of incidence is well constrained by LED "flashers" installed on neighbouring DOMs (see figure 7.1).

7.1.2 Atmospheric Neutrino Flux Model Systematic Uncertainties

Those parameters related to the atmospheric neutrino flux, other than the overall normalization of the flux that is left unconstrained to account for uncertainties on the absolute flux of atmospheric neutrinos, are either fixed to a model prediction via the flux predicted by a model (as in the first part of the analysis 'model tests'), or are measured (as in the second part of the analysis on characterizing the atmospheric neutrino spectrum).

In the model dependent measurements (case study A) the typical flux parameters, like the cosmic ray spectral index, γ, the normalization of the ν_e flux (*i.e.* $\nu_e + \bar{\nu}_e$), the $\nu/\bar{\nu}$ and kaon-to-pion ratios (upward going / horizontal going) flux, are all fixed to the model values effectively via the predicted flux, for the model tests that will be employed. Please see section 7.3.1 for full details.

In the (quasi) model independent characterization of the flux (case study B of this analysis), the spectral index is not limited to a given value and instead a model independent segmented fit was preformed, where a given energy segment is free to float to the best fit value. The K/π ratio is also measured. Please see section 7.3.2 for full details.

7.1.3 Neutrino Mixing Parameters (Nuisance)

Uncertainties associated with the oscillation of the atmospheric neutrinos from production to detection (see Appendix A) directly impact the flux analysis. Those not directly related to the atmospheric neutrino measurements are fixed to the current global best fit values used in [3] which come from nufit 2.0 [11], with their uncertainties. We consider the oscillation parameters in distinct sets. The first set are Δm^2_{21}, $\sin^2\theta_{12}$ and δ_{CP} which are fixed in in this analysis, as DeepCore does not have sensi-

tivity to these parameters. The second set of values are (Δm^2_{32}, $\sin^2\theta_{23}$ and $\sin^2\theta_{13}$), related to the atmospheric neutrino oscillations. These may impact the analysis and are free to float to their best fit values.

While these parameters are among the least impactful in the study, they provide an important crosscheck on the result as a fit with a large pull of the extracted oscillation parameters from the previously measured values [3] would be cause to re-examine the success of the fit.

7.1.4 Cross-Section Systematics (Nuisance)

The dominant interaction processes for neutrinos in the energy range of this analysis are deep inelastic scattering (DIS), resonant production and quasi-elastic scattering (QE) (see Figure 7.3 and 7.4). In this analysis the uncertainties of the DIS cross-sections are considered via overall normalization of the flux. Uncertainties of the non-DIS processes, (*i.e.* resonant production and quasi-elastic scattering), are estimated by GENIE simulation (by varying the axial mass resonance for charged current quasi-elastic (CCQE) scattering (called M^{CCQE} in GENIE) as a correction to the weights of the generated interactions. Note: the GENIE authors state that M^{CCQE} is merely an effective parameter; it reproduces the correct differential cross-section at low energy but is masking nuclear physics processes that are not included in the current GENIE model [45] [3]. The default value of 1.12 GeV and prior of 0.22 GeV (the one sigma error) were taken from GENIE [45]. In this analysis, we following this convention and allow the axial mass resonance to vary in our fits.

Note: in the analysis results this parameter is labeled as M_A^{res}, and we measure how many sigma away from 1.12 we are; (*i.e.* for example, a measured value of 0.4 means we are 0.4 of a sigma away. Then: 1.12 - (0.4)*0.22 = 1.03. This means we measured a value of 1.03, instead of 1.12).

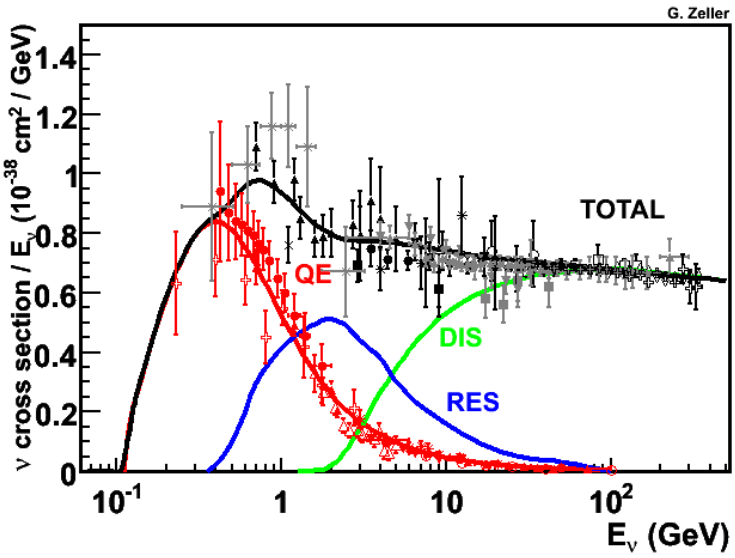

Figure 7.3: Showing current knowledge of neutrino charged-current cross sections [55]. The plot shows the total neutrino per nucleon CC cross-sections divided by neutrino energy, as a function of energy [55]. Data on this plot is discussed in [55] and is for isoscalar targets.

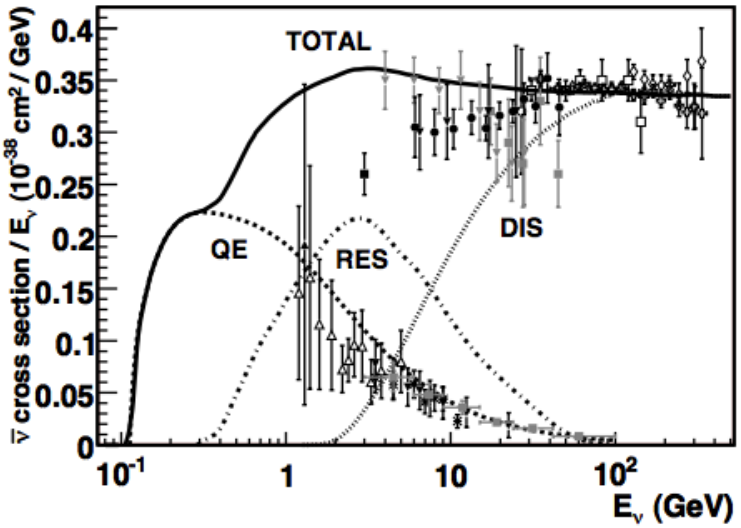

Figure 7.4: Showing current knowledge of anti-neutrino charged-current cross sections [55]. The plot shows the total anti-neutrino per nucleon CC cross-sections divided by neutrino energy, as a function of energy [55]. Data on this plot is discussed in [55] and is for isoscalar targets.

7.2 Background Considerations

7.2.1 Atmospheric Muons

As discussed in Chapter 4.1.2, the main background in this analysis is from atmospheric muons reaching the DeepCore fiducial volume undetected. This has been studied in detail for the extension to the data sample used in this analysis. Note that the atmospheric muon background decreases dramatically with energy as higher energy muons produce more light and are more easily rejected (see figure 7.5). The impact of the muon background is addressed using a data-driven technique [3], where the muon template is added to the expected neutrino event rate and its normalization is left unconstrained in order to assess the impact of the atmospheric muon background. Together this provides the total event expectation.

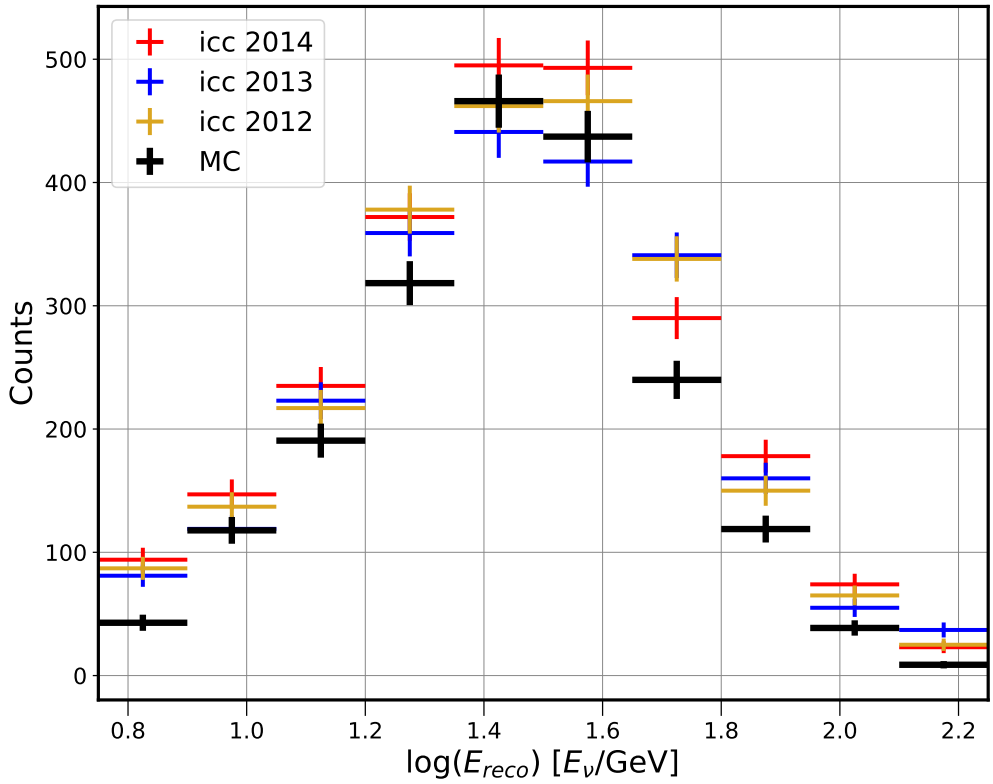

Figure 7.5: Showing events with directions along identified corridors in the main IceCube array. Here we see the muons removed when cutting out events with two casual hits near a corridor region. The MC represents two months of simulated atmospheric muons. The spectrum of the data events tagged as atmospheric muons by this cut are used to estimate the background signal in this analysis. The muons from each analysis year are histogramed according to the analysis binning and the MC set is scaled to the 2012 data rate.

7.3 Atmospheric Neutrino Flux Measurements

The analysis of the atmospheric neutrino flux performed here has been divided into two distinct case studies; model dependant (A) and (quasi) model independent (B). The goals of these case studies are:

Case study A: Model-dependent
Comparison of known model predictions to the final data set to provide a measure of the discrimination power between models (cosmic ray + hadronic interaction).

Case study B: (Quasi) model-independent
Directly measure the parameters related to the atmospheric spectrum from the data by exploring the model space, *i.e.*:

B.1: Measure the K/π ratio in a semi-model independent approach for a given combination of cosmic ray, hadronic interaction, and atmospheric models.
B.2: Measure the neutrino energy spectrum and the absolute normalization of the flux for muon and electron neutrinos from 5.6–180 GeV in reconstructed energy, unfolded up to a true energy of 1 TeV.

In each of the next sections we detail the development of each of the case studies to provide the measurement goals above. The final results of each are discussed in Chapter 8.

7.3.1 A - Model-Dependent Measurements

In the first part of the analysis (that was performed last for reasons of blindness), the final data sample is used to test a set of fixed model permutations as follows: for each of the considered atmospheric neutrino flux model permutations (see Table 7.1) the atmospheric neutrino flux predictions are tabulated and the final level signal simulation is re-weighted to reflect these predictions. Realizations of the predicted MC data with Poissonian noise as shown in Figure 7.6. These are then fit with all nuisance

parameters considered (see Table 7.2), with the analysis machinery (MINUIT2 [56]) using a modified χ^2; given by

$$\chi^2 = \sum_{i\in\{\text{bins}\}} \frac{(n_i^{\nu+\mu_{\text{atm}}} - n_i^{\text{data}})^2}{(\sigma_i^{\text{data}})^2 + (\sigma_{\nu+\mu_{\text{atm}},i}^{\text{uncor}})^2} + \sum_{j\in\{\text{syst}\}} \frac{(s_j - \hat{s}_j)^2}{\hat{\sigma}_{s_j}^2}. \tag{7.1}$$

Here $n_i^{\nu+\mu_{\text{atm}}}$ is the predicted number of events (the sum of neutrino events weighted to the oscillation parameters using Prob3++ [57] and the atmospheric muon background) in the i^{th} bin. The number of observed events in the i^{th} bin is n_i^{data}, having a Poisson uncertainty $\sigma_i^{\text{data}} = \sqrt{n_i^{\text{data}}}$, and $\sigma_{\nu+\mu_{\text{atm}},i}^{\text{uncor}}$ is the uncertainty in the prediction of the number of events of the i^{th} bin. The term $\sigma_{\nu+\mu_{\text{atm}}}^{\text{uncor}}$ includes the effects of both the finite MC statistics and the uncertainties in the data-driven muon background estimate [3]. The second term of Eq. (7.1) is a penalty applied for the nuisance parameters, where s_j is the value of j^{th} systematic, $\hat{s}_j$ is the central value and $\hat{\sigma}_{s_j}^2$ is the Gaussian width of the j^{th} systematic prior [3].

The modified χ^2 is treated as a test statistic, with systematics treated as nuisance parameters. A distribution is constructed from the best fits of the resultant test statistic. The output distribution is fit with a χ^2 distribution to determine the effective number of degrees of freedom. As priors are used in the analysis, some of the parameters only effect a partial degree of freedom; as well, due to the atmospheric muon (atm_μ) template term, the effective degrees of freedom are less than in a classical χ^2. The tail of the distribution is evaluated by calculating the cumulative distribution function (CDF). These distributions are used to compute the σ and p-value for each fit. The variables in the fit are cross checked with each other to study the correlations.

A test fit was applied to the simulation dataset. The fit assumes three-flavour oscillations with $\Delta m_{21}^2 = 7.53 \times 10^{-5}$ eV^2, $\sin^2\theta_{12} = 0.304$, and $\delta_{CP} = 0^\circ$, which are from nufit 2.0 [11].

The result of the fits for one of the models to be tested is shown in Figure 7.6 with

Table 7.1: Showing the atmospheric neutrino flux models to be evaluated. This is done by comparing our data to predicted fluxes from numerical tables of fluxes generated for this analysis using open source code MCEq [4], which solves the matrix cascade equations numerically. All of the permutations of the hadronic interaction models and the cosmic ray primary models listed here are compared to our data sample (18 models). Note that the cosmic ray primary models are: GH = Gaisser-Honda [21], GSF = Global Spline Fits [58], and the Hillas model (H3a) [59]. In addition to these models, HKKM2014 [44] flux prediction tables are also compared to our data.

	CR primary Model :		
Hadronic int. model :	GH [21]	H3a [59]	GSF [58]
DPMJET-III [23]			
DPMJET-III-2017.1 [22] [60]			
EPOS-LHC [61]			
QGSJET II 04 [62]			
SYBILL 2.3c [63]			
SYBILL 2.1 [64]			

Table 7.2: Showing the fit parameters of the model dependent tests, which test our data against the18 models in 7.1 and HKKM2014.

Parameters in the fit	**Prior**
Oscillation parameters (nuisance):	N.H.
Δm^2_{31} [eV$^2 \times 10^{-3}$]	no prior
$\sin^2(\theta_{23})$	no prior
$\sin^2(\theta_{13})$	0.0238 ± 0.0001
Detector (nuisance):	
overall optical eff. [%]	100 ± 10
rel. optical eff., lateral (hole ice) [m]	0.02 ± 0.01
rel. optical eff., head-on (hiFwd) [a.u.]	no prior
Flux and cross-section parameters (nuisance):	
Neutrino event rate [% of nominal (livetime)]	no prior (total MC events, post fit)
NC relative normalization [%]	100 ± 20
M_A^{res} [σ]	0.0 (central value) $\pm 1\sigma$ (See section 7.1.4)
Background:	
Atm. μ contamination [% of sample]	no prior
Test statistic (best fit):	
χ^2_{mod} (modified χ^2 [3])	no prior

the 1-CDF Figure 7.7. The 1- CDF tail distributions of the best for for all hadronic interaction models combined with the h3a cosmic ray model is shown in Figure 7.8 as an example.

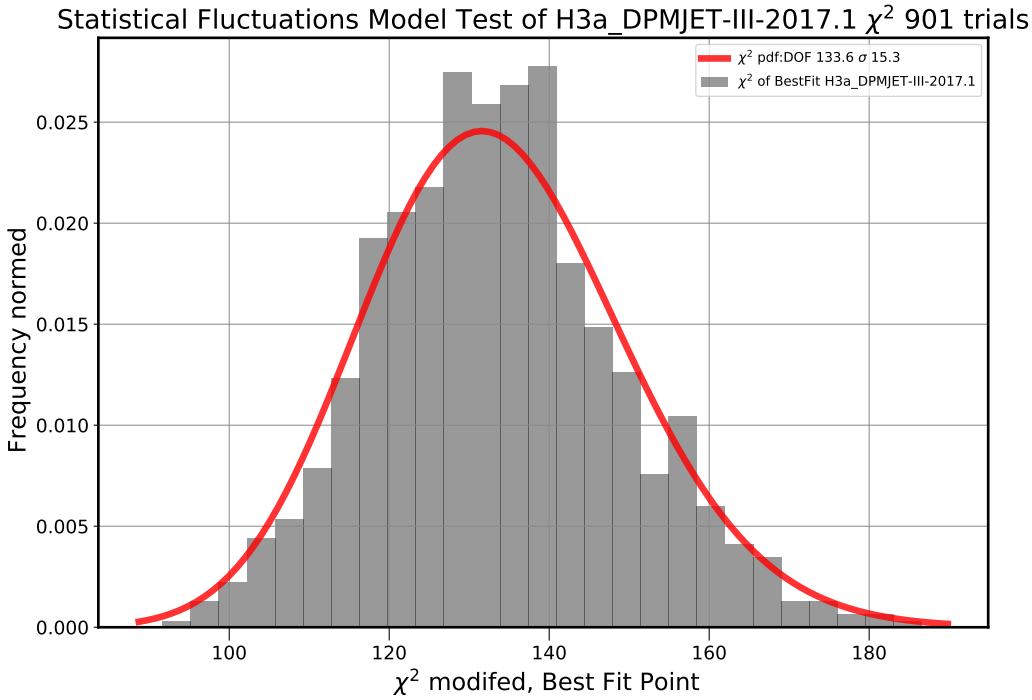

Figure 7.6: Showing best fit test-statistic values for the statistical fluctuations of the model created with MCEq [4] using H3a and DPMJET-III-2017.1.

The same fit as applied to the simulation above is then preformed against the final data set. Whenever possible, all parameters in the fit pertaining to the atmospheric neutrino flux are fixed by the given model via the predicted neutrino flux. The resulting χ^2 value of the data fit is compared using the standard deviation from the distributions in, for example Figure 7.6 and, equivalently, a p-value calculated from the tail of the CDF (1-CDF). See Figure 7.8 for example CDF tail distributions. The results of these fits are shown together with the model-independent characterization method (see next) in the Chapter 8: sections 8.2 and 8.3.

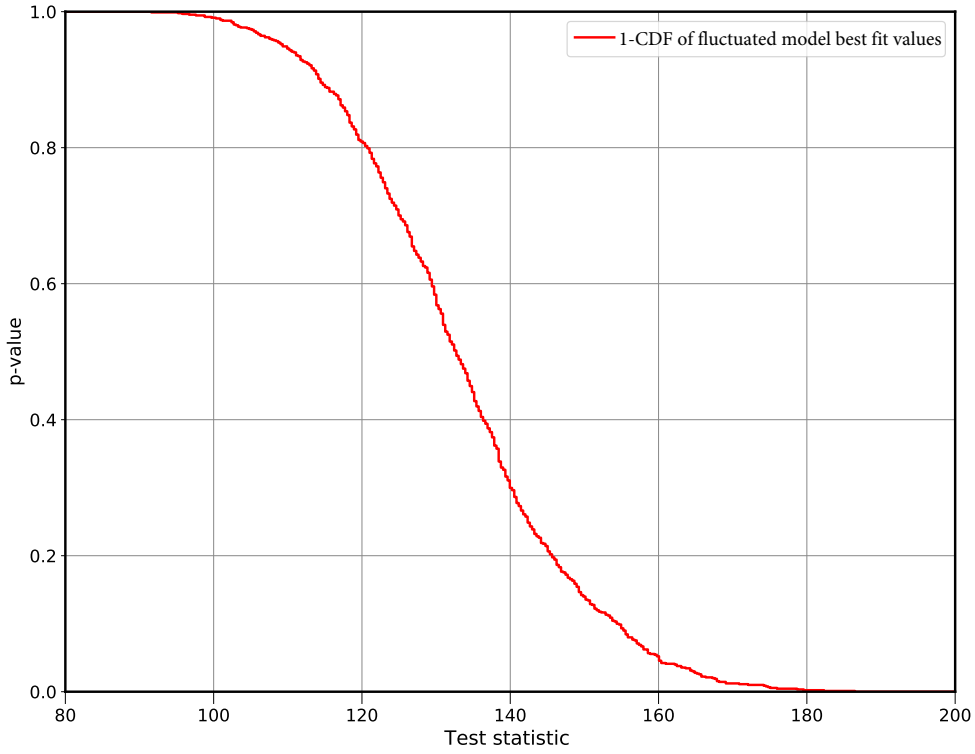

Figure 7.7: Showing the (1-CDF) tail distribution for model H3a + DPMJET-III-2017.1 best fits using the cumulative sum of the best fit test statistics in Figure 7.6 (for the model H3a + DPMJET-III-2017.1). On the y-axis the 1-CDF of best fit test-statistics is shown, which correspond to p-values.

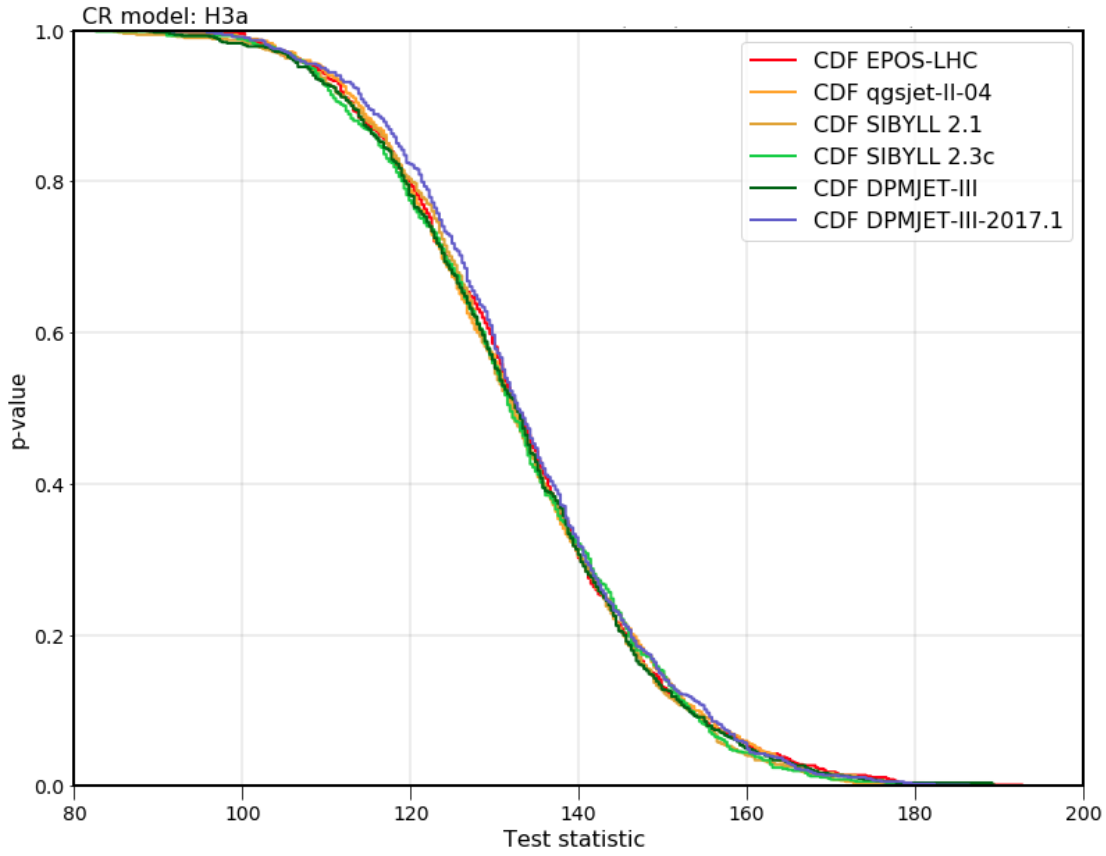

Figure 7.8: Showing (1-CDF) tail distribution for model test best fits, for all H3a based models. On the y-axis we see 1-CDF of best fit test-statistics, which correspond to p-values.

7.3.2 B - (Quasi) Model-independent measurements

Ideally in the case B study we would obtain a model-independent measurement of the atmospheric neutrino flux properties, in particular the neutrino energy spectrum with absolute flux normalization, and the K/π ratio. The development of each of these measurements is described next and, as will become clear, the outcomes compared to ideal model-independent scenario are limited.

Measurement of the neutrino energy spectrum and flux normalization

The single spectral index previously assigned by a specific selected model is replaced in this analysis with a series of segments that divide the energy range of interest into approximately equal bins in log(E). Note that the ideal case would utilize an infinite number of bins so that the spectrum may be fit precisely. However, with a detector energy resolution in this energy range of approximately 25% (see section 6.4), the segment widths are defined accordingly (see Figure 7.9).

The total events in a given energy segment then become the zenith integrated sum. For each segment, an E^{-3} energy spectrum is assumed, which is similar to the currently observed data in our energy range (see Figure 7.9), and the segments are essentially flat on flux $\times E^3$ plot.

The segment widths are also adjusted such that each has roughly equal statistics. Figure 7.10 shows the outcome of this optimization process, where the selected segmentation provides a discernible peak with similar event counts in the neighbouring segments. In the unfolding process to determine the energy spectrum, the individual segments must still be distinguishable by the minimizer. A quality check has been performed by examining the analysis observables ($\cos(\theta_{zen})$) and energy) for the selected segments (see Figure 7.11 and Appendix E). A sequential shift in the peak of the event distribution is observed for each subsequent energy segment, providing the needed separability. In the actual fit for the spectrum, the zenith of the profile

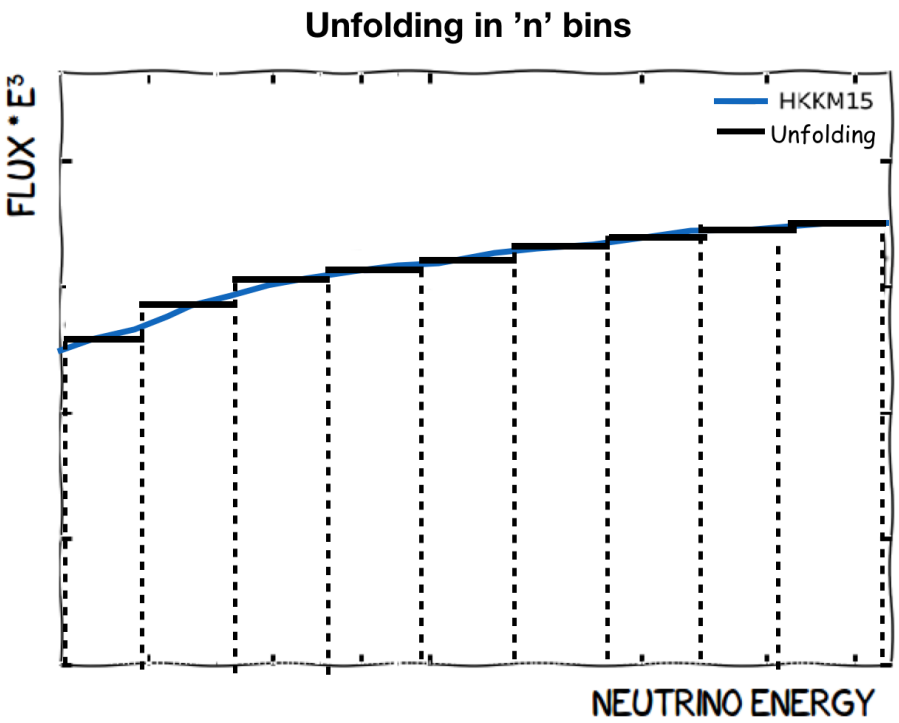

Figure 7.9: Artists representation of the unfolding of the energy spectrum in segments (bins), where each bin or 'segment' follows an E^{-3} spectrum. In the analysis, the segments for ν_μ are divided as follows by true energy (left to right in plot): Fraction1: (0-9) GeV, Fraction2: (9-15) GeV, Fraction3: (15-25), Fraction4: (25-40) GeV, Fraction5: (40-70) GeV, Fraction6: (70-120) GeV, Fraction7: (120-1000) GeV. HKKM2015 [5] (alternately called HKKM2014) for ν_μ is shown $\times E^3$ for reference.

of each segment is taken to be the same as the prediction from the DPMJET-III hadronic model [23]. The normalization for each segment is treated as a separate free parameter, preserving the zenith profile and the $\frac{\nu}{\bar{\nu}}$ ratio.

The total amount of events N is then the sum of the events in each segment 2D histogram, *i.e* $N = \sum_{i \in \text{bins}} N_{frac_i}$.

The K/π ratio is also in this fit; where each segment contains a π-flux template and a K-flux template according to the DPMJET-III, that are normalized (see next section) for a single shared scaling fraction of the K-component. Specifically, the table of fluxes predicting the neutrinos from the kaons globally does not change form or shape, but

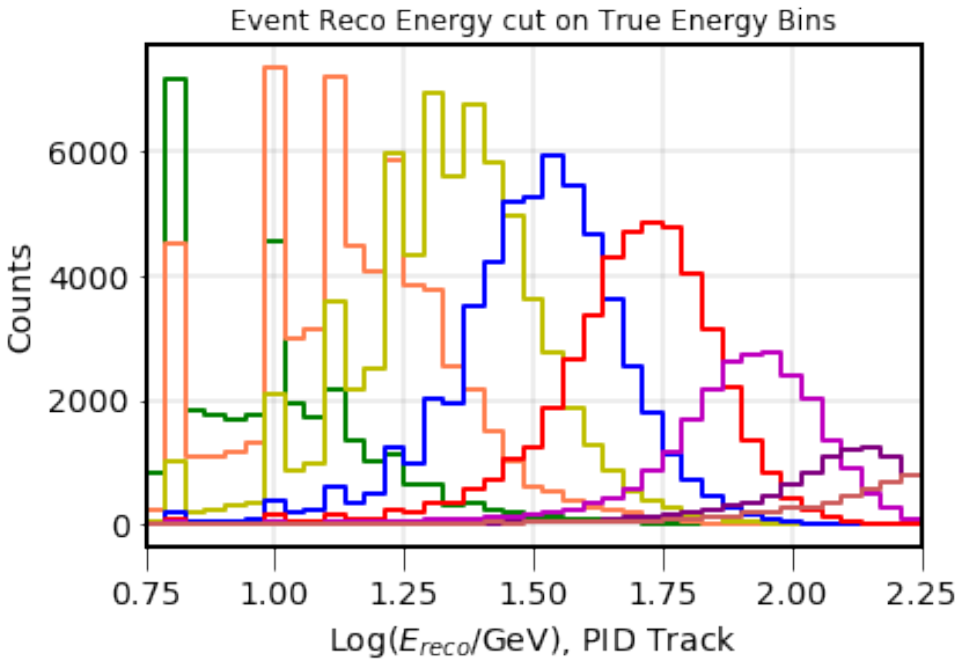

Figure 7.10: Showing the MC events in each proposed true energy segment for ν_μ events. These plots show reconstructed energy distribution in each true energy 'segment'. The peak structure at the lower energies is a relic of the reconstruction method (see previous chapter). Here the segments for ν_μ are shown and are dived as follows by true energy: Fraction1: (0-9) GeV, Fraction2: (9-15) GeV, Fraction3: (15-25), Fraction4: (25-40) GeV, Fraction5: (40-70) GeV, Fraction6: (70-120) GeV, Fraction7: (120-1000) GeV.

its normalization is allowed to float. This produces a quasi-model-independent fit for the K/π ratio in the form:

$$\Phi = N(\Phi_\pi + N_K \Phi_k) \ , \quad (7.2)$$

where Φ is the total flux, N is the overall normalization of the total flux, and N_K is the normalization of the K component. N_K is therefore provided at all energies in the segment fit. It is worthwhile to note that the method inherently ensures the shape of the distribution for π and K decays in the model is correct, which is incorrect by up to 30%-40% in some energy ranges for the known kaon-neutrino yield. Still, this method represents the most sophisticated measurement of the K/π ratio to date and

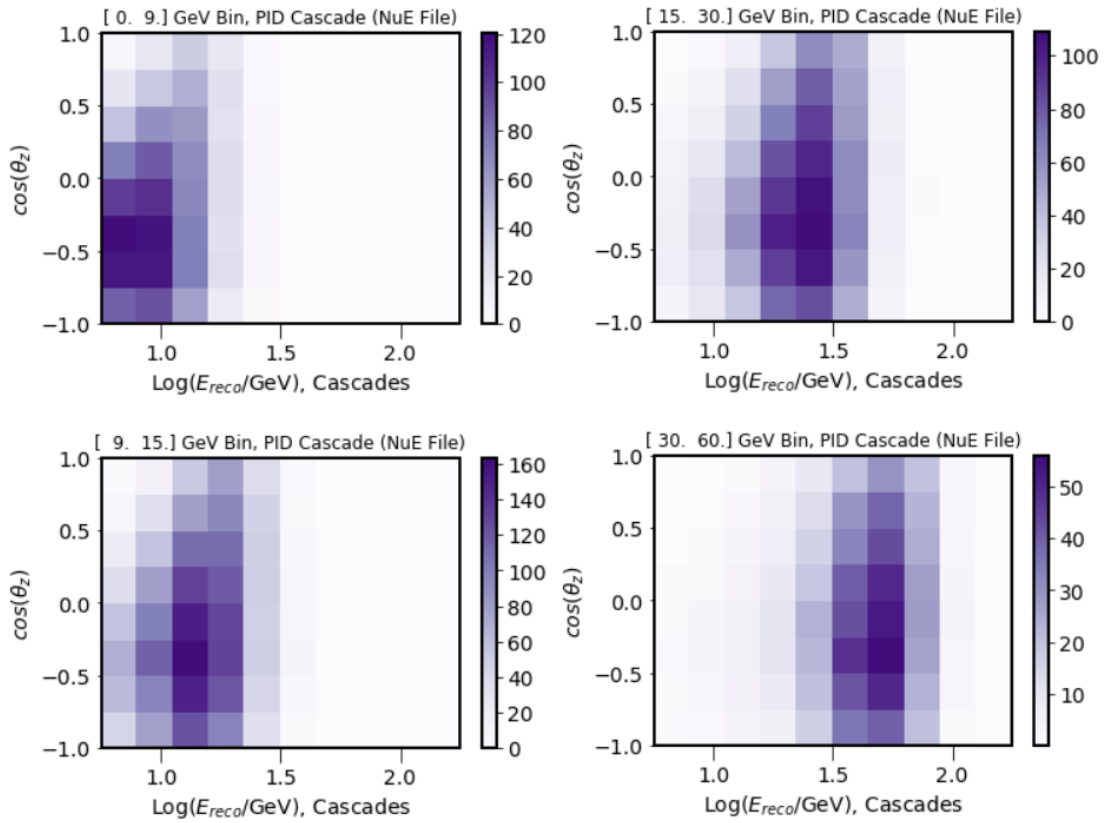

Figure 7.11: Unfolding bin optimization in observables where the x-axis is the $\log(E_{reco}/GeV)$ (energy observable proxy) and the y-axis is $\cos(\theta_{zen})$ (zenith observable), where PID cascade-like only is shown here.

represents an important first step in its understanding.

Measurements of the K/π Ratio

The K/π ratio provides a direct measure of the production mechanisms for atmospheric neutrinos. In this way the the K/π ratio is a key input to the underlying atmospheric models and, hence, advance studies involving these particles.

As discussed in Appendix E, the model numerical flux tables are generated using MCEq [4]. The tables, containing the predicted neutrino flux for given direction (zenith angle) and energy, are used to weight the available signal detector MC.

By changing the event distributions obtained when using different table configurations, it is possible to estimate the final dataset sensitivity to the K/π parameter.

The predictions for the kaon and pion contributions to the neutrino flux and K/π ratio for the primary models considered in this analysis are shown in Figure 7.12.

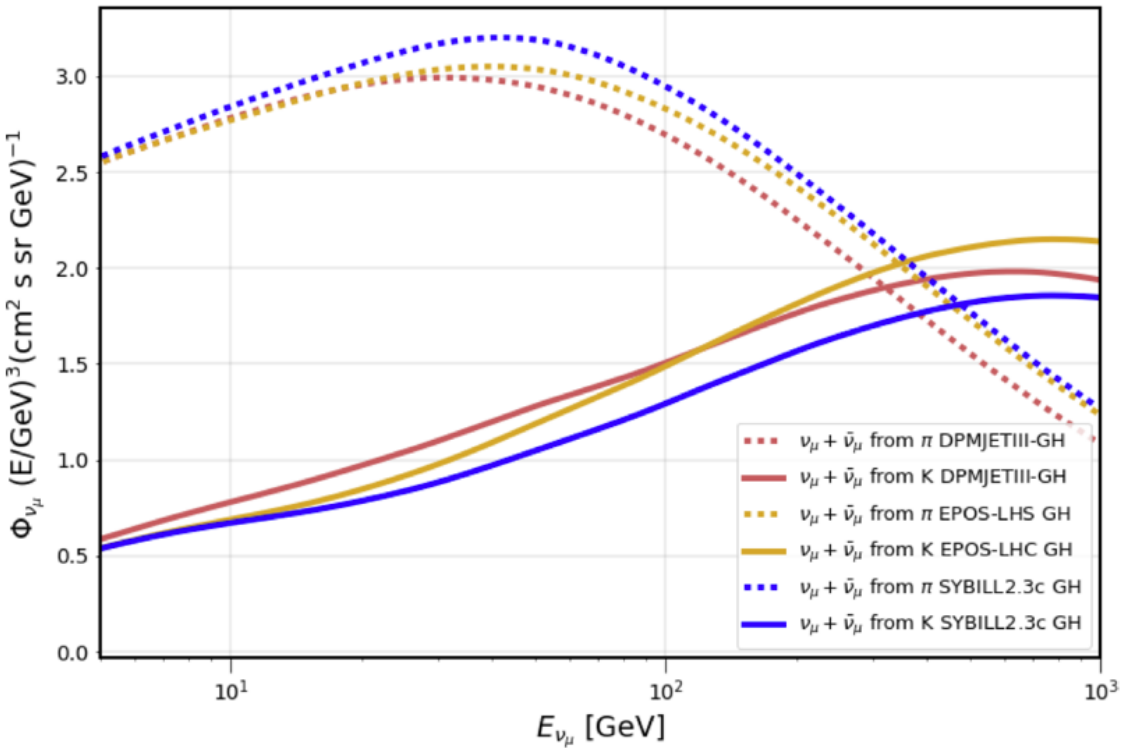

Figure 7.12: The contributions of pions and kaons to the muon neutrino flux integrated over zenith angles are shown separately as a function of neutrino energy. Hadronic interaction models included in the plot are: EPOS-LHC [65], DPMJET-III [23, 22], SYBILL2.3c [66]. Plots generated with a simple wrapper written for MCEq [4].

Here, as discussed previously, in this analysis we keep the template of the atmospheric muon neutrinos decaying from pions fixed, and we allow the component decaying from kaons to be scaled in the fit. The choice of which parent mesons table to fix is arbitrary. The scaling of the template shifts the crossover point where kaons become the dominate source of muon neutrinos (see Figure 7.12).

Figure 7.12 shows the zenith integrated ν_μ flux for the nominal value ($N_K = 1$) for

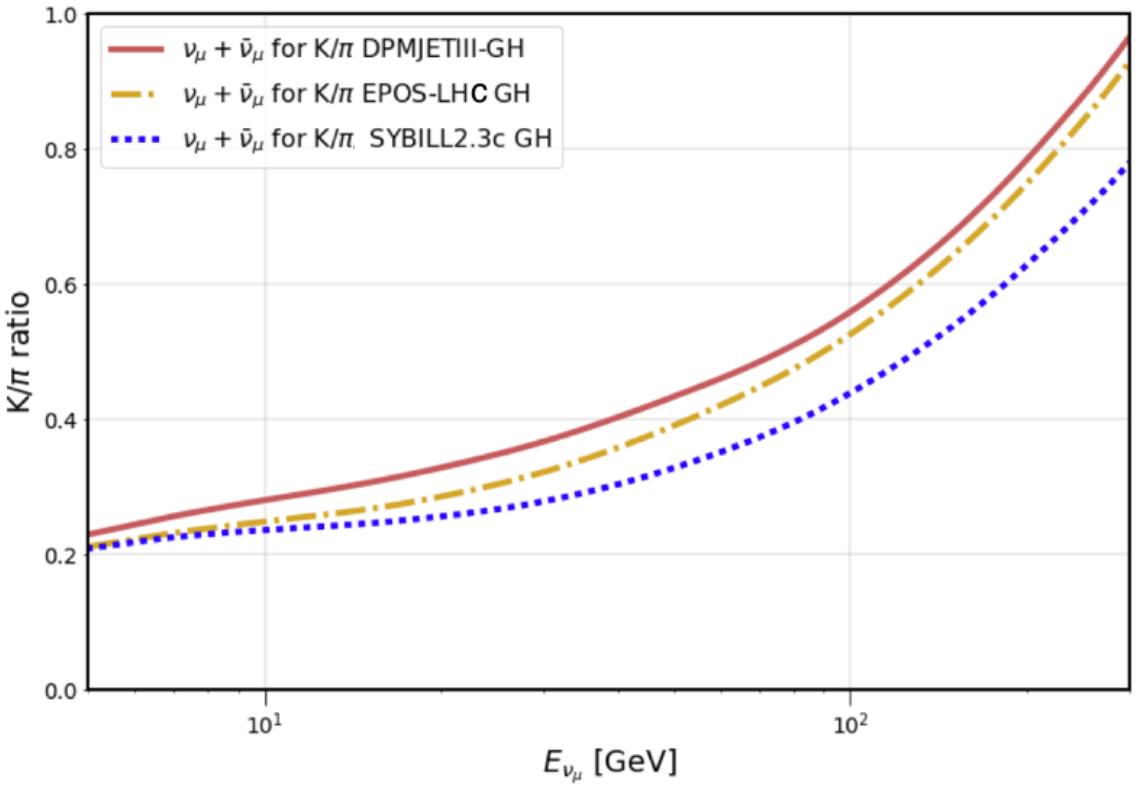

Figure 7.13: Showing zenith integrated atmospheric ν_μ flux partial contributions, arising from π and K decays (ratio). The cosmic ray primary model used was Gaisser-Honda [21] and the atmospheric model is NRLMSISE00 [5]. Plots use [4].

a given model. This information can be applied to compute the change in the K/π ratio at all energies.

Cross-checks of the Analysis Technique

Tests were conducted to demonstrate the robustness of the described analysis: the effect of the selected baseline model; and the effect of the re-weighting of the flux prediction tables.

Baseline Model Selection

Tests were run by drawing the MC simulation data from different combinations of models and unfolding the neutrino spectrum for each case. The circular MC tests (where a model is fit without added statistical fluctuations or an 'Asimov test') results shown in Figure 7.14 and 7.15 demonstrate that we can recover the different model distributions (*i.e.* a spectral distribution for which our fit has no prior input knowledge). Note that the zenith distribution contributing to this test is drawn from the combined models DPMJETIII + Gaisser-Honda + NMISSE-00.

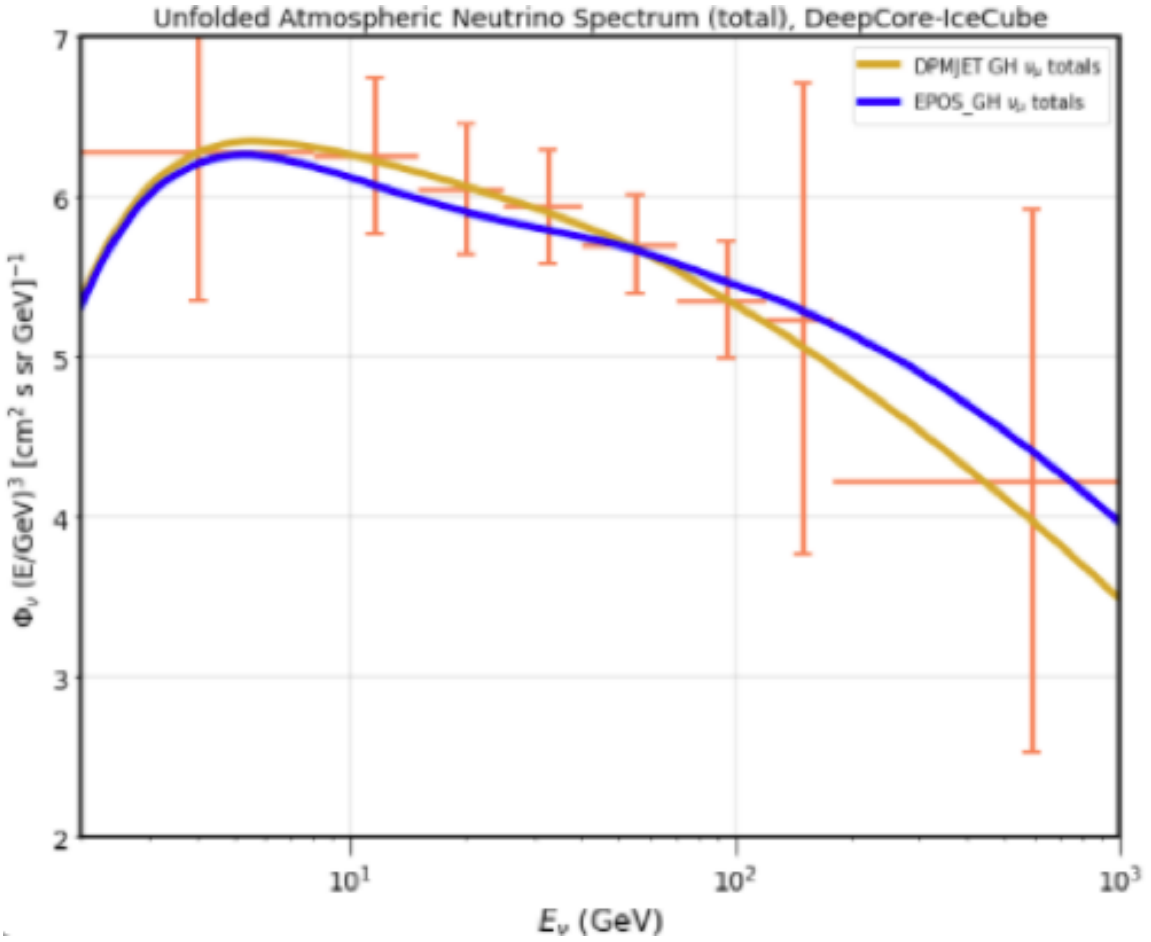

Figure 7.14: Showing a set of Asimov tests. In this test of the analysis machinery, one model (DPMJET-III + GH) is used to fit the MC data from itself. The fit works as follows: The energy segment normalizations are allowed to float, allowing one to fit any spectrum given enough segments. Here the model in yellow is used as the baseline K/π model.

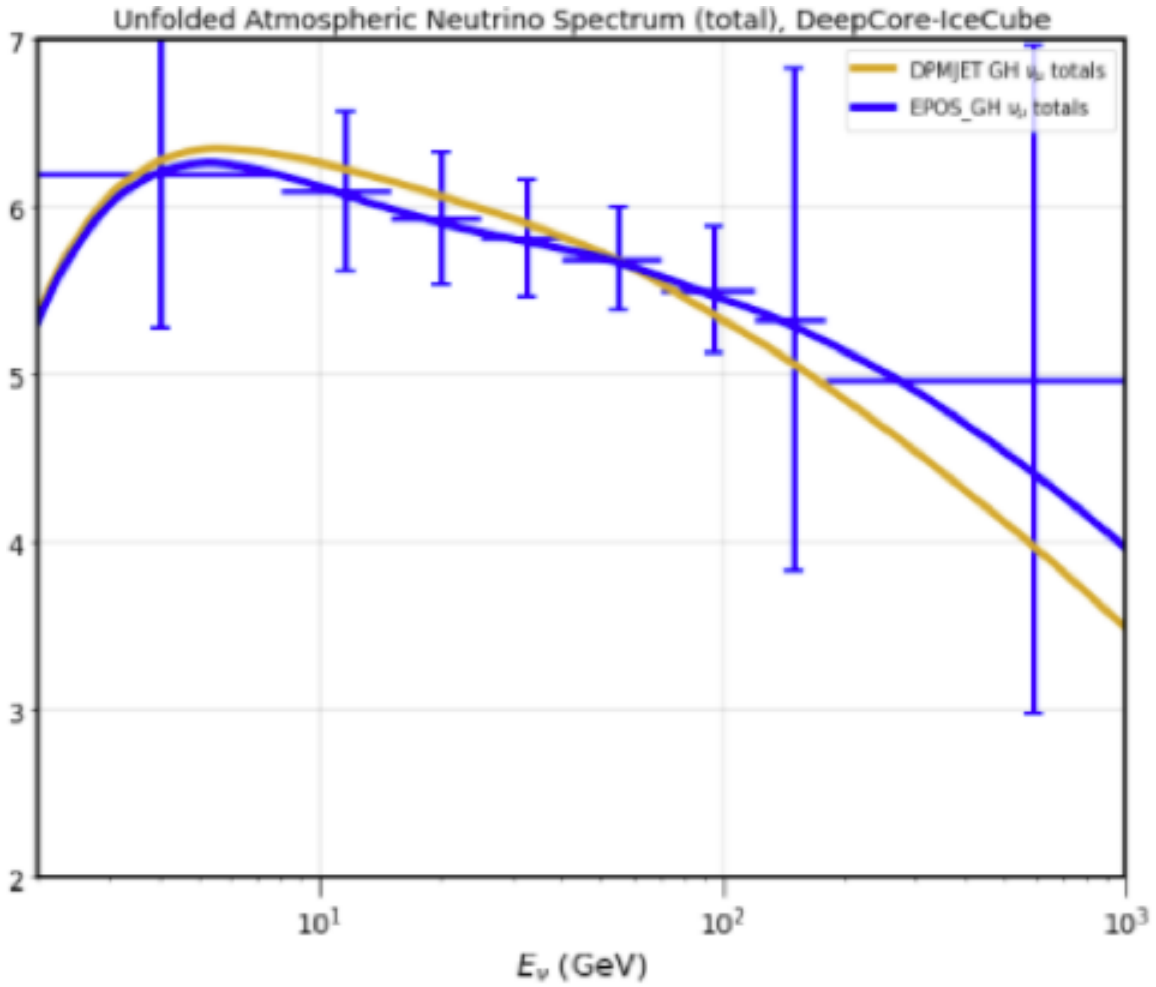

Figure 7.15: Showing a set of Asimov tests. In this test of the analysis machinery, one model (DPMJET-III + GH) is used, to fit MC data from EPOS-LHC + GH. The fit works as follows: The energy segment normalizations are allowed to float, allowing one to fit any spectrum given enough segments. Here the model in yellow is used as the baseline K/π model and so to create the fitting machinery and the model in blue is injected as 'data'. The machinery is able to fit this spectrum with an Asimov χ^2_m result of 0.002 despite being based on the model in yellow.

Re-weighting the Flux Prediction

In this test the sample is re-weighted (according to an E^3 spectrum, as discussed above) on an event-by-event basis. The resultant distributions are then evaluated for the potential impact on the zenith parameter. The critical point to take away is that we want to preserve the shape of the zenith distribution. Figures 7.16 and 7.17 show the zenith integrated neutrino flux prior to and with re-weighting applied to

the sample, respectively. We find that new weights slightly over-predict the flux at the lowest energy bins and then begin to under predict the flux at the middle bins.

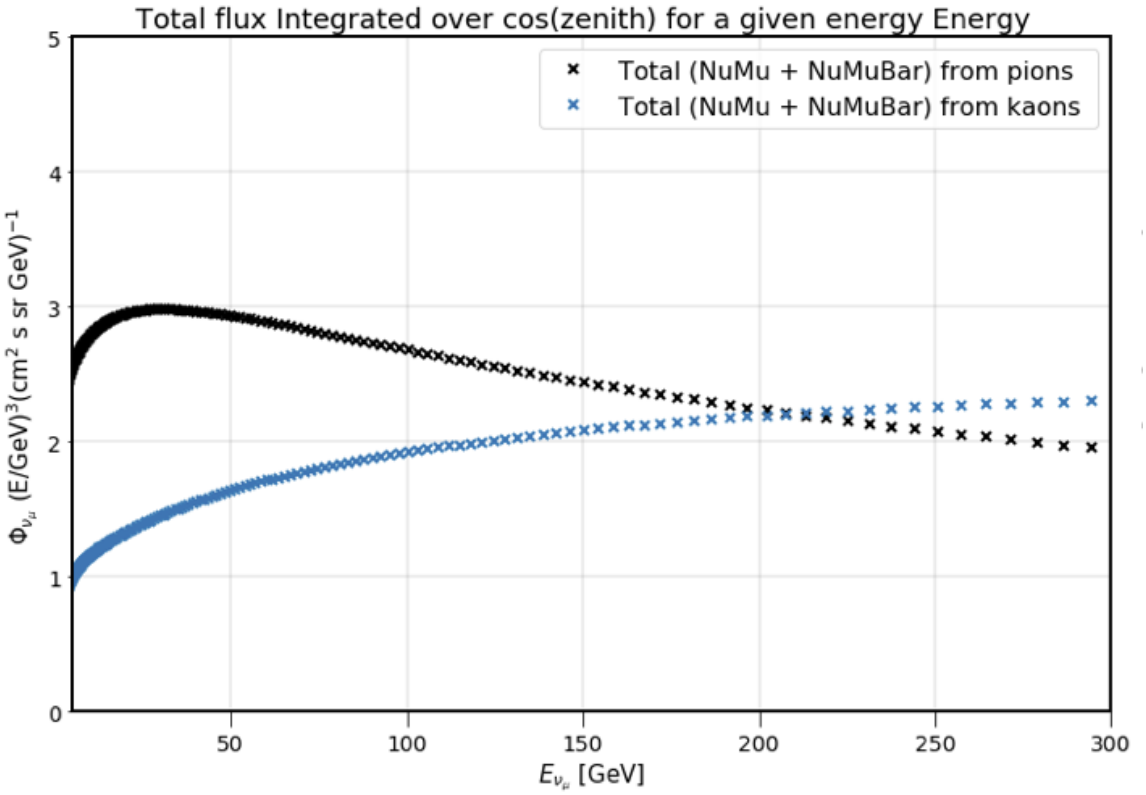

Figure 7.16: Showing the zenith integrated neutrino flux and energy prior to re-weighting of the MC sample. Here ν_μ from kaons are shown in blue and pions in black. The cosmic ray primary model used was Gaisser-Honda [21] and the atmospheric model is NRLMSISE-00 [5].

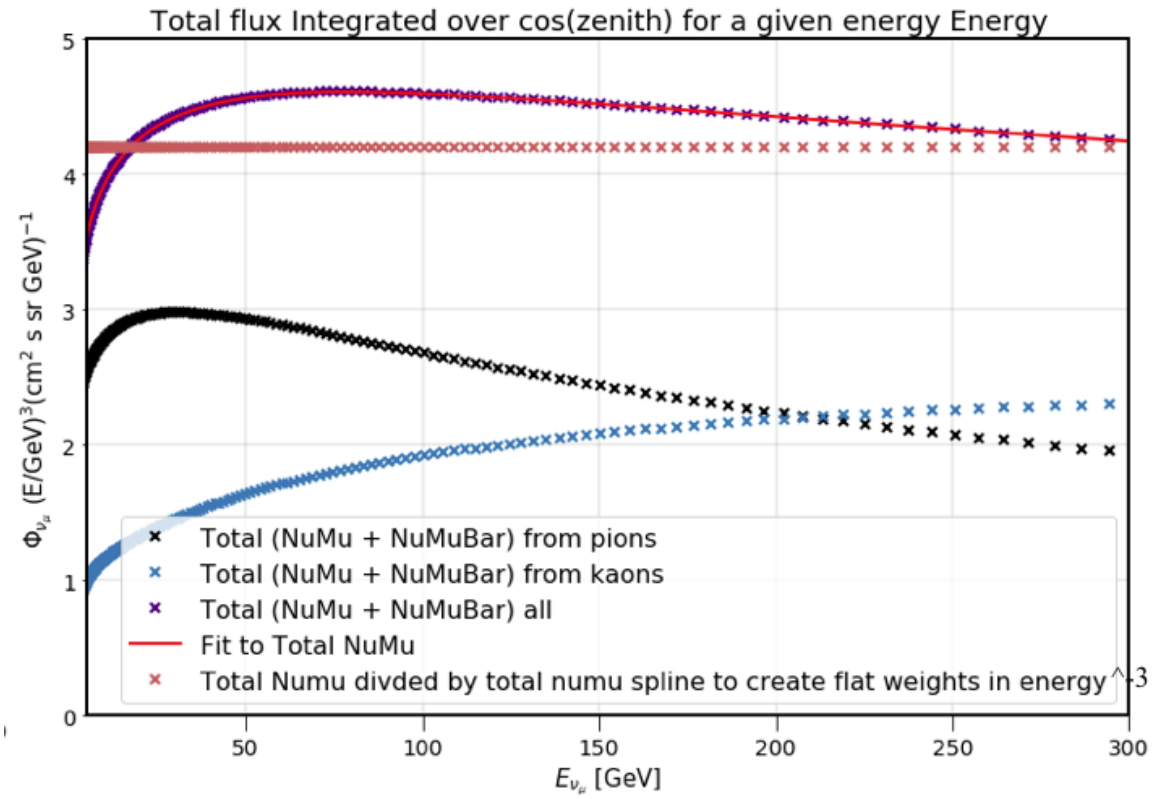

Figure 7.17: Showing the zenith integrated neutrino flux and energy with re-weighting by the MC sample. Here ν_μ from kaons are shown in blue, pions in black, and their total in purple with a spline fit underlying in red. The pink line shows total/(spline of total) that is then scaled to the average flux value of the purple (total ν_μ) line. The cosmic ray primary model used was Gaisser-Honda [21] and the atmospheric model is NRLMSISE-00 [5].

Chapter 8

Results

This chapter provides the results of the model-dependent (case study A) and quasi-model independent (case study B) analyses. It begins with a discussion of the initial data/MC test of the fitting procedure using a dedicated small statistical sample. An overview of the measurement for Case A is next, including the fit results and the full parameter values and uncertainties at the best fit of the most probable model (including all systematics). The results of the model-independent atmospheric neutrino spectrum fit are then discussed, concluding with the results of the measurement of the K/π fit.

8.1 Data/MC Agreement check: 10% Subset Sample Fit

As a test of the analysis method, the fit was performed against small subset of the final sample (10% of the final data set, randomly selected, as is typical in IceCube analyses). The 10% subset sample fit also provides a cross-check of the data/MC agreement.

The resultant modified χ^2 test statistic distribution for 750 fluctuated best fit realizations of the MC is shown in Figure 8.1. The best fit to the 10% subset sample has a test statistic value of 115.5; a p-value of 0.8 (see Figure 8.2). This suggests a good fit and thereby a good data/MC agreement.

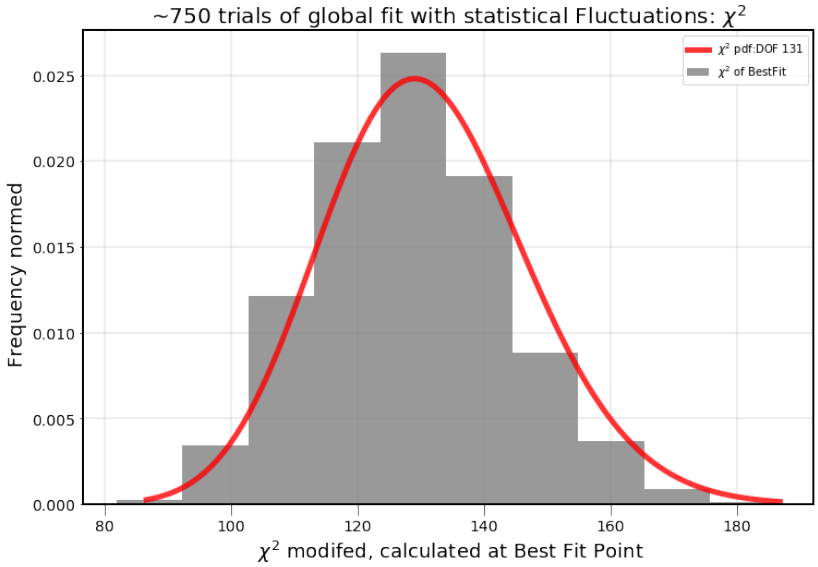

Figure 8.1: Showing the test-statistic, a modified χ^2, for 750 best fits of statistically fluctuated realizations of the MC. The fit performed on the 10% subset sample data has a test statistic result value of 115.5.

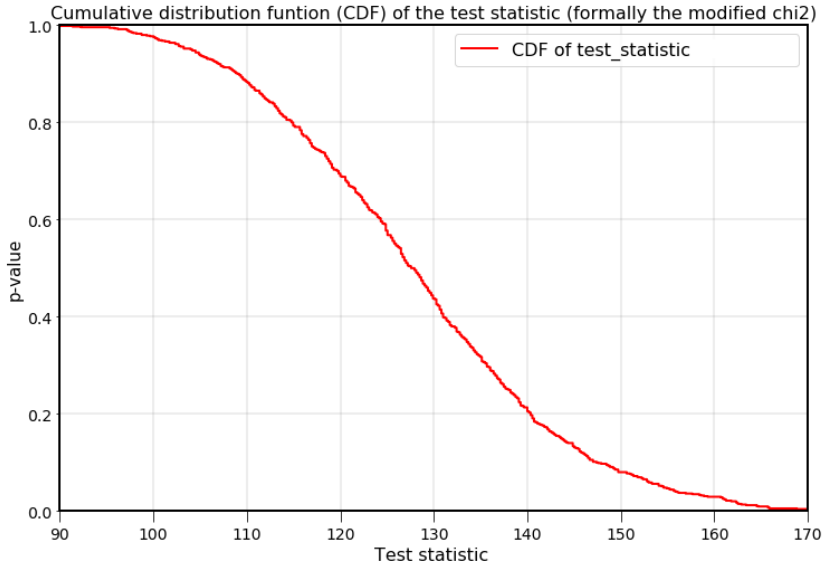

Figure 8.2: Showing the 1-CDF of the test-statistic for the 10% subset sample fit, a modified χ^2, for 750 best fits of statistically fluctuated realizations of the MC. The fit performed on the 10% subset sample data has a test statistic result value of 115.5, giving a p-value of $\sim$0.8.

8.2 A - Model Dependent Results

Here we present the results of the model-dependent tests. These results follow from the fitting procedure described in the previous chapter and includes the cross-section uncertainties, the atmospheric neutrino oscillations (nuisance parameters) uncertainties, the detector systematics (including ice-related systematics), and the atmospheric muon background. Since we want to test specific atmospheric neutrino flux models in this analysis, we do not vary parameters related to the flux; they are instead defined by the neutrino flux (energy and zenith distribution) predicted by the models. The results of the fit to the final data set are shown in table 8.1.

Table 8.1: Atmospheric neutrino flux models tested, with tables made for this analysis using MCEq [4]. The experimental data is compared to all permutations below via hypothesis test. GH = Gaisser-Honda, H3a = Hillas model, GSF = Global Spline Fits.

Hadronic int. model :	**CR primary Model** :		
	GH	H3a	GSF
DPMJET-III	6.17 σ	4.31 σ	6.55 σ
DPMJET-III-2017.1	6.34 σ	3.79 σ	4.42 σ
EPOS-LHC	5.42 σ	4.37 σ	7.23 σ
qgsjet II 04	6.33 σ	4.38 σ	7.53 σ
SYBILL 2.3c	5.75 σ	4.39 σ	7.05 σ
SYBILL 2.1	9.81 σ	11.9 σ	11.5 σ
HONDA 2015			3.90 σ

In addition to these models, we tested our data against the atmospheric neutrino flux tables 'HKKM2014' (by Honda et al.) for the South Pole [5]. Note that Honda's tables are year averaged and we have chosen to following this convention in all flux tables generated for this analysis.

From Table 8.1 one obtains the resultant probable agreement of the data sample with the models represented by the combination of cosmic ray spectrum model (columns: GH, H3a and GSF) and hadronic interaction models (rows: DPMJET-III, DPMJET-III-2017.1, EPOS-LHC etc). The most probable model set compared to the IceCube-

DeepCore sample is the combination of the hadronic interaction model DPMJET-III and the cosmic ray spectrum predicted by Hillas (H3a) model. The resultant parameters of the fit for this combination are shown in Table 8.2 and the full sets of resultant parameters for every model can be found in Appendix F.1.

Table 8.2: Showing detailed fit results for most probable model given the IceCube-DeepCore analysis sample. Hadronic model: DPMJET-III-2017.1 and the cosmic ray spectrum predicted by H3a (Hillas model). The 1 σ (68% CL) profile error on the data best fit is reported where applicable, calculated with the χ^2_m test statistic by profiling over all other variables. A total of 49967.0 events in are data fit, with 49799.6 expected events in MC.

Parameters in the fit	**Prior**	**Best fit point**
Oscillation parameters (nuisance):	N.H.	
Δm^2_{31} [eV$^2 \times 10^{-3}$]	no prior	2.4 ± 0.1
$\sin^2(\theta_{23})$	no prior	0.544 ± 0.005
$\sin^2(\theta_{13})$	0.0238 ± 0.0001	0.0240 ± 0.0001
Detector:		
overall optical eff. [%]	100 ± 10	108 ± 4
rel. optical eff., lateral (hole ice) [m]	0.02 ± 0.01	0.017 ± 0.003
rel. optical eff., head-on (hiFwd) [a.u.]	no prior	-0.8 ± 0.5
Flux and cross-section parameters:		
Neutrino event rate [% of nominal (livetime)]	no prior	2.70 yrs (*i.e.* 100%)
NC relative normalization [%]	100 ± 20	97 ±11
M_A^{res} [σ]	0.0 (central value) ±1σ	-1.6 (σ away)
Background:		
Atm. μ contamination [% of sample]	no prior	5.3 ±0.6
Test statistic (best fit):		
χ^2_{mod} (modified χ^2 [3])	no prior	193.6

8.3 B - (Quasi) Model-Independent Result

This section shows results from the energy spectrum and K/π measurements from case study B; the quasi model-independent characterization of the atmospheric neutrino flux. A spectral unfolding of the experimental data from $\sim$1 GeV to 1 TeV in true neutrino energy was performed, where ν_μ and ν_e events are separated using our PID (see 6.3). We find competitive results, consistent with existing global values (see Chapter 9), with a resultant spectrum than cannot be described with a simple power law. The test statistic value from the fit is 140.9, or a p-value of 0.2, indicating a good fit and good data/MC agreement (see Table 8.3). Note, the neutrino event rate and the segment fraction rates are correlated (see Chapter 9). As such, when plotting the fraction energy segments a scaling factor of 3.22/2.70 (the fitted event rate over the detector livetime) is used to account for this correlation. The error on the fitted energy segment fractions is calculated by fixing a given fraction and profiling over all other fit parameters. The resultant profile scan is evaluated at the 1σ-level and the relative error is assessed. The profile scans are not symmetric and, in the comparison to Super-Kamiokande and global results, this is reflected in asymmetric y-errors for our measurement (see Figure 9.2).

As an example, Figure 8.3, shows a simple curve fit algorithm used to find the central value at $\Delta\chi^2 = 0$ and, subsequently, the values of the profile curve at $\Delta\chi^2 = 1$ (1σ uncertainty). This curve is slightly asymmetric, providing 1 σ error bounds of 0.053 and 0.062. These are then calculated as a relative (percent) error for the extracted spectrum. The fraction of events in a given energy segment is then translated into a normalization and scaled by the fitted livetime/detector livetime.

There is limited sensitivity to the K/π ratio in this fit due to low statistics in the sample at higher energies and a fit result that dominantly finds pions as the primary neutrino parent meson for the events in the sample. The spectrum unfolding segments have uncertainties ranging in size from $\sim$8% to 33% relative error (see Table 8.3 and Figure 8.4 and 9.2). The mid-range energy segments are competitive with

Super-Kamiokande's current leading results 9.2] and this analysis contributes new information here and at the higher energies where the previous spectrum measurements were lacking.

Table 8.3: Showing detailed fit results from the model independent unfolding of the atmospheric neutrino spectrum and the quasi-model independent fit of the K/π ratio with the IceCube-DeepCore analysis sample. (Hadronic model: DPMJET-III and the cosmic ray spectrum predicted by H3a – Hillas model). The 1σ profile error on the data best fit is reported where applicable, calculated with the χ^2_m test statistic by profiling over all other variables. A total of 49967.0 events are in the data fit, and 49847.0 expected events in MC fit output.

Parameters in the fit	**Prior**	**Best fit point**
Oscillation parameters (nuisance):	N.H.	
Δm^2_{31} [eV$^2 \times 10^{-3}$]	no prior	2.5± 0.1
$\sin^2(\theta_{23})$	no prior	0.410 ± 0.005
$\sin^2(\theta_{13})$	0.0238 ± 0.0001	0.0240 ± 0.0001
Detector:		
overall optical eff. [%]	100 ± 10	97 ± 4
rel. optical eff., lateral [cm^{-1}]	0.02 ± 0.01	0.021 ± 0.004
rel. optical eff., head-on [a.u.]	no prior	-0.2 ± 0.5
Flux and cross-section parameters:		
NC relative normalization [%]	100 ± 20	91 ±11
M_A^{res} [σ]	0.0 (central) ± 1	-0.4 (σ away)
Background:		
tm. μ contamination [% of sample]	no prior	6.8 ± 0.7
Measurement:		
K/π fraction [% of nominal]	no prior	20
Fraction of events – ν_μ:		[% of total sample]
Frac1: ν_μ 1-9 GeV (%)	no prior	12.6 ±2.7
Frac2: ν_μ 9-15 GeV (%)	no prior	12.1 ± 2.3
Frac3: ν_μ 15-25 GeV (%)	no prior	15.9 ± 1.3
Frac4: ν_μ 25-40 GeV (%)	no prior	10.1 ± 0.7
Frac5: ν_μ 40-70 GeV (%)	no prior	9.6 ± 0.7
Frac6: ν_μ 70-120 GeV (%)	no prior	5.8 ± 0.5
Frac7: ν_μ 120-1000GeV (%)	no prior	3.6 ± 1.0
Fraction of events – ν_e:		
Frac8: ν_e 1-9 GeV (%)	no prior	7.6 ± (2.2, -1.7)
Frac9: ν_e 9-15 GeV (%)	no prior	9.5 ± (1.5, -1.7)
Frac10: ν_e 15-30 GeV (%)	no prior	8.4 ± (1.1, -1.2)
Frac11: ν_e 30-70 GeV (%)	no prior	3.5 ± 1
Frac12: ν_e 70-1000 GeV (%)	no prior	1.8 ± (3.3, 1.5)
Neutrino event rate [% livetime)]	no prior	3.22 yrs (*i.e.* 120)
Test statistic (best fit):		
χ^2_{mod} (modified χ^2 [3])	no prior	140.9

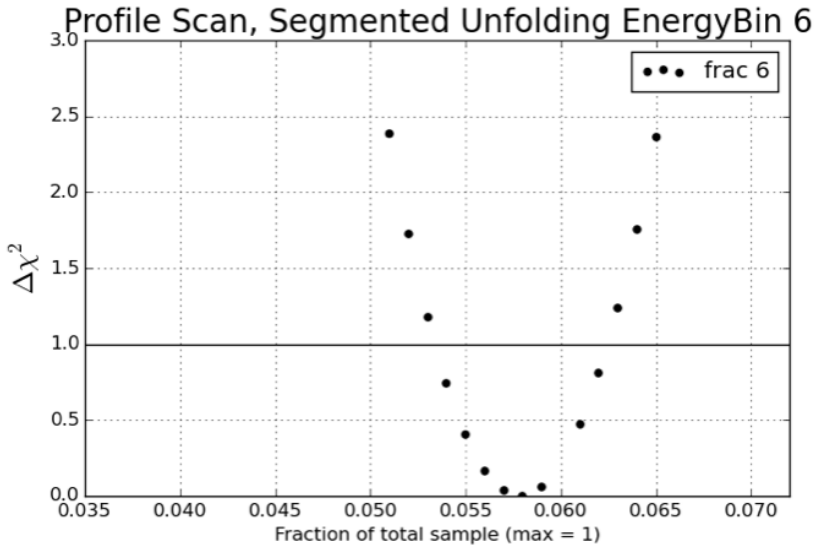

Figure 8.3: Showing the scan of atmospheric neutrino fraction for energy segment 6 (70 – 120 GeV), produced by profiling over all other variables. Here the fit finds 5.8 $\pm$ 0.5 % of the sample in this bin, giving a relative error of 8.6% on on this fraction.

As noted above, the results indicate that the ν_μ component in the data sample primarily arises from pions, with the fit preferring 80% more pions than the nominal prediction with a 68% uncertainty at the 1σ. We note that at $\sim$70 GeV, the uncertainty in the kaon production in hadronic interaction models is large (order 40%) [12]. Insufficient high-energy events in this sample makes measuring the K/π ratio challenging.

It therefore appears there may not be enough high energy events in the 2.7 years of data livetime to make a precise measurement of the K/π ratio (see Figure 8.5). With an uncertainty on the K/π ratio of 68% at 1σ for a suggested high pion fraction, the measured value of neutrinos from a kaon parent with respect to the nominal prediction (DPMJET-III + h3a) is reduced by 40%. This exceeds our predicted sensitivity of 38%, based on the K/π ratio fitting at the nominal (model predicted) value; *i.e.* a lower pion fraction than suggested by this fit to the data sample.

We note that a 10% increase in the pion fraction from the nominal production produces a reduction of $\sim$4% in sensitivity due to the K/π production crossover energy

point increasing.

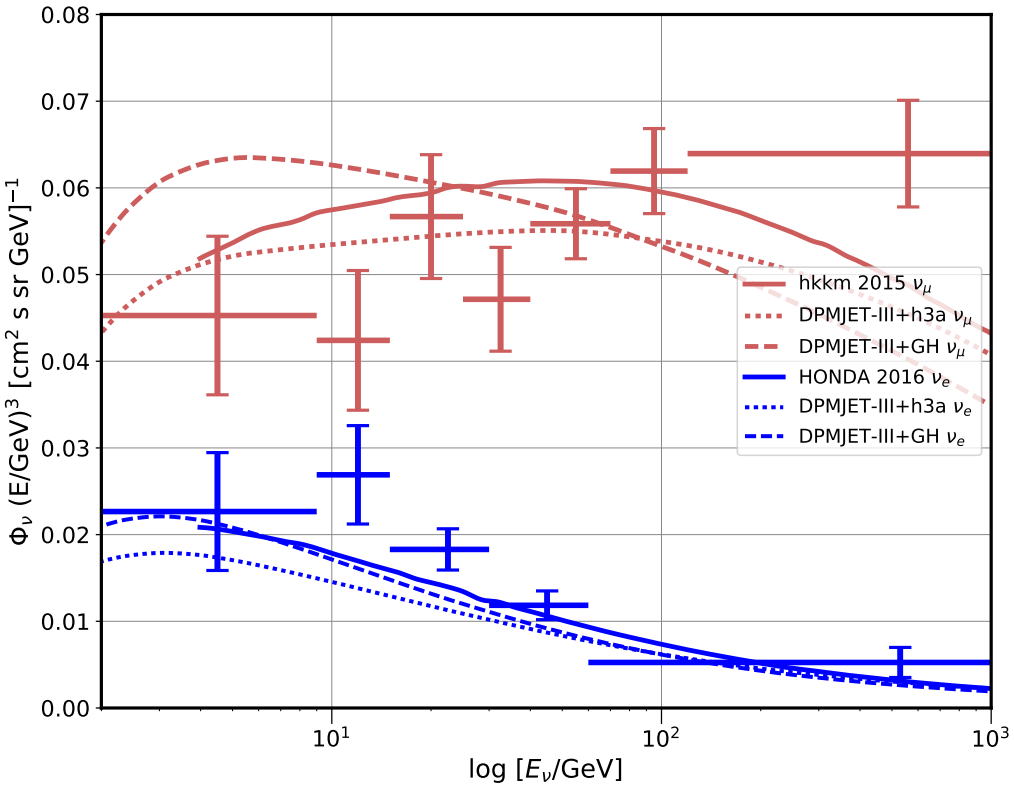

Figure 8.4: Showing the resultant unfolded atmospheric neutrino flux from this analysis. The vertical error bars are 1σ (stat.+syst.), while the horizontal error bars show the true energy range of the unfolded bins. Note that ν_μ is shown in red, and ν_e in blue. Lines show model expectations as per the legend.

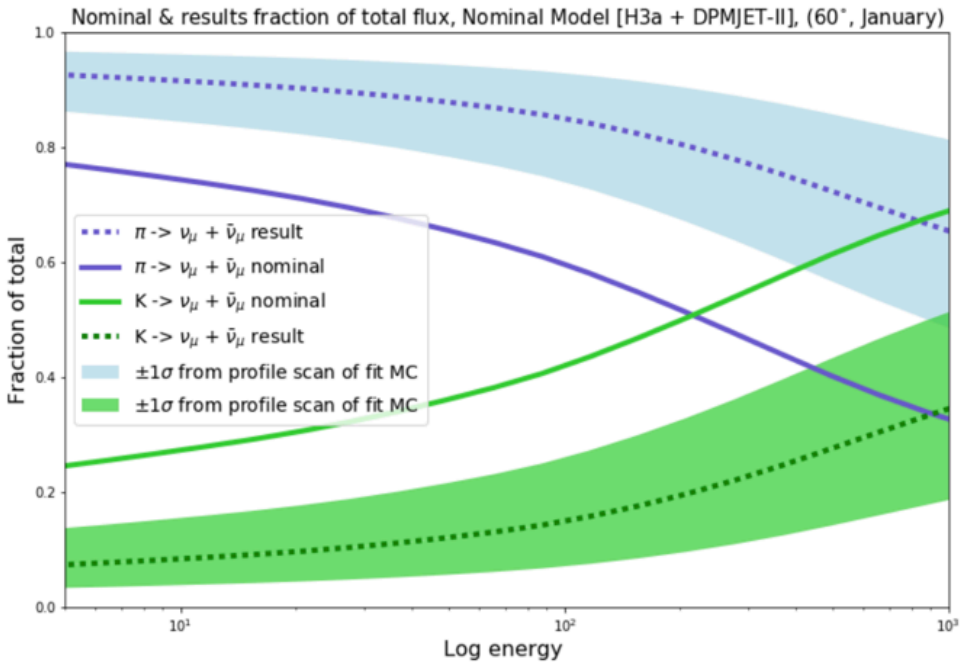

Figure 8.5: Showing the fractional contribution to neutrinos from the first atmospheric meson, either pions or kaons. Dashed lines show the outcome of the fit for each component overlain with the 1σ uncertainties. The nominal model prediction (from DPMJET-III + h3a) is shown as the solid lines.

Chapter 9

Discussion and Outlook

With the highest statistic atmospheric neutrino sample available to date, a binned analysis has been performed to obtain model-dependent and (quasi) model-independent measurements of the atmospheric neutrino flux. The model-dependent tests (case study A) find that, of the current atmospheric neutrino flux models considered, DPMJET-III.2017 combined with the cosmic ray spectrum from H3a provides the most probable agreement with the IceCube data set analyzed here. It is noteworthy that a newly created (2018) data-driven cosmic ray model Global Spline Fits (GSF) [58] closely follows H3a in terms of the cosmic ray model preference by the data. Further, the new generation of hadronic interaction models that take into account the 7 TeV LHC data are also preferred in the fit to our data to those that do not; most notably in the case of the SIBYLL model series where the creators have worked to improve the kaon-related momentum space [4] .

The (quasi) model-independent study (case study B) provided a test statistic from the fit of 140.9 (p-value of 0.2), indicating reasonable data/model agreement. Further, as expected from the fit results, the obtained values of the systematic parameters at the best fit point are within the uncertainties of the nominal values. An interesting output from the fit are the atmospheric oscillation parameters that result. The extracted parameters at the best fit point are within the 90% CL of the most recently

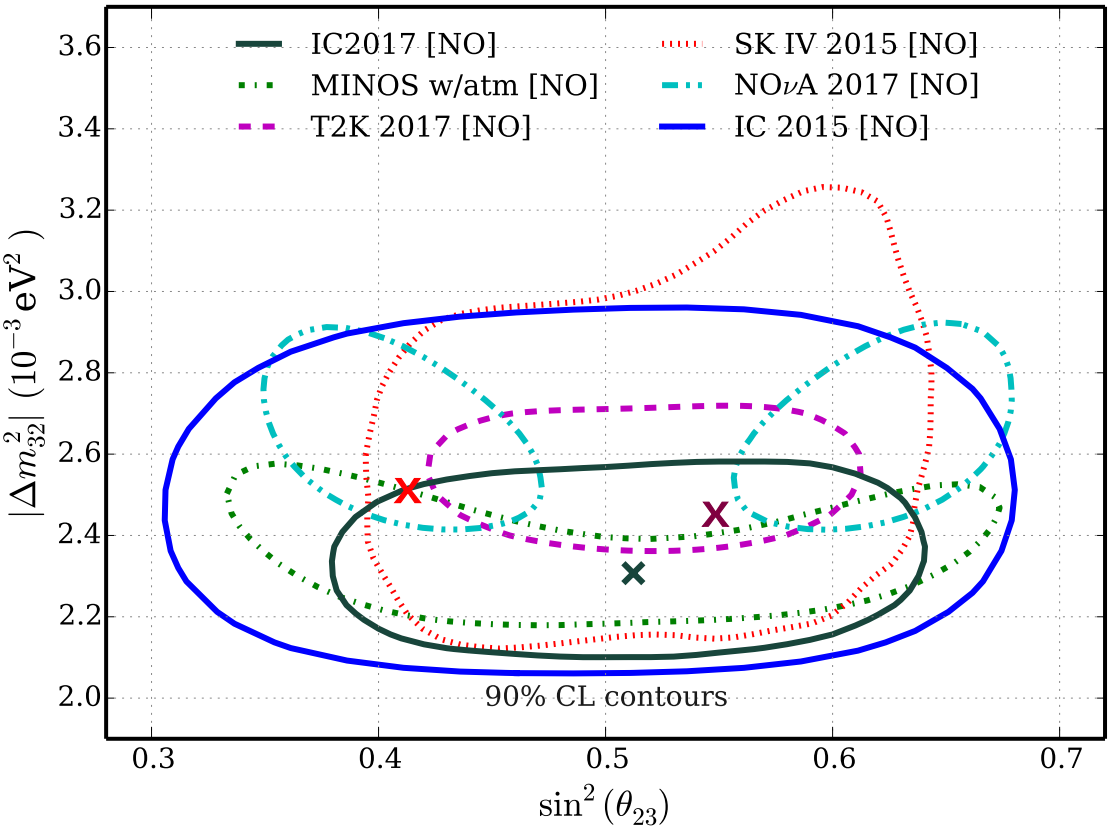

Figure 9.1: The 90% allowed region from the most recent IceCube oscillation analysis [3] (IC2017 in green) compared to other experiments [67] [68] [69] [70] (dashed lines). This analysis used the same data set below the reconstructed neutrino energy of 56 GeV. The green central cross marks the best-fit point from [3]. The purple and orange crosses show the best-fit points from case studies from analysis A and B, respectively.

published IceCube results (see Figure 9.1) [3]. It is important to note in this case that the previous work included atmospheric neutrino systematics that were not flux preserving, which is not the case in this result.

Control over the systematic uncertainties was key to the outcome of the analysis; in particular the potential backgrounds from atmospheric muons, for which there was no selected prior in the fit. The atmospheric muon contamination was found to be $\sim 5\%$ in case study A, which compares well with the MC estimations that indicated the value is close to 5%. Guidance from a previous IceCube study [3] provided a similar expectation. The model input in the case study A best fit is similar

to HKKM2014 (same hadronic interaction model, but without muon charge ratio calibration, similar cosmic ray model, same atmospheric density model) and obtaining a similar atmospheric muon fraction provides confidence in the result. Similarly in case study B, the atmospheric muon fraction is found to be 6.8%, within reasonable expectations from the comparable low-energy analyses.

9.1 Comparison to the Global Picture

As a final step, we show the results of this analysis (case study B) in the context of available measurements in the global community (see Figure 9.2). Compared to IceCube-DeepCore's previous measurement, we extend the sensitivity down to 1 GeV true neutrino energy (5.6 GeV reconstructed neutrino energy) from 100 GeV in ν_μ [1] and 80 GeV in ν_e [2]. Of particular note, the mid-range energy segments in this analysis are competitive with the global best results and explore an important energy regime that has been previously lacking in precision measurements of the spectrum. We also note that a cosmic ray model with a flatter spectrum in our energy range is preferred by the considered models (H3a, GSF). Honda *et al.*'s relatively new model HKKM2014 also preforms well, having similarities to the best-fit model. We note, however, that no model fits with the IceCube data to better than $\sim 3.79\sigma$, and so caution is recommended when using the best fit model from IceCube, and to carefully consider the model uncertainties. The atmospheric neutrino flux also effects the values of the atmospheric neutrino oscillations and clearly there is more work to be done in model refinement. It is key to be aware of the discrepancies between even the most favoured atmospheric neutrino models and our IceCube data. We conclude that the differences between the fluxes predicted by these models and our data are statistically significant.

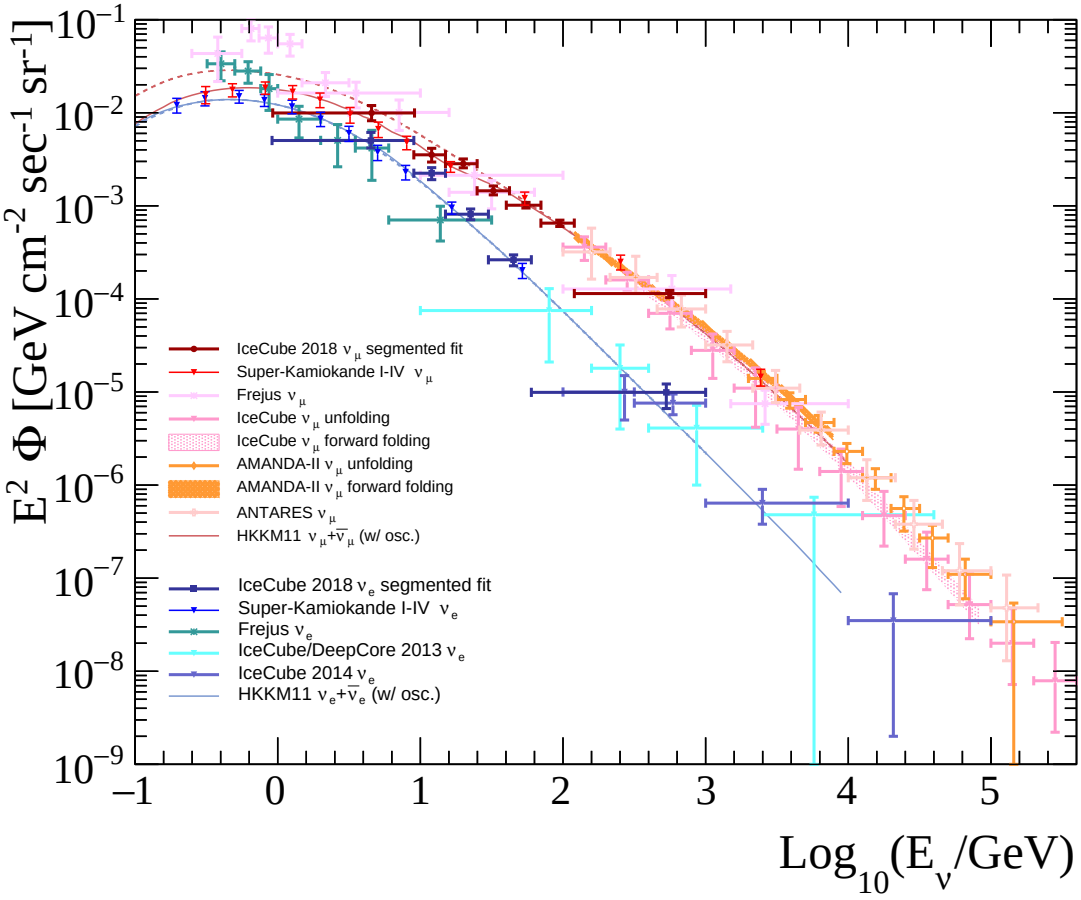

Figure 9.2: Showing the atmospheric neutrino energy spectrum of ν_μ and ν_e. The dark blue and red bars and points show Ice-Cube-DeepCore 2018 (this work) and contain all systematics and uncertainties with the measurement. The energy spectra of the atmospheric fluxes by SKI-V [13], Frejus [71], AMANDA-II [40] [72], IceCube [1] [2] and ANTARES [73] are shown. The HKKM11 [74] flux model predictions for the shown in solid (with oscillation) and dashed (without oscillation) lines.

9.2 Future Considerations

There are a number of potential improvements that have been recognized at the late stages of the development of the presented analysis and are briefly discussed here.

Analysis-centric improvements would be focused on increasing the statistical sample in key energy regions and augmenting the efficiency of the particle identification algorithms. Improved PID is particularly critical to improving the knowledge of the individual ν_μ and ν_e spectrum measurements at lower energies. Further, due to the current limitations of the PID, the neutrino fractions in the lower energy segments are highly correlated. As can be seen in Figure 9.3, in the lowest 2 energy segments (0-9 GeV and 9-15 GeV) the correlations between are 97% and 54%, respectively. The correlations indicated that our PID currently has little to no separation below 9 GeV, and limited separation below 25 GeV (reconstructed neutrino energy). This impacts the results since although the models predict a smooth spectrum at this energy, that is not what is measured. A future adaptation to the analysis would be to implement a regularization that would enhance the capability of the PID at these lower energies, with the potential that this step would introduce some loss of information on the spectral features. It is also noteworthy that the extracted ν_e flux is higher than expected; potentially related to ν_μ events from kaons being misidentified as ν_e. Currently in the fit the ν_e and ν_μ spectra are free to float with respect to one another. However, we have prior knowledge the spectra are linked that has not yet been incorporated, and would add power to better constrain the (mis)identification of those events and therefore the spectrum of the flux.

Specifically related to the K/π ratio and the related spectral fit, it is clear the measurement may be improved with the addition of a higher energy data set so as to include more high-energy (kaon parent) events; constraining the current pion component over-prediction observed in the results. In addition, more freedom in the K/π spectrum fit is currently required. The particle distribution shapes may be relaxed, in place of the strict criteria that they must follow a global shape from the

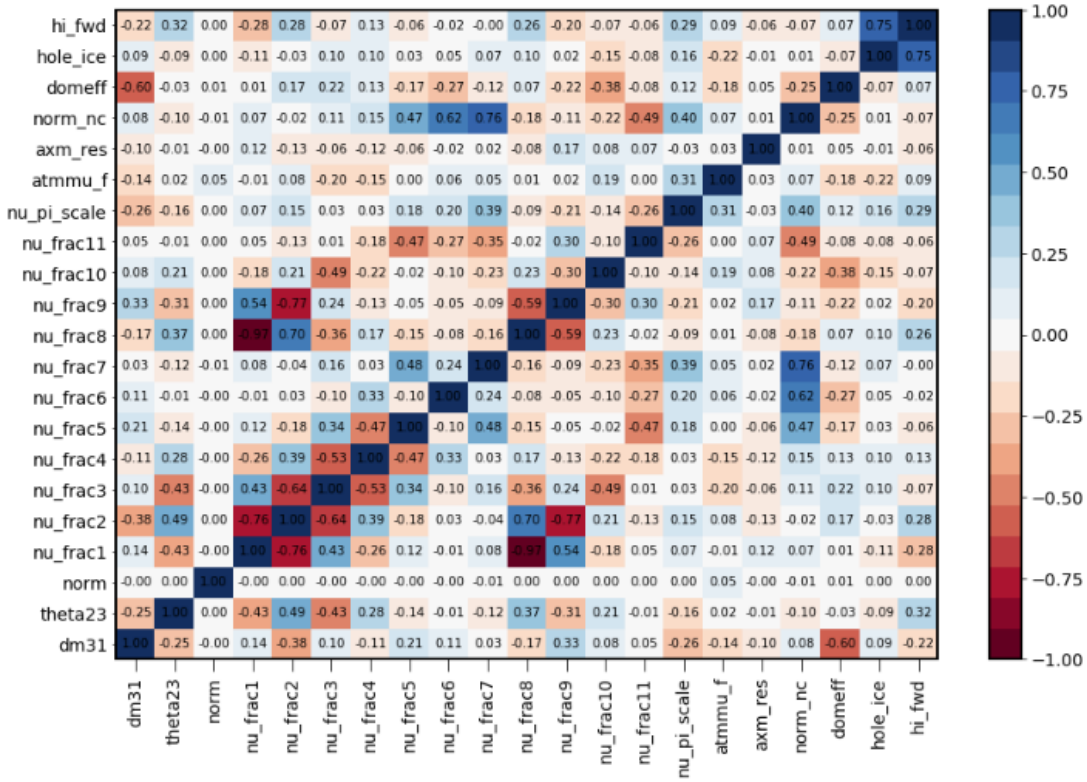

Figure 9.3: Showing the full correlation matrix (z-colour scale) from the Asimov fit of MC simulation data for the case study B analysis. This plot gives the expected analysis correlations. Note: 'Nu frac' 1-7 represent the ν_μ fractions, and 'Nu frac' 8-11 represent the ν_e fractions. The lowest energy bins in ν_μ and ν_e are highly correlated (97%) implying almost no PID separation in these two neutrino event fraction parameters in the fit.

underlying model, to facilitate this. For the leading atmospheric production models, there are a number of anticipated future improvements. At lower energies, only the DPMJET-III models are currently relevant. As such, the MCEq simulation platform is patched below 30 GeV with interpolations to models that start near 60 GeV. By extending this analysis with a higher energy sample, the impact of this interpolation of the DPMJET-III model may be explored. Additionally, the models considered in this analysis can be divided into the individual contributions from the pion and kaon parents; an extended sample utilized in an iterative fit would permit ratio tests of each model separately.

The precision measurement of the atmospheric neutrino flux, and hence the K/π ratio, remains of significant interest for the broad experimental and theoretical communities. With the increased statistics available from continued IceCube-DeepCore operation, and improvements in the knowledge of the detector systematics (via advanced calibrations of the *in situ* DOM efficiency and local ice properties), there is potential for significant improvement to the results reported in these initial analyses. Combining this with steadily improved measurements abroad, *e.g.* the muon charge ratio provided by the BESS balloon experiment [75] [76], provides unique and complementary approaches for determining the K/π ratio over a large energy range. For future measurements with atmospheric neutrinos, including those involving precision studies of the neutrino properties, it is expected the results of the analysis presented here will prove to be key input parameters for a previously sparsely studied and crucial energy regime.

Bibliography

[1] IceCube Collaboration, Measurement of the ν_μ energy spectrum with IceCube-79 Eur. Phys. J. C (2017) 77: 692.

[2] IceCube Collaboration, Measurement of the Atmospheric ν_e flux in IceCubePhys. Rev.Lett. 110 (2013) no.15, 151105

[3] IceCube Collaboration, Measurement of Atmospheric Neutrino Oscillations at 6?56 GeV with IceCube DeepCore Phys. Rev. Lett. 120, 071801 2018. arXiv:1707.07081

[4] A. Fedynitch, R. Engel, T. K. Gaisser, F. Riehn and T. Stanev, EPJ Web Conf. 99, 08001 2015

[5] M. Honda *et al.*, Phys. Rev. D 92, 023004 2015

[6] T.K. Gaisser, R. Engel, E. Rescind, Cosmic Rays and Particle Physics, Cambridge University Press, Great Britain 2016

[7] FermiLab, http://www.fnal.gov/pub/inquiring/matter/madeof/index.html

[8] Particle Data Group. Journal of physics G. Nuclear and Particle Physics, Vol 37, No 7A 2010

[9] Super-Kamiokande Collaboration, Y. Fukuda *et. al.*, Evidence for Oscillation of Atmospheric Neutrinos, PRL 81, 1562 1998

[10] The SNO Collaboration, Measurement of the rate of e+d, p+p+e- interactions produced by 8B solar neutrinos at the Sudbury Neutrino Observatory Phys. Rev. Lett. 87, 071301 2001

[11] nufit 2.0, 2014, http://www.nu-fit.org/?q=node/92

[12] G. D. Barr, T. K. Gaisser, S. Robbins and T. Stanev, Phys. Rev. D 74 094009 2006

[13] Super-Kamiokande Collaboration, Measurements of the atmospheric neutrino flux by Super-Kamiokande: Energy spectra, geomagnetic effects, and solar modulation Phys. Rev. D 94, 052001 2016

[14] Neutrino Physics, K. Zuber, Taylor and Francis, 2012

[15] Cosmic Rays and Particle Physics, Cambridge University Press,T. K. Gaisser, Great Britain 1990

[16] http://www.hap-astroparticle.org/184.php

[17] S. Tilav, Bartol Research Institute and UDeleware, SUGAR2015

[18] A. Fedynitch, R. Engel, T.K. Gaisser, F. Riehn and T. Stanev, PoS(ICRC2015)1129 2016

[19] A. Fedynitch, 7th Open meeting for Hyper-Kamiokande, London 2016

[20] IceCube MasterClasses lecture 'detecting neutrinos 2017

[21] T. K. Gaisser and M. Honda, Ann. Rev. Nucl. Part. Sci. 52, 153 2002

[22] A. Fedynitch and R. Engel in Proceedings, 14th Int. Conf. Nuclear Reaction Mechanisms, Varenna, 2015, p. 291, https://cds.cern.ch/record/2114737

[23] S. Roesler, R. Engel and J. Ranft, The Monte Carlo event generator DPMJET-III, Monte Carlo 2000

[24] P. A. Cherenkov, Visible radiation produced by electrons moving in a medium with velocities exceeding that of light, Phys Rev 52:378-379, August 1937

[25] J.D.Jackson, Classical Electrodynamics, Third Edition, published by Wiley 1999

[26] I. Fank and I. Tamm. Coherent visible radiation from fast electrons passing through matter. C. R. Acad. Sci. USSR, 14:109-114, 1937

[27] R. Radel and C. Wiebusch. Calculation of the Cherenkov light yield from low energetic secondary particles accompanying high energy muons in ice and water with GEANT4 simulations. Astropart. Phys. 38:53-67, 2012

[28] IceCube Collaboration,R. Abbasi et al., The Design and Performance of IceCube-DeepCore, Astropart. Phys. 35, 1109.6096 2012

[29] K. A. Olive et al. (Particle Data Group Collaboration). Passage of particles through matter. Chinese Physics C, 38(090001), 2014

[30] Image D.Grant, IceCube Collaboration

[31] M. Dunkman, Measurement of Atmospheric Muon Neutrino Disappearance with IceCube-DeepCore, Doctor of Philosophy dissertation, May 27, 2015, https://etda.libraries.psu.edu/catalog/27226

[32] Image by the IceCube Collaboration, NSF

[33] IceCube collaboration, Optical properties of deep glacial ice at the South Pole. Journal of Geophysical Research: Atmospheres, 111(D13), 2006. doi:10.1029/2005JD006687

[34] IceCube collaboration, Nucl. Instrum. Methods Phys. Res., Sect. A 601, 294 2009

[35] IceCube collaboration, Nucl. Instrum. Methods Phys. Res., Sect. A 618, 139 2010

[36] IceCube Collaboration. The design and performance of the IceCube-DeepCore detector. Astropart. Phys., 35(10):615?624, 2012. doi:10.1016/j.astropartphys.2012.01.004

[37] Sebastian Euler Observations of Oscillations of Atmospheric Neutrinos with the IceCube Neutrino Observatory (Thesis) Ph.D. thesis, Rheinisch-Westf¡8a¿lische Technische Hochschule (RWTH) Aachen, Germany, October 2013

[38] P. B. Price, K. Woschnagg, and D. Chirkin. Age vs depth of glacial ice at South Pole. Geophysical Research Letters, 27(14):2129?2132, 2000. doi:10.1029/2000GL011351

[39] [4] R. Greve. The Dynamics of Ice Sheets and Glaciers Lecture Notes, Institute of Low Temperature Science, Hokkaido University (2004)

[40] R. Abbasi et al. (IceCube), Phys.Rev. D79, 102005 2009, arXiv:0902.0675 [astro-ph.HE]

[41] D. Chirkin for the IceCube Collaboration, Evidence of optical anisotropy of the South Pole ice, ICRC 2013, arXiv:1309.7010

[42] J. L. Kelley (IceCube Collab.), AIP Conf. Proc.1630, 154 2014

[43] J.P. Yanez, Measurement of neutrino oscillations in atmospheric neutrinos with the IceCube DeepCore detector, Doctor of Philosophy dissertation, https://d-nb.info/1058165291/34

[44] M. Honda *et al.*, Phys. Rev. D 92, 023004 2015

[45] C. Andreopoulos et al., Nucl. Instrum. Meth. A614, 87 2010, arXiv:0905.2517 [hep-ph], version GENIE 2.8.6 - icetray

[46] J.-H. Koehne, K. Frantzen, M. Schmitz, T. Fuchs, W. Rhode, D. Chirkin, and J. B. Tjus, Comput. Phys. Commun. 184, 2070 2013

[47] S.Agostinelli, Geant4 simulation toolkit, Nucl. Instrui. Meth, Vol. 506, 3, 1 2003

[48] L. Radel, Masters thesis, Rheinisch-Westflischen Technischen Hochschule 2012

[49] https://github.com/claudiok/clsim.

[50] D. Heck et al., CORSIKA: a Monte Carlo code to simulate extensive air showers (Forschungszentrum Karlsruhe GmbH, Karlsruhe, Germany, 1998), http://inspirehep.net/record/469835/files/FZKA6019.pdf

[51] IceCube Collaboration, M.G. Aartsen et al., Determining neutrino oscillation parameters from atmospheric muon neutrino disappearance with three years of IceCube DeepCore data, Phys. Rev. D, 91, 072004 2015

[52] Neutrino Generator (NuGen). Neutrino event simulator developed by the IceCube Collaboration.

[53] Upcoming IceCube collaboration publication on NuTau appearances from 5-56 GeV (paper)

[54] MultiNest v 3.10, F. Feroz, M. Hobson, arXiv:0704.3704, arXiv:0809.3437 arXiv:1306.2144 Released Jul 2015

[55] From eV to EeV: Neutrino Cross-Sections Across Energy Scales. J.A., Formaggio, G. P. Zeller, Rev.Mod.Phys. 84 (2012) 1307-1341 arXiv:1305.7513 [hep-ex] FERMILAB-PUB-12-785-E arXiv:1305.7513

[56] F.James and M.Roos, Comput. Phys.Commun. 10, 343 1975

[57] R. Wendell et al., http://www.phy.duke.edu/ raw22/public/Prob3++

[58] H. Dembinski, R. Engel, A. Fedynitch, T. K. Gaisser, F. Riehn and T. Stanev, Data driven model of the cosmic-ray flux and mass composition from 10 GeV to 10^{11} GeV PoS, ICRC 2017

[59] A. M. Hillas, arXiv:astro-ph/0607109

[60] S. Roesler, R. Engel and J. Ranft, The Monte Carlo event generator DPMJET-III in Proc. of Int. Conf. on Advanced Monte Carlo for Radiation Physics, Particle Transport Simulation and Applications (MC 2000),

[61] T. Pierog, I. Karpenko, J. M. Katzy, E. Yatsenko and K. Werner, EPOS LHC: Test of collective hadronization with data measured at the CERN Large Hadron Collider, Phys. Rev. C92 2015 034906, [1306.0121]

[62] S. Ostapchenko, Total and diffractive cross sections in enhanced Pomeron scheme, Phys. Rev. D81 2010 114028, [1003.0196].

[63] F. Riehn, R. Engel, A. Fedynitch, T. K. Gaisser and T. Stanev, A new version of the event generator Sibyll, 1510.00568.

[64] E.-J. Ahn, R. Engel, T. K. Gaisser, P. Lipari and T. Stanev, Cosmic ray interaction event generator SIBYLL 2.1, Phys. Rev. D 80 (2009) 094003, [0906.4113].

[65] T. Pierog, I. Karpenko, J. M. Katzy, E. Yatsenko and K. Werner, Phys. Rev. C 92, 034906 2015

[66] F. Riehn, R. Engel, A. Fedynitch, T. K. Gaisser and T. Stanev, PoS(ICRC2015)558 2016

[67] P. Adamson et al. (MINOS), Phys. Rev. Lett. 110,251801 (2013), 1304.6335

[68] K. Abe et al. (T2K), Phys. Rev. Lett. 118, 151801 2017, arXiv:1701.00432

[69] P. Adamson et al. (NOvA), Phys. Rev. Lett. 118, 151802 2017 arXiv:1701.05891

[70] R. Wendell (Super-Kamiokande), AIP Conf. Proc. 1666,100001 2015, arXiv:1412.5234

[71] K. Daum (Frejus.), Z. Phys. C66, 417 1995

[72] R. Abbasi et al. (IceCube), Astropart.Phys. 34, 48 (2010), arXiv:1004.2357 [astro-ph.HE]

[73] S. Adrian-Martinez et al. (ANTARES), Eur. Phys. J. C73, 2606 (2013), [Eur. Phys. J.C73,2606(2013)] arXiv:1308.1599 [astro-ph.HE]

[74] Phys. Rev. D83, 123001 2011

[75] T. Sanuki, M. Motoki, H. Matsumoto, E. Seo, J. Wang, et al., Astrophys.J. 545, 1135 (2000), arXiv:astroph/0002481 [astro-ph]

[76] S. Haino, T. Sanuki, K. Abe, K. Anraku, Y. Asaoka,et al., Phys.Lett. B594, 35 (2004), arXiv:astroph/0403704 [astro-ph]

[77] Personal correspondence, Logan Sibley

[78] J.L. Hewett, H. Weerts, R. Brock, J.N. Butler, B.C.K. Casey, et al. Fundamental Physics at the Intensity Frontier. arXiv:1205.2671 2012

[79] G. L. Fogli, E. Lisi, A. Marrone,D. Montanino, A. Palazzo, and A. M. Rotunno. Global analysis of neutrino masses, mixings, and phases: Entering the era of leptonic CP violation searches, Phys. Rev. D, 8:013 012, 2012. doi:10.1103/PhysRevD.86.013012

[80] NoiseEngine developed by the IceCube collaboration

[81] Thesis, E.Thomson (publication pending)

[82] A. Fedynitch, J. Becker Tjus and P. Desiati, Phys. Rev. D 86 114024 2012

[83] R. M. Ulrich et al., PoS(ICRC2015)407 2016

[84] K. Goulianos, FERMILAB-Conf-94/266-E 1996

[85] Cosmic Rays and Particle Physics, T. K. Gaisser, R. Engel, and E. Resconi, Cambridge University Press 2016

[86] Tangy Pierog. Air shower Simulation with a New Generation of post-LHC Hadronic Interaction Models in CORSICA, PoS (ICRC 2007) 1100

[87] K. Werner, F.-M. Liu and T. Pierog, Parton ladder splitting and the rapidity dependence of transverse momentum spectra in deuteron gold collisions at RHIC, Phys. Rev. C74 044902 2006 [hep-ph/0506232]

[88] S. Ostapchenko, On the re-summation of enhanced Pomeron diagrams, Phys. Lett. B636 2006 40-45, [hep-ph/0602139]

[89] TOTEM collaboration, Elastic Scattering and Total Cross-Section in p+ p reactions measured by the LHC Experiment TOTEM at sqrt s= 7 TeV, Prog.Theor.Phys.Suppl. 193 2012 180-183, [1204.5689]

[90] J. M. Picone, A. E. Hedin, D. P. Drob, and A. C. Aikin, NRLMSISE-00 empirical model of the atmosphere: Statistical comparisons and scientific issues, J. Geophys. Res., 107 (A12), 1468, 2002

[91] M. Honda, T. Kajita, K. Kasahara and S. Midorikawa, A New calculation of the atmospheric neutrino flux in a 3-dimensional scheme, Phys. Rev. D 70, 043008 2004

Appendix A

Neutrino Oscillation Physics

A natural consideration in measuring the atmospheric neutrino flux is what happens to the neutrinos after they are produced, until the point where they interact in the detector. It is now a well-established fact that neutrinos oscillate both in the vacuum and in matter [14]. Neutrinos travel in a superposition of their mass eigenstates, i.e. the flavour states that we experience through the weak interaction are not eigenstates of the energy operator. It is the mass states that propagate, not the flavour states. One can also think of this as each of the mass eigenstates having a mixture of ν_e, ν_μ, ν_τ, in different amounts (see figure A.1).

The oscillation of these neutrinos is a purely quantum mechanical effect that was first noted as a possible solution to the observations of the Homestake (Davis) experiment (1970 until 1994) [14] measurement of the ν_e solar neutrino flux produced in solar fusion processes. However, only one third of the predicted flux was measure, resulting in what became known as the 'solar neutrino problem' [14]. In 1998 the Super-Kamiokande experiment provided the first experimental measurement of atmospheric neutrino oscillations [9] and in 2001 the Sudbury Neutrino Observatory (SNO) experiment resolved the solar neutrino problem with a full solar flux measurement that demonstrated oscillation of solar neutrinos.

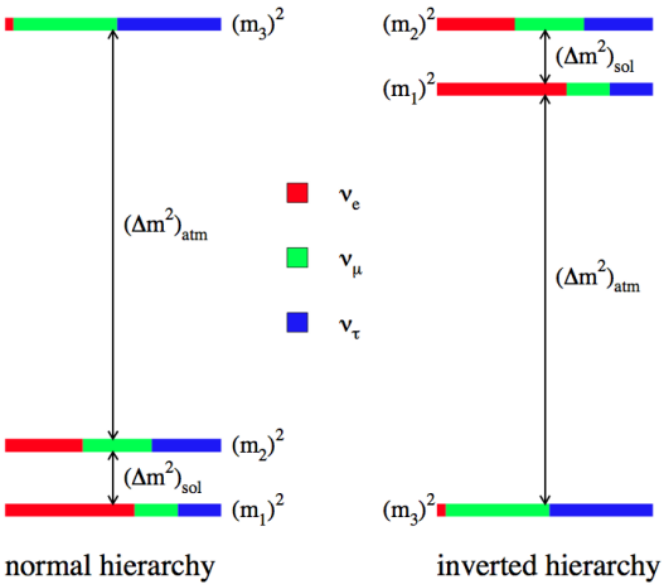

Figure A.1: Showing a pictorial representation of the flavour composition of each mass state and correspond to the values of the mixing angles θ_{ij}, with red for ν_e, green for ν_μ and blue for ν_τ. The smallness of θ_{13} relative to the other mixing angles can be seen by the small contribution of ν_e to the ν_3 mass state. The smallness of $\Delta m^2_{21} \equiv (\Delta m^2)_{sol}$ relative to Δm^2_{23} is not to scale and as the sign of $\Delta m^2_{23} \equiv (\Delta m^2)_{atm}$ is unknown, the figure shows both normal and inverted hierarchy [77] [78].

A.1 Conceptual Approach to Neutrino Oscillations

The discovery of neutrino flavour oscillations provided the first evidence for physics beyond the Standard Model in the last two decades. It has been mentioned previously in this document that the particle we call a 'neutrino' is a state that is produced in a weak interaction. In this way, it is by definition a flavour eigenstate, in the sense that a neutrino is always produced or created with the corresponding charged lepton, *i.e.* a ν_e is produced in partnership with an electron.

As observed in the CKM matrix in the quark sector [14], it is possible that these definite flavour states (ν_e, ν_μ, ν_τ) are not states of definite mass, i.e. they are not mass eigenstates. What this *implies* is that every time a muon is produced, for example, in a weak interaction, one of the mass eigenstates is also noted [77]. Let us imagine that we create a given mass state with a certain probability (different from

creating the other mass states, possibly, *i.e.* say we create v_1 only 20 percent of the time). If we could then resolve the mass state produced, we could follow each mass state as it propagates and we would not expect any oscillation between states. The neutrino masses are too light, however, for us to resolve with current experiments. That is, we can be sure we created a neutrino mass state, but not which one, so what we have created at the weak interaction vertex is a coherent superposition of the mass states, v_1, v_2, v_3. It is this coherent superposition that we call the 'muon neutrino' (ν_μ), e.g.

$$|\nu_\mu >= U_{\mu 1}|\nu_1 > + U_{\mu 2}|\nu_2 > + U_{\mu 3}|\nu_3 > \tag{A.1}$$

,

Suppose a neutrino is generated at a weak interaction vertex; this neutrino will have definite flavour (ν_e, ν_μ, ν_τ) but will be produced as a linear combination of definite mass states. These mass states then propagate to the detector. If the masses are not the same, the mass states will travel at different speeds and may no longer have the same phases difference as at the source. This means a different relative phase may be measured at the detector, and it is possible that a different flavour will be detected than was produced at the source.

For simplicity in focusing on the meaning of the different parameters, we consider a case where there exits only the ν_e and ν_μ flavours and only the mass states v_1 and v_2. The relationship between these mass states and flavour states as basic rotation matrices:

$$\begin{aligned} \nu_\mu &= \cos(\theta)\nu_1 + \sin(\theta)\nu_2 \\ \nu_e &= -\sin(\theta)\nu_1 + \cos(\theta)\nu_2 \end{aligned} \tag{A.2}$$

or

$$\begin{aligned} v_1 &= \cos(\theta)\nu_\mu - \sin(\theta)\nu_e \\ v_2 &= \sin(\theta)\nu_\mu + \cos(\theta)\nu_e. \end{aligned} \tag{A.3}$$

Here the time dependencies are:

$$\begin{aligned} v_1(t) = v1(0)e^{\frac{-iE_1 t_i}{\hbar}}, \\ v_2(t) = v2(0)e^{\frac{-iE_2 t_i}{\hbar}}. \end{aligned}$$

If we start with our previous example and start with a pure muon neutrino state, then we have:

$$\nu_e(0) = 0, \qquad \nu_\mu(0) = 1, \qquad v_1(0) = \cos(\theta), \qquad v_2(0) = \sin(\theta)$$

The time dependance for this state then:

$$\begin{aligned} v_1(t) = \cos(\theta)e^{\frac{-iE_1 t_i}{\hbar}}, \\ v_2(t) = \sin(\theta)e^{\frac{-iE_2 t_i}{\hbar}} \end{aligned} \tag{A.4}$$

where,

$$\begin{aligned} v_e(t) &= \sin(\theta)v_1(t) - \sin(\theta)v_2(t) \\ &\equiv \sin(\theta)\cos(\theta)(e^{\frac{-iE_1 t_i}{\hbar}} + e^{\frac{-iE_2 t_i}{\hbar}}). \end{aligned} \tag{A.5}$$

The probability that the ν_μ becomes a ν_e is the square of the amplitude, i.e.

$$|\nu_e(t)|^2 = [\sin(\theta)\cos(\theta)]^2(e^{\frac{-iE_1t_i}{\hbar}} + e^{\frac{-iE_2t_i}{\hbar}})(e^{\frac{-iE_1t_i}{\hbar}} + e^{\frac{-iE_2t_i}{\hbar}}) \tag{A.6}$$

$$= \frac{\sin^2 2\theta}{4}(1 - e^{i(E_1-E_2)t/\hbar} - e^{i(E_1-E_2)t/\hbar} + 1) \tag{A.7}$$

$$\tag{A.8}$$

$$= \frac{\sin^2 2\theta}{4}(2 - 2\cos\frac{(E_2-E_1)t}{\hbar}) \tag{A.9}$$

$$= \frac{\sin^2 2\theta}{4}4\sin^2(\frac{(E_2-E_1)t}{\hbar}) \tag{A.10}$$

$$= \frac{\sin^2 2\theta}{4}4\sin^2(\frac{(E_2-E_1)t}{\hbar}) \tag{A.11}$$

$$= \left(\sin 2\theta \sin(\frac{(E_2 - E_1)t}{\hbar})\right)^2 \tag{A.12}$$

$\mathrm{P}(\nu_\mu \to \nu_e) = \left(\sin 2\theta \sin(\frac{(E_2-E_1)t}{\hbar})\right)^2$.

Instead of energy differences, this can be written in terms of neutrino mass difference

as follows; noting our standard relativistic conservation of energy equations, we have

$$E_1^2 = p_1^2c^2 + m_1^2c^4, \qquad and \qquad E_2^2 = p_2^2c^2 + m_2^2c^4. \tag{A.13}$$

Therefore

$$E_{\nu_i} = \sqrt{p^2 + m_i^2} = p + \frac{m_i^2}{2p}, \tag{A.14}$$

where E_ν is the average energy**[1] and p is the same for all mass eigenstate components, i.e. $p_1 \equiv p_2$ and all the masses, m_i are tiny,

$$E_1 - E_2 = \frac{(m_1^2 - m_2^2)}{2p} \approx \frac{\Delta m_{12}^2}{2p}. \tag{A.15}$$

with, $t = L/\beta$, where $\beta \approx 1$, we obtain

$$(E_1 - E_2)t = \frac{\Delta m^2}{2E}L. \tag{A.16}$$

providing the mixing probability as

$$P(\nu_\alpha \to \nu_\beta, t) = | < \nu_\beta | \nu_\alpha(t) > |^2 = 2\sin^2\theta \sin^2\left(\frac{\Delta m^2}{4E}L\right) \tag{A.17}$$

$$= 2\sin^2\theta \sin^2\left(\frac{1.27\Delta m^2[eV]}{2E[GeV]}L[km]\right). \tag{A.18}$$

[1]**Note this is an assumption and not strictly correct, though the obtained oscillation results are the same. More correct is with to utilize a wave packet formulation , but this beyond the scope of this document.

This is an instructive form to work with, and from here we can pick out the following elements to note:

- Δm^2, the mass-squared difference:

  In this example, there are only two flavours, and thus only two mass states. We see here that for neutrino oscillations to occur $\Delta m^2 \neq 0$. This means that at least one of the neutrino masses must be non-zero, explaining that some neutrinos, at minimum, if not all, must have mass. This also means that the masses of the different mass states cannot equal each other, $m_1 \neq m_2$. This is clear also conceptually; *i.e.* if the masses control the relative phase of the mass wave functions, then if they were the same, the relative phase would never change and we would not expect to see oscillations. Instead, we would always see the same linear combination. Note though, from this equation we cannot determine the absolute masses of m_1 and m_2 only the difference in their masses. Further, we also cannot identify which state is more massive and a negative sign in front of the of the mass-squared term would make not affect this equation.

- θ, the mixing angle:

  If the mixing angle $\theta = 0$ then the flavour states are the same as the mass states and oscillations would not be observed. If $\theta = \frac{\pi}{4}$, the case for maximal mixing, then all $\nu_\alpha \rightarrow \nu_\beta$ at some point along the ν propagation. Conceptually this means that this angle tells us how different the mass states are from the flavour states.

- L/E, experimentally set parameter:

  This is the parameter that we can control by deciding where to put the detector (distance, in [km]) from the neutrino source; the terms 'L" or the 'baseline' of the experiment, and E, which is the average neutrino energy of the beam or source. The value of E can be controlled for neutrinos produced in an accelerator facility. For natural sources like the Sun, and the atmospheric neutrinos,

we cannot control E and we may only be sensitive to certain combinations of $(\Delta m^2, \theta)$. Neutrino beams diverge as they propagate, so at some point, the area of the detector area must grow as you move further from the beam. If one wishes to investigate a particular value of Δm^2 for example, then we want to build our detector such as to maximize the value of sin(our variables); i.e. we want $sin^2\left(\frac{1.27\Delta m^2}{2E}L\right) = 1$, so we select L and E to arrange this for the Δm^2 that we wish to investigate.

From measurements of the Z_0 resonance width, there are three (active) neutrinos. We, therefore, require a 3x3 matrix to describe the active neutrino mass mixing. This matrix, called the PMNS matrix after Pontecorvo-Maki-Nakagaya-Sakata, may be written as[14]

$$U = \begin{pmatrix} U_{e1} & U_{e2} & U_{e3} \\ U_{\mu 1} & U_{\mu 2} & U_{\mu 3} \\ U_{\tau 1} & U_{\tau 2} & U_{\tau 3} \end{pmatrix}$$

$$U = \begin{pmatrix} c_{12}c_{13} & s_{12}s_{13} & s_{13}e^{-i\delta} \\ -s_{12}c_{23} - c_{12}s_{23}s_{13}e^{i\delta} & c_{12}c_{23} - s_{12}s_{23}s_{13}e^{i\delta} & s_{23}c_{13} \\ s_{12}s_{23} - c_{12}c_{23}s_{13}e^{i\delta} & -c_{12}s_{23} - s_{12}c_{23}s_{13}e^{i\delta} & c_{23}c_{13} \end{pmatrix}$$

where $s_{ij} \equiv sin(\theta_{ij})$ and $c_{ij} \equiv cos(\theta_{ij})$. Here θ_{ij} is again the mixing angle. The parameter δ is a phase, which was not present in the two flavour case, selected for charge-parity violation in the three flavour case. Note that the sign of the mass difference changes the oscillation probably if δ has certain values.

A common parametrization of the PMNS matrix is to separate the 'atmospheric,' 'accelerator/reactor,' and 'solar' parameters respectively

$$U = \begin{pmatrix} 1 & 0 & 0 \\ 0 & c_{23} & s_{23} \\ 0 & -s_{23} & c_{23} \end{pmatrix} \begin{pmatrix} c_{13} & 0 & s_{13}e^{-i\delta} \\ 0 & 1 & 0 \\ -s_{13}e^{-i\delta} & 0 & c_{13} \end{pmatrix} \begin{pmatrix} c_{12} & s_{12} & 0 \\ -s_{12} & c_{12} & 0 \\ 0 & 0 & 1 \end{pmatrix}$$

The current global best fit values for the neutrino oscillation parameters are shown in table 10.1:

Parameter	Best-fit value	Error	Unit
θ_{12}	33.6	$^{+1.1}_{-1.0}$	$^\circ$
θ_{13}	8.93	$^{+0.46}_{-0.48}$	$^\circ$
θ_{23}	38.4	$^{+1.4}_{-1.2}$	$^\circ$
$\sin^2(\theta_{12})$	3.07	± 0.18	10^{-1}
$\sin^2(\theta_{13})$	2.41	± 0.25	10^{-2}
$\sin^2(\theta_{23})$	3.86	$^{+0.24}_{-0.21}$	10^{-1}
$\sin^2(2\theta_{12})$	8.51	$^{+0.26}_{-0.29}$	10^{-1}
$\sin^2(2\theta_{13})$	9.41	$^{+0.95}_{-0.96}$	10^{-2}
$\sin^2(2\theta_{23})$	9.48	± 0.20	10^{-1}
Δm^2_{21}	+ 7.54	$^{+0.26}_{-0.22}$	$10^{-5}\,\mathrm{eV}^2$
Δm^2_{32}	+ 2.39	$^{+0.06}_{-0.10}$	$10^{-3}\,\mathrm{eV}^2$
δ	1.08	$^{+0.28}_{-0.31}$	π

Figure A.2: Example global best fit values for the neutrino oscillation parameters for normal mass ordering [79].

In summary lepton families propagate in mass eigenstates, oscillate, and are measured as flavour states via weak force interactions. If neutrinos have mass (which they do) then they will oscillate, *i.e.* change their flavour (neutrino type) from one to another. It is worth noting that the smaller the masses, the longer the oscillation length becomes. Note, oscillation length is defined for L/E from one peak to the next, Figure A.3. Where the maximum probability of converting one type of neutrino to another is equal to $\sin^2 2\theta$. Experimentally, this quantity is shown to be near maximal mixing, for the 2-3 states, making ν_μ disappearance/ν_τ appearance a dramatic effect. The frequency of the oscillation is controlled by the square of the difference the mass

of ν_α and ν_β, i.e Δm^2.

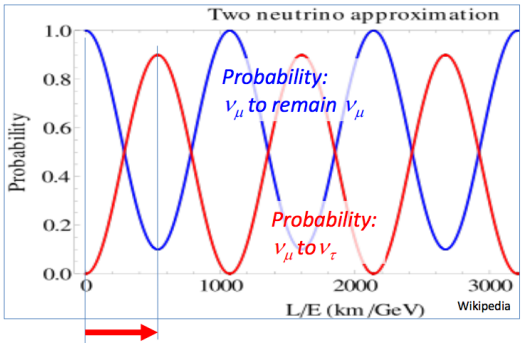

Figure A.3: Showing the neutrino oscillation probabilities for the two neutrino approximation (here $\nu_\mu and \nu_\tau$), for a given L/E from the neutrino source. The blue line shows the probability that the original neutrino, ν_μ will retain its identity, $P(\nu_\mu \rightarrow \nu_\mu)$; the red line is the probability it will be converted to ν_τ, $P(\nu_\mu \rightarrow \nu_\tau)$. Note IceCube is able to measure L/E from ∼65 (far left) to ∼1300. Figure taken from wikipedia

A.2 Aside on Matter Oscillations

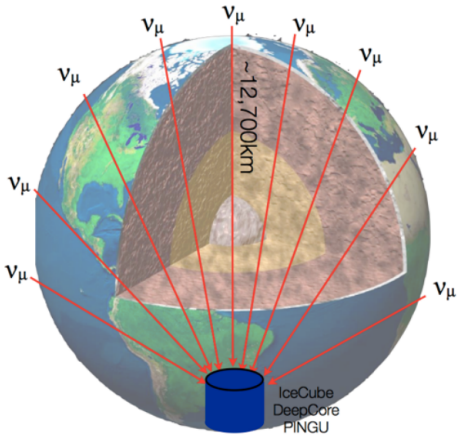

Figure A.4: Atmospheric neutrinos traversing the earth to reach a ground-based observatory.

The above calculation describes oscillations in a vacuum. In reality neutrinos may have propagated through the matter of the Earth to reach detectors. When neutrinos propagate through matter, there is a certain probability that electron neutrinos will

scatter off electrons present in the material they are traversing. If we call the interaction potential of a given propagating neutrino 'V', then a neutrino propagating through matter can be considered to have an 'effective mass,' and the total energy of the neutrino will now not only be E, the energy of the neutrino in a vacuum, but E + V. As different neutrinos have different potentials in matter, phase differences may develop due to this additional potential; that is, we may see additional neutrino oscillations purely due to this matter effect. If these oscillations from matter resonate with the vacuums oscillations, we may see an enhancement of the oscillation effects. This enhancement effect is called the MSW effect. It has a dramatic effect on solar neutrinos (neutrinos produced in and then propagating out of the sun), and also affect atmospheric neutrinos in ground-based detectors, to a much lesser extent A.5.

A.3 Oscillation of Atmospheric Neutrinos

Atmospheric neutrinos are produced in fairly well-known quantities and flavours. An example of the oscillation pattern is shown in figure A.5. For the majority of atmospheric neutrinos measured with IceCube, they must travel at least 10 km and at most 12600 km (the diameter of the Earth), Figure A.4.

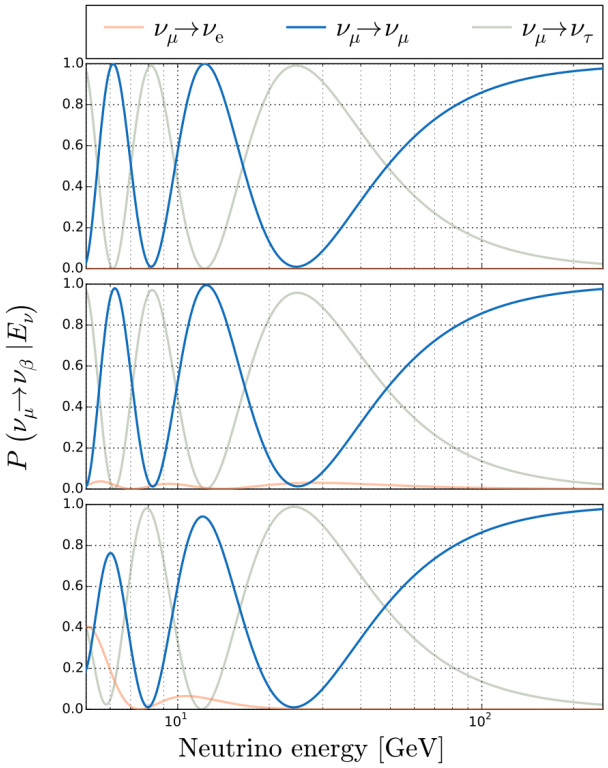

Figure A.5: Three panel figure showing up-going atmospheric neutrinos which have traversing the earth to reach the IceCube Observatory [31]. The (top panel) is shown in the two-neutrino approximation, in a vacuum. The (middle panel) shows three neutrino flavour oscillations and the (bottom panel) shows three neutrino flavour oscillations in matter. The oscillation baseline used is 12,600 km [31].

Appendix B

Event Selection Variable Related Definitions

This section describes the technical details and definitions of the selection variables which are discussed more generally in the previous Appendix.

B.1 Interaction Vertex

In IceCube coordinates the origin or centre of the detector is defined as $(x, y, z) = (0, 0, 0)$ on the centre of String 36, in the middle of the detector, which is approximately 1950 m below the surface. In the vertical direction, z, DeepCore DOMs is located between -500 m and -150 m, and the dust layer is between -210 and -135 m.

Radial position ρ, is defined as:

$$\rho = \sqrt{(x - x_{36})^2 + (y - y_{36})^2}, \tag{B.1}$$

and depth position z of the interaction vertex are often used.

Appendix C

Data Sample Selection Details by Level

C.1 Selection Criteria: Levels 1- 6

The first levels, (L1 and L2) are based on trigger conditions and (L3) depends primarily on veto cuts. These are common for a given energy range in IceCube and the independent selection criteria of a given unique sample starts at level 4.

C.2 Levels 1-2 (Common Levels)

This section discusses the basic event filtering at the early stages of selection processes. Pulling the above knowledge together, we can now define the standard and unique levels in IceCube analyses. Levels 1 and 2 are standard to all and are based on online triggering (level 1) and filtering (level 2). As outlined, both these rely on charges recorded by the PMTs in all DOMs. In IceCube, it is assumed that each photon hitting a DOM releases one photoelectron. The calibration and characteristics of a PMT are described in [36]. In IceCube a photoelectron (PE) is the unit of

charge, where 1 PE is defined as the charge recorded by a DOM when a single photon hits the DOM and exceeds a 0.25 PE threshold, i.e. the 'hit' defined above.

When several nearby DOMs are hit, a local coincidence (LC) occurs, indicating a possible physics event.

Online trigger (Level 1) and online filter (Level 2) take place on site at the South Pole [42] and are discussed in the main body of this thesis.

C.3 Level 3 (Mostly Common Level)

As preciously discussed, Level 3 selection aims to removes events that are triggered by atmospheric muons and by noise. Algorithms at Level 3 rely on hit information and make use of the DeepCore volume and surrounding strings.

NoiseEngine/ MicroHits & MicroCharge

Two algorithms are used to identify events triggered by random detector noise. First, the *NoiseEngine* [80] algorithm looks for indications of directionality in the hits. First a hit cleaning is preformed via removal of isolated hits from the event and then a time window is found that maximizes the number of hits categorised as 'clean'. Then clean hits are compared to all other hits and to see if the hit pair satisfies a space-time window suggestive of causal connection. These are then projected onto a binned sphere and if three or more pairs are categorized into the same bin, then hits are deemed likely to be casually related and the event is kept, as this scenario is likely not to be triggered by random noise. The second algorithm *MicroHits & MicroCharge* uses both hit timing/position information and charge information. Again cleaned hits are used as well as a dynamic time window. Instead of binning on a sphere, the criteria is that no more than two cleaned hits can have a charge of 2 PE or more, otherwise the event is rejected from the sample.

VertexGuessZ (vertical position first guess) and DeepCore Fiducial volume PE (charge in DeepCore fid. vol.)

Two selection criteria are applied to quickly identify possible physics events (neutrinos) that take place inside the DeepCore fiducial volume. The first requires that the total amount of charges inside the DeepCore fiducial volume be greater than zero. The second requires that the first cleaned hit has a z position below -120 m. Both of these selection criteria must be passed for a possible physics event (neutrino) to be considered.

High charge events

To find atmospheric muon events that may still be present in the physics events sample, charge variables are considered. An atmospheric muon tends to have a higher value of hits above 200m (in detector coordinates) than a neutrino signal event. This variable is called *NAbove200*. A possible physics event is rejected from the sample when *NAbove200* is greater than 12 PE. The *Center of Gravity* (CoG) algorithm which is used to identifies casually connected hits in the veto region earlier in the analysis chain. At this stage, the charges from these hits are summed and if the total charge from hits in the veto region greater than or equals 7 PE, the event is rejected.

Fiducial volume vetos

The last two common Level 3 selection criteria are charge-related and fiducial volume related. The first is the ratio of total charge outside the fiducial region to inside the fiducial region and events with this ratio greater than 1.5 are rejected from the sample. A second charge ratio cut *C2QR6* which is more complex is also used here. It is defined in [31].

The vent rate from data is dropped by a factor of 20 at this level. (From $\sim$ 20 Hz to

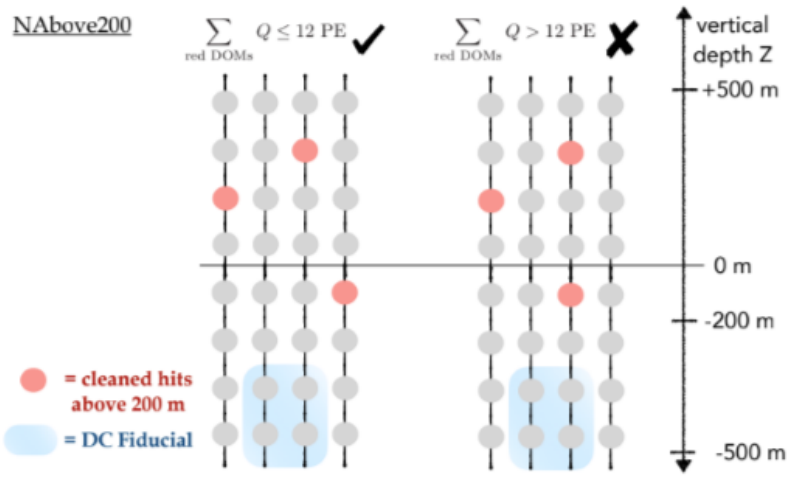

Figure C.1: Showing charge variable NAbove200 [81].

~ 1 Hz).

The next stages of selection in DeepCore are typically unique to a given data sample. For this work, the sample was extended in energy from 56 GeV in reconstructed energy, to 180 GeV in reconstructed energy. Changes to the standard sample [3] begin at level 5. The focus of the next chapter is on the checks made in order to justify this extension and the changes implemented in order to do so.

C.4 Level 4

This section focuses on the event selection method. To overview, this event selection (internally called the "DRAGON" sample), uses a set of straight cuts and a boosted decision trees to improve the purity of neutrino events (physics events for this sample).

Further, following the BDT, events flagged by the corridor cut are rejected.

Trigger cuts: charge/hit related

In low energy events one suffers from a lack of information. To determine if there is sufficient information detected in an event for current reconstruction algorithms, *NChannel* (number of hits in an event; events must have at least 8 cleaned hits to avoid being ejected from the sample) and *RTFiducialQ* (charge-related variable which searches for clusters of cleaned hits in the DeepCore fiducial region that are causally connected; events with a minimum of one cluster with at least 7 PE are not rejected).

Trigger cuts: event size related

These cuts are based on our *Center of Gravity* (CoG) algorithm. The first cut is based on the space-time interval Δs^2. Here Δs^2 is used to differentiate between events caused by random noise from neutrino events. Events where Δs^2 is between -$(400\,\mathrm{m})^2$ and $0\,\mathrm{m}^2$ remain in the sample. All others are rejected. The next two cuts relate to the physical size of the potential physics event. This is determined by the charge-weighted spread of vertex z position (σ_z) as well as the photon arrival time (σ_t). Events with $\sigma_t \leq 1{,}000\,\mathrm{ns}$ and $7\,\mathrm{m} \leq \sigma_z \leq 100\,\mathrm{m}$ are kept and all other events are rejected.

Veto

These cuts aim to remove further atmospheric muons from the sample. They are done via two veto requirements. The first variable counts veto charges using the CoG algorithm and is very similar to the total veto charge requirement at Level 3 but is instead applied to the veto region outside the DeepCore fiducial volume. In this larger veto volume events with a total veto charge greater than 5 PE are rejected. The second veto charge requirement defines a veto volume by the estimated point of interaction (integration vertex), and us called *VICH*. *VICH* looks for causally-related

hits in a dynamic veto region which is calculated event-by-event. Events with greater than or equal to 7 PE are rejected.

Containment

A containment is also required of the retained sample events. This is made up of four containment conditions demand that the point of interaction in an event is inside the DeepCore fiducial volume. Only events with ρ_{HLC} less than 150 m and z_{HLC} position between -475 m and -200 m remain in the sample. As well, the ρ_{Q1} and z_{Q1} vertex positions from the first quartile (Q1) in the CoG algorithm are calculated. Only events with ρ_{Q1} less than 150 m and z_{Q1} position between -475 m and -150 m are not rejected. See [31] for details and development of these cuts.

C.5 Sample - Level 5

At Level 5, a boosted decision tree (BDT) with eleven variables is trained to continue reducing the atmospheric muon background (see figure C.2). These variables are of three main types: event reconstruction, charge and event CoG (event vertex) variables. Each is explained and detailed in [31]. A quick overview is given here for ease of reference.

Event reconstruction BDT training variables

The three event reconstruction are obtained from IceCube's two fast reconstruction algorithms.They are the reconstructed particle speed (via the *iLineFit* algorithm [36]) and zenith angle (from *SPEFit11* [36] and *iLineFit*)..

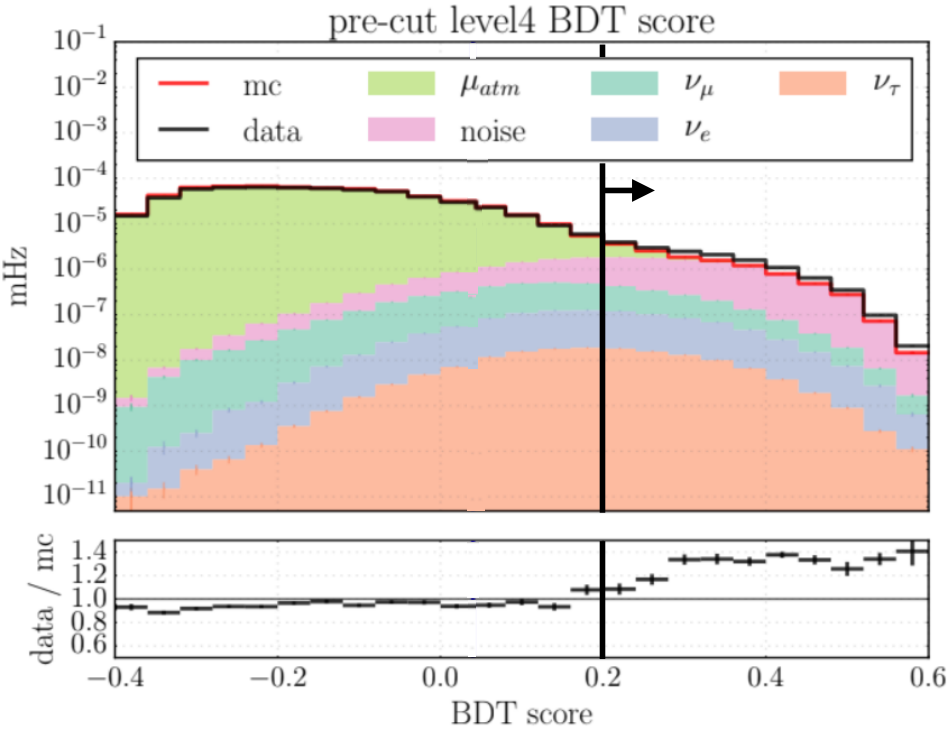

Figure C.2: (TOP) The BDT score distribution. A cut is placed at 0.2 BDT score. The shaded colours show (stacked) histogram from each event type and the black line shows the distribution of data events. The vertical line is the cut value of 0.2, events below which are rejected [3]. (BOTTOM) The black error bars show the statistical fluctuation from data. The script for plot adopted from [81].

PMT Hit and charge related BDT training variables

Four BDT variables are related to charge and hit information. They include the charge ratios and the number of hit DOMs in the cleaned hit series as well as the total charge from the event $qTOT$. As noted previously, atmospheric muons generally deposit more charge than a neutrino. As such, regions of high-charge in the total charge distribution can be used to aid in tagging atmospheric muons (which are background in this sample).

CoG related BDT training variables

These four variables use the separation in space of the first and last collected charges in a considered event's hits. Three of the variables are reused from level 4.

Fig. C.2 shows the BDT score distribution, and a cut is applied to accept events with a score above 0.2. Compared to Level 4, 99.9% of the atmospheric muon background is removed, whereas 58% of all neutrinos are kept after the BDT score cut is placed.

C.6 Sample - Level 6

After completing Level 5 the detailed event reconstruction takes place which uses the MULTINEST algrithm. After this reconstruction we begin Level 6 and several final selection criteria are added to improve neutrino purity of the sample.

Second set of Containment Cuts

Based on the newly found starting and stopping positions of the carefully reconstructed event, a second set of containment criteria is required. These are containment regions are illustrated by the red lines in figure C.3. The starting containment aids in rejecting atmospheric muons travelling into the analysis volume through the

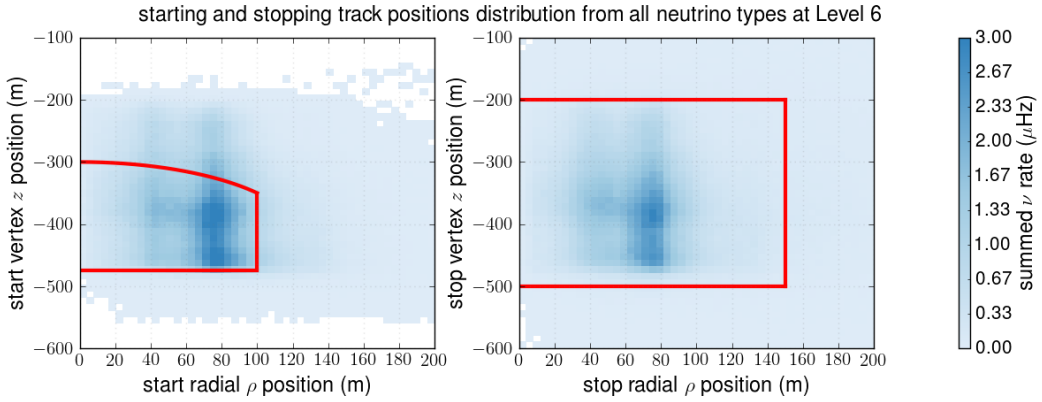

Figure C.3: Showing the 2D distributions of events in IceCube Coordinates (see previous Appendix). Radial ρ and depth z positions of reconstructed track are found in the final detailed reconstruction. (LEFT) shows the starting containment cut and (RIGHT) the stopping containment (which is not required in this analysis). The colour axis is the total rate from all neutrino flavours. The red lines outline the containment cuts, inside which events are kept [53].

dust layer. The stopping radial ρ_{stop} and depth z_{stop} positions are required to be within $\rho_{\text{stop}} \leq 150\,\text{m}$ and -500 m $\leq$ z_{stop} $\leq$ -200 m . In addition to expanding the energy range on the data selection, the L6 stopping containment cut on the sample was removed in order to retain more events in the above ∼56 GeV range.

Approximately 2000 events were gained in the higher energy bins of the sample by removing the stopping containment cut shown in figure C.3 right. The starting containment (left figure C.3) remains in place. Due to these changes the following checks on the sample are preformed and shown in following chapters.

Direct Hits Cut (SANTA [51])

A final cut is applied to increase the purity of cc ν_μ events. This cut is baed on the number of 'direct hits' in an event; where direct hits are hits from minimal scattered photons. These are determined with the SANTA algorithm [51]. Only events with at least three direct hits are kept in the sample

Appendix D

Global Flux Knowledge and Discussion of Available Models.

D.1 Current Flux Knowledge - Overview

For the neutrinos considered in this Analysis, typical cosmic ray energies are of the order of 100 GeV - 1 TeV. At these energies the hadronic and primary flux uncertainties in the absolute neutrino flux increases [12, 82]. There is less experimental data at these energies compared to that for GeV scale neutrinos where the availability of secondary particle production data from accelerators, and direct cosmic ray flux measurements, result in good model predictions [12]. Part of the increase in the uncertainty arises for kaons becoming more relevant as the parent meson above approximately 70 GeV neutrino energy. Where the absence of fixed-target kaon measurements on light nuclear targets drives the extrapolation errors in the hadronic interaction models [4]. An uncertainty estimation is assigned to each region of the energy-momentum fraction phase-space based on the evaluation of globally available fixed-target data. Due to the steep primary (CR) spectrum, the relevant phase-space for inclusive lepton production is $x_{\mathrm{F}} \sim 0.2$ [83], where x_{F} is Feynman-x (or longi-

tudinal momentum fraction) [84]. There are very few measurements of $x_{\mathrm{F}} \sim 0.2$ (parallel momentum having a large fraction 0.2 of the beam momentum) as this is region extremely close to the beam (see fig D.1),

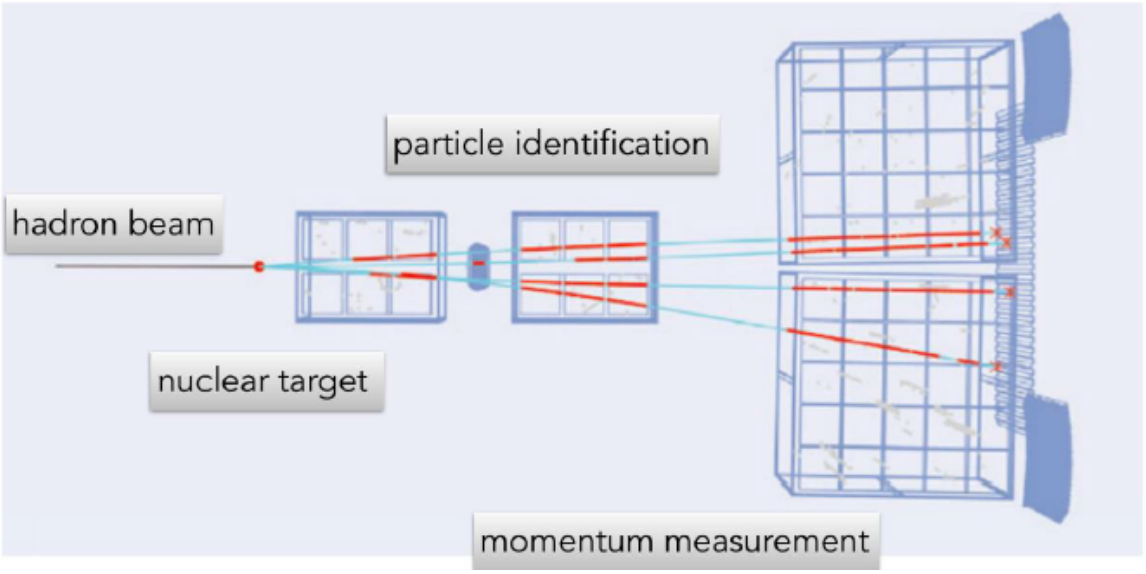

Figure D.1: This graphic shows a particle accelerator beam and detectors to measure hadronic physics. The scattering angle θ of the resultant particles is defined by P_z (forward momentum) and P_T (transverse momentum), where P_z is $\sim$ TeV -PeV and P_T is typically a few GeV and $\theta = arctan\frac{P_T}{P_z}$. Most atmospheric leptons come from forward phase-space, where there is a gap in detector coverage at accelerators (along the beam line).

Correspondingly the lack of beam data in the models leads to large model uncertainties in their region of analysis.

To summarize, current estimates have $\geq$ 30% uncertainty in kaon (K) production and $\geq$ 15% uncertainty in pion (π) production in the projectile fragmentation region, leading to uncertainty in hadronic models in the region that is relevant for the mesons produced in the atmosphere [12]. A K/π ratio measurement could be used to improve and constrain hadronic interaction models in $x_{\mathrm{F}} \sim 0.2$ and would represent a significant improvement over current measurements.

For TeV scale neutrinos, cosmic ray observations in the relevant range become indirect, and errors from the primary flux model contribute significantly to the total

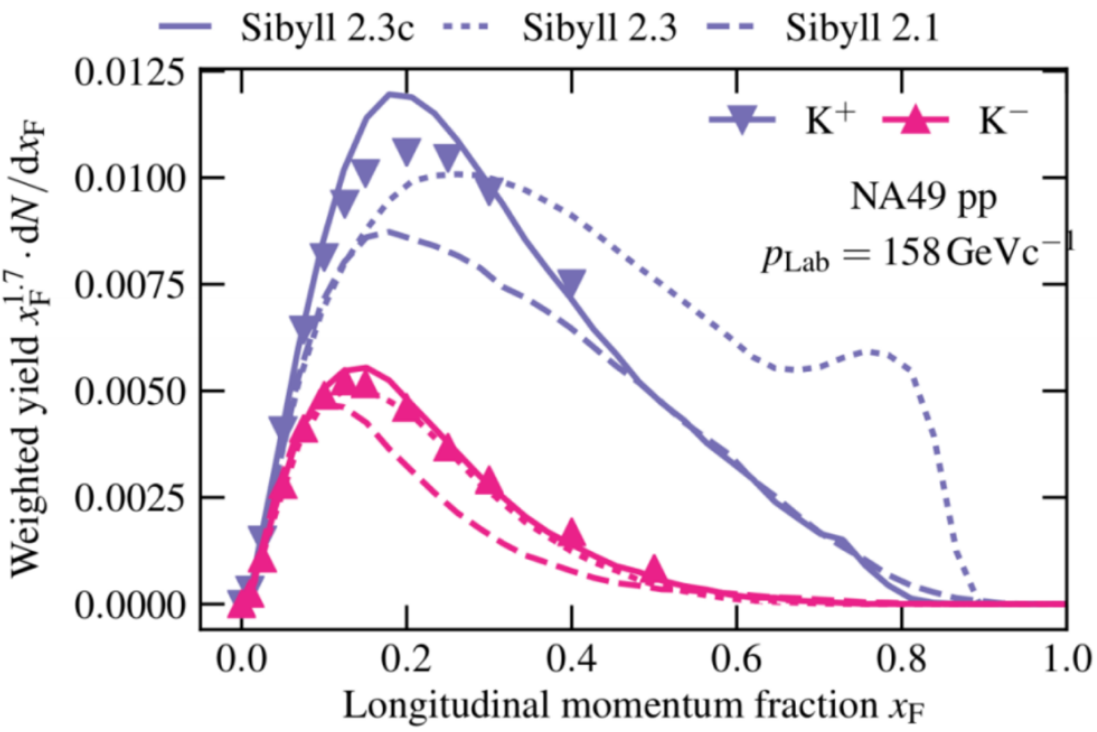

Figure D.2: This plot taken from A.Fedynich VietNus2017 shows NA49 p-p data plotted over the hadronic integration models from the Sibyll series: Sibyll 2.1, 2.3 and 2.3c. It highlights how a lack of kaon data from nuclear targets about 100 GeV create an issue in hadronic interaction modelling. On the x-axis is X_f, which is the longitudinal momentum fractionated on the y-axis is the particle yield in $\frac{dN}{dx_f}$. Note that K_L^o and $K^{\pm}$ become the dominant source of ν_es above $\sim$ 100 GeV.

uncertainty.

D.2 Current Flux Knowledge - Inputs

Due to the advancement of neutrino detectors, atmospheric neutrino measurements are now capable of providing precision input to cosmic ray and hadronic interaction models [4]. Atmospheric neutrino flux calculations [85, 21] require as minimum input: the cosmic ray spectrum model (that provides the energy spectrum of the incident particles that create the particle shower), the hadronic interaction model (that governs the production of particles as well as their interactions), and the atmospheric

density profile model (which provides the atmospheric content, thickness and particle density). The cosmic ray spectrum model and hadronic interaction model represent the largest uncertainties in these predictions [12]; their precision study remains a challenge for the field.

D.2.1 Available Cosmic Ray Models

The choice of cosmic ray interaction model (ie. the expected particle type proton or heavier ion and flux impinging on the atmosphere) impacts the spectrum of the primaries and therefore the shape of the energy unfolding of the atmospheric neutrino energy spectrum, as well as the atmospheric neutrino flux. Cosmic ray models need to cover 12 orders of magnitude in energy (from 10^9 to 10^{20}). Direct measurements

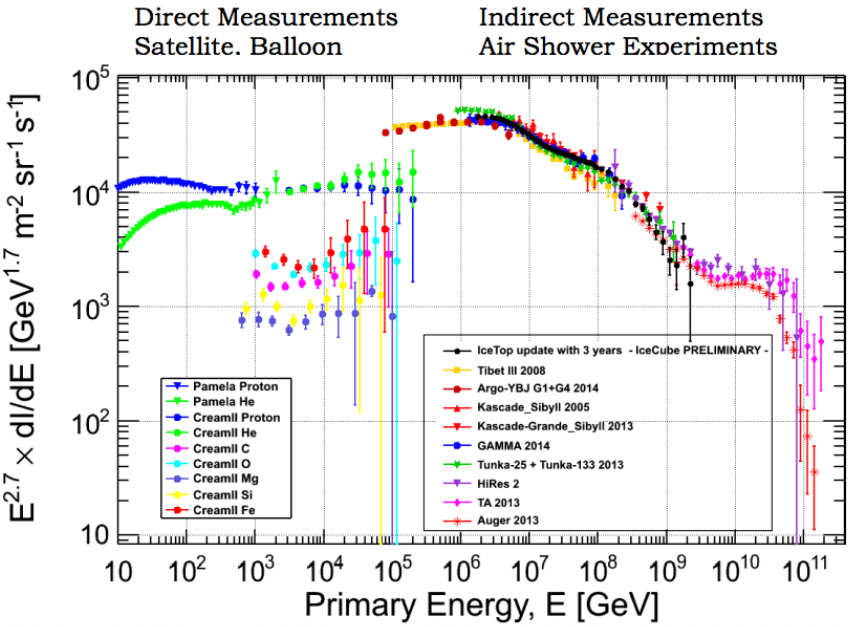

Figure D.3: Cosmic ray energy spectrum. PAMELA / ATIC / CREAM show rigidity-dependent spectral breaks and spectrum hardening (steepening) after these breaks. IceTop shows that the spectrum does not follow a simple power law above the knee up to 1 EeV and shows spectral hardening at ∼18 Pev and ∼130 PeV [17].

are ideal but can only be made over positions of this energy range via satellite- and

balloon-based experiments. Neutrino observatories and air shower experiments, like IceCube and Auger, can respectively, provide indirect measurements in a compensatory range of energies. It is expected that several source populations are needed to

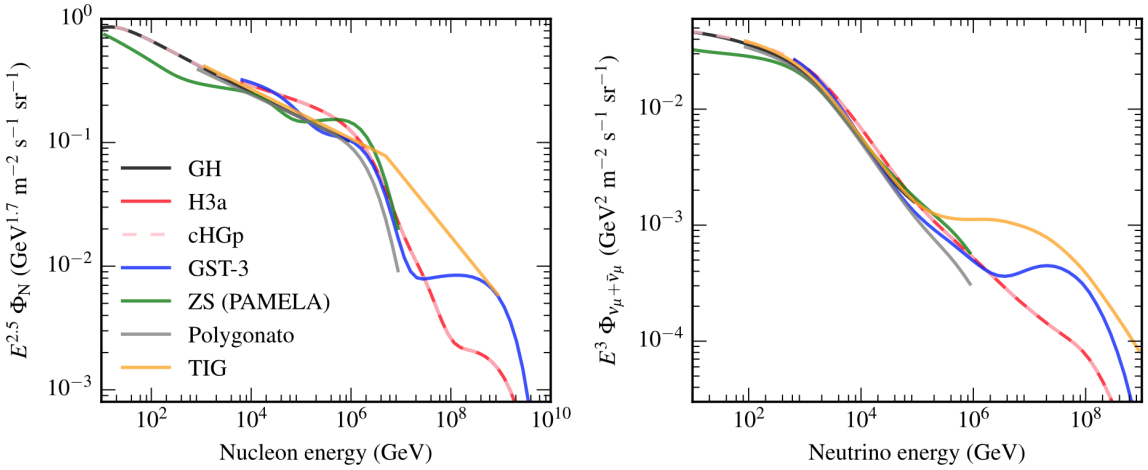

Figure D.4: Showing cosmic ray nucleon energy spectrum for available MCEq cosmic ray spectrum models and partner neutrino energy spectrum [4]. The (left) shows the incoming proton energy and the (right) shows the resultant neutrino energies.

explain the observed cosmic ray spectrum [17]. One method is to fit the elemental spectrum with theoretical assumptions resulting in a smooth curve; another is a data-driven model, e.g. Global Spline Fit (GSF) [58], that parametrizes measurements of the cosmic ray flux and its composition (from 10^1 to 10^{11} GeV).

D.2.2 Available Hadronic Interaction Models

Differences between hadronic interaction models are the primary source of uncertainty in the prediction of extensive air showers (our signal in this analysis). The dependance of uncertainties on the hadronic models r the cosmic ray flux is linear *i.e.* a 10% error in the cosmic ray flux results in a similar shift of the neutrino fluxes [12] Here we split the hadronic interaction models into two categories: those updated using the first LHC data; and those updated to take into account LHC data at 7 TeV. These models have recently become available and were implemented as part of MCEq [4]providing improved descriptions of particle production; particularly

of charmed particles [86]. Four high energy models were updated to take into account LHC 7 TeV data. This are: EPOS-LHC [61] (updated from EPOS 1.99 [87]), QGSJETII-04 [62] (updated from QGSJETII-03 [88]), Sibyll 2.3c [63] (updated from Sibyll 2.1 [64]), and DPMJET-III.17-1 [22] [60] (updated from DPMJET2.55 [23]). Beyond taking the LHC 7 TeV data into account, the other changes to these models include an update of parameters in order to reproduce the TOTEM cross-sections [89].

These hadronic interaction models are all parton based models associated with the Gribov-Regge multiple scattering approach [86] This type of simple parton model sees scattering as an exchange of 'parton ladders' between a projectile and target. The four main differences in approach of the models mentioned above, are:

EPOS-LHC

These modes are derived from minimum bias Monte Carlo hadronic generators. The goal is to describe soft particle production for any system and energy (*i.e.* rare particles, and all possible data). This model takes into account: high-density effects leading to collective behaviour in heavy ion collisions; Cronin transverse momentum broadening; parton saturation; and screening. In doing so, it aims to be able to describe all types of heavy ion data and nuclear effects. It is used in both heavy interactions and cosmic ray air shower simulations.

DPMJET - III

This is a minimum bias Monte Carlo hadronic generator. It is suited to studying particle jet projection rather than soft particle production [86] since it does not including any final stage interactions due to collective hadronization (i.e. high-density interactions, effecting charm interactions). It is a full extension of the parton model to nuclear interactions and is used in both heavy interactions and cosmic ray air shower simulations.

QGSJET

This is a minimum bias nuclear interaction model optimized for air shower simulations. It has a minimum set of parameter choices to reduce the uncertainty caused by

extrapolation to high energies. As a result, this model has a less detailed description of the final stage of hadronic interactions (no final state effects, and no rare particle production) [86].

SIBYLL

This model is a minimum bias Monte-Carlo hadronic interaction model. It is also optimized for air shower simulations, but has a different approach compared to the QGSJET models. For more than 15 years, Sibyll 2.1 has been a standard model for air shower simulation [64] [86] used extensively in CORSIKA [50] in IceCube. Sibyll advances are motivated by data of the LHC and fixed-target experiments, and a better understanding of the phenomenology of hadronic interactions, to develop an improved version of this model [86].

D.2.3 Available Atmospheric Density Models

Atmospheric density models contain details of the atmosphere (density, content, etc.) for various geographic locations. Averaged models (US Std) also exist. For a detector at the South Pole, there is an expected seasonal difference in the slant depth at a given angle (see Figure D.5). To account for this, flux calculations of mass density are performed for each month and the results are averaged for each season.

Of the sets of atmospheric density models available at the time, NRLMSISE-00 [90] is considered to state of the art [5], being the favoured model of Super-Kamiokande. It contains seasonal variations and an accurate global density map with specific consideration of the South Pole location. NRLMSISE-00 is also the atmospheric density model used in the HKKM2014 (HONDA) model [5]; one of the most robust atmospheric neutrino flux models available to date.

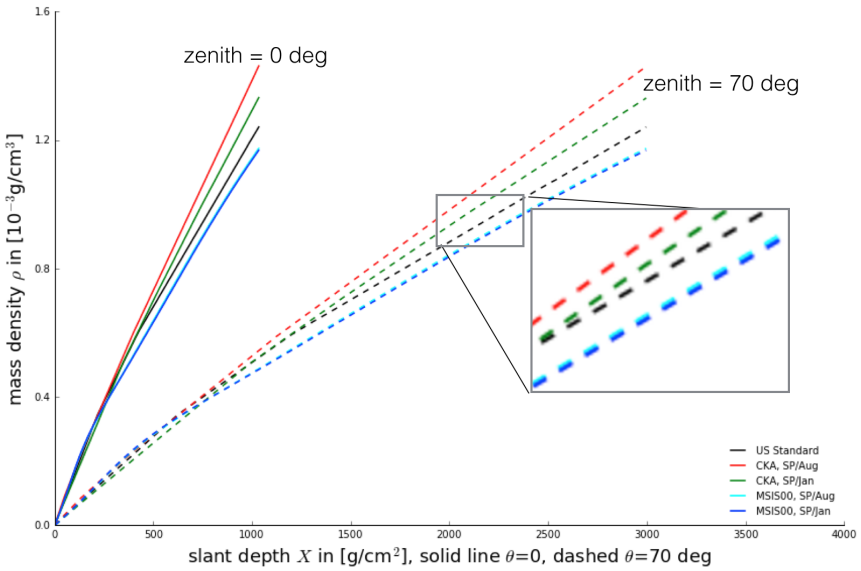

Figure D.5: Showing the expected mass density as a function of the slant depth for respect to the IceCube detector location. Plot created with MCEq.

D.2.4 HKKM2014 (Honda) models

In addition to the individual model components discussed, complete atmospheric neutrino flux models exist, predicting fluxes at a given location on Earth. These final product models typically utilize a given hadronic interaction model, cosmic ray flux model and atmospheric density model themselves. The result is to provide the user with the atmospheric neutrino fluxes at the Earth's surface, typically parameterized in cos(zenith) and energy. The atmosphere models by Honda et al. (HKKM2004 [91], HKKM2011 [74], HKKM2014 [5]), are used by many neutrino experiments, due to their precision from close development with measurements at Kamiokande and Super-Kamiokande.

These models are also calibrated to the muon charge ratio data from balloon experiments, improving the model accuracy [5]. A challenge of such models is that one cannot, for example, explore the impact of the hadronic interaction models on the final flux and experimental parameters of interest. As a result, is difficult to discern the uncertainties of a given model component choice, for example.

D.2.5 Note on K/π Ratio Definition

The predicted K/π depends on how we define the neutrino parent particle source. In Figure D.6 we show an example of this for neutrinos at IceCube, calculated using [4].

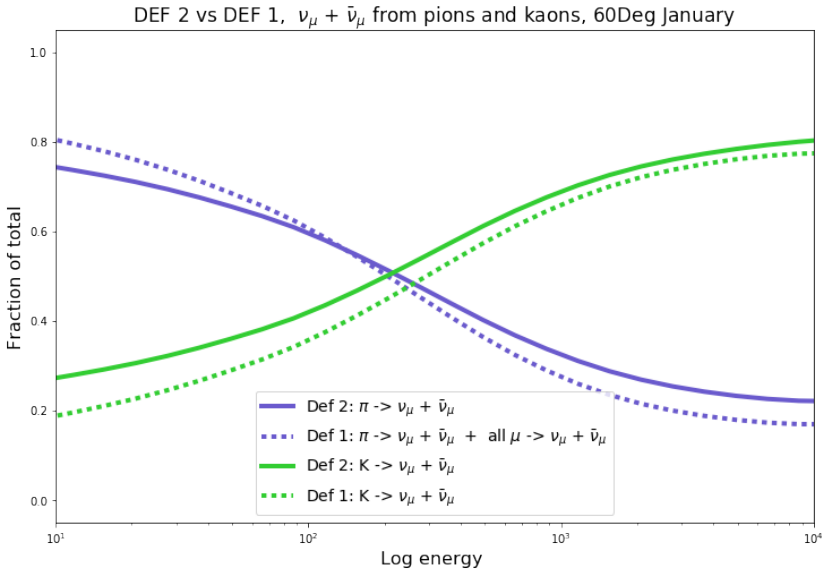

Figure D.6: Showing fractional contribution of intermediate particles to the flux of atmospheric neutrinos, zenith angle 60°using primary (cosmic ray) spectrum is Gaisser-Honda [21] and the interaction model is DPMJET-III-2017.1 [22]. $K \rightarrow \nu_\mu + \bar{\nu}_\mu$ and $\pi \rightarrow \nu_\mu + \bar{\nu}_\mu$ is shown as 'def2' when accounting from first mesons produced in the cosmic ray shower, and 'def1' when neutrino parent is defined as from the meson that most recently created the neutrino.

Appendix E

Predicted Flux Table Generation and Re-weighting

This appendix details the procedure outlined above in step-by-step detail for the curious and for the use of anyone performing a follow-up analysis.

E.1 MCEq Table Generation for the Predicted Neutrino Flux in Direction and Energy

Utilizing a simple wrapper written by the author for MCEq, (that takes as input a zenith angle, a cosmic ray flux model, a hadronic interaction model and an atmospheric density model) we create tables of the expected particle fluxes for a set of predefined energies by solving the matrix cascade equations. We then spline the resulting tables, see in figure E.1.

The advantage of using MCEq is the ability to choose combinations of preferred models. For this analysis we choose to make three separate tables for ν_μ flux: $K \to \nu_\mu$ *i.e.* the total expected atmospheric neutrino flux decaying from kaons, $\pi \to \nu_\mu$, *i.e.*

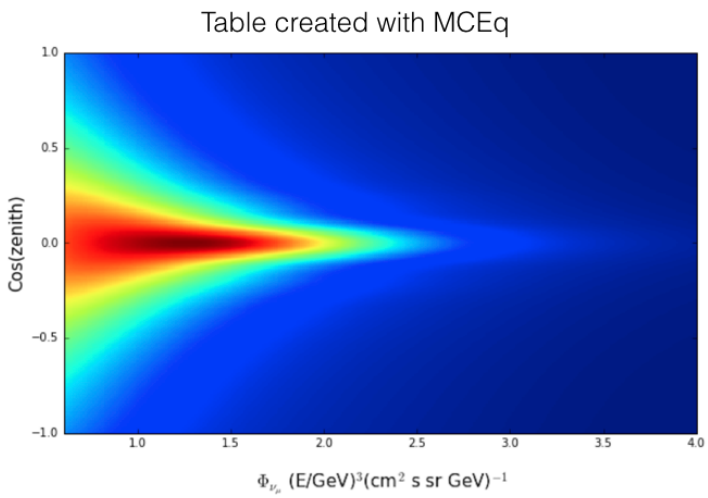

Figure E.1: Spline of an example MCEq table of total ν_μ flux created with DPMJET-III and H3a, generated by the author.

the total expected atmospheric neutrino flux decaying from pions, and ν_μ total.

CORSIKA users currently have no choice but to measure the K/π ratio in terms of the last produced meson. As part of this thesis work, it is now possible to break the atmospheric neutrino flux into prediction tables based on the first produced meson. This is a more meaningful separation as this is what we expect to be most sensitive to in the IceCube detector. Modelling in this way allows us to more directly probe the hadronic interaction model used in the analysis. In the next pass of this analysis it is hoped that the K/π ratio will tested for all the model tables that have subsequently been generated here.

E.2 Re-weighting the Predicted Flux.

The predicted energy spectra are re-weighted in this analysis so that the total flux in a given energy segment is E^3. In doing so, the event weighting scheme that gives a largely flat spectrum in E^3, but preserves the zenith angle distribution shape and thereby the K/π for a given hadronic model (see Figure E.3).

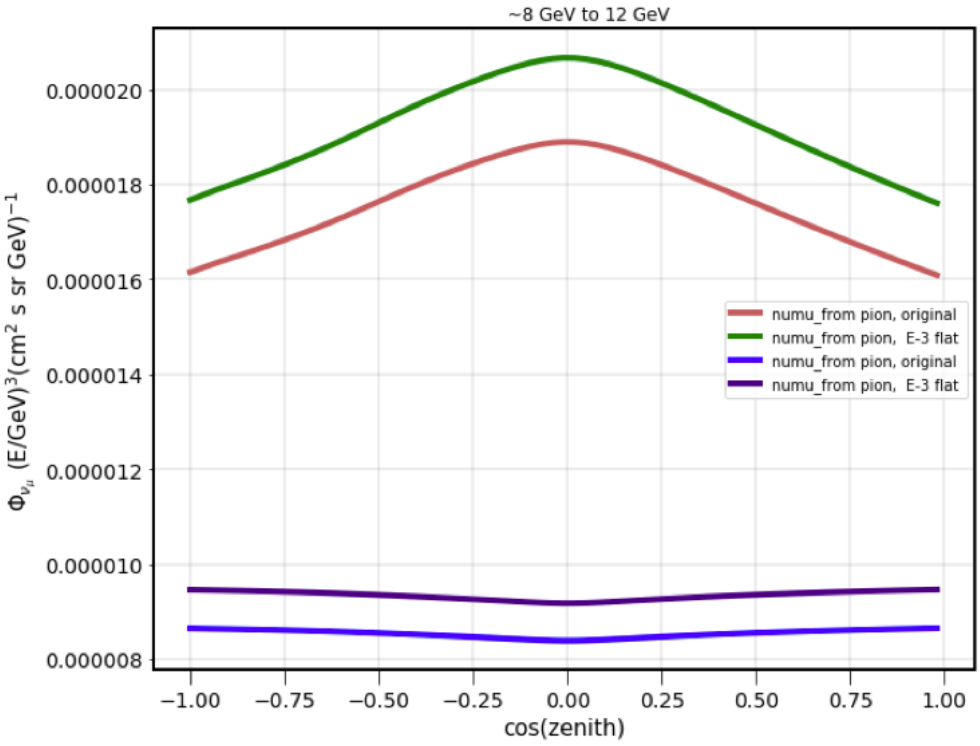

Figure E.2: Zenith projections of an energy segment based on MCEq tables before and after energy spectrum reweighing. Note the shape of the zenith distribution is preserved. This plot shows a low energy range example segment.

We may then make slices in true energy in this projection to make segments in energy that can be used in the spectral fit. With the set of weights nearly flat in E^3, the energy spectrum becomes quasi-independent of the model. Here the ν_μ from *pi* and ν_μ from K need to be separate tables so that we can scale them up and down relative to one another and so fit for the K/π ratio. Note that we will respect $\nu/\bar{\nu}$ ratio as predicted by a given MCEq model; *i.e.*, we allow the previously mentioned scaling factor to float but we do not change the shapes of the predicted component distributions.

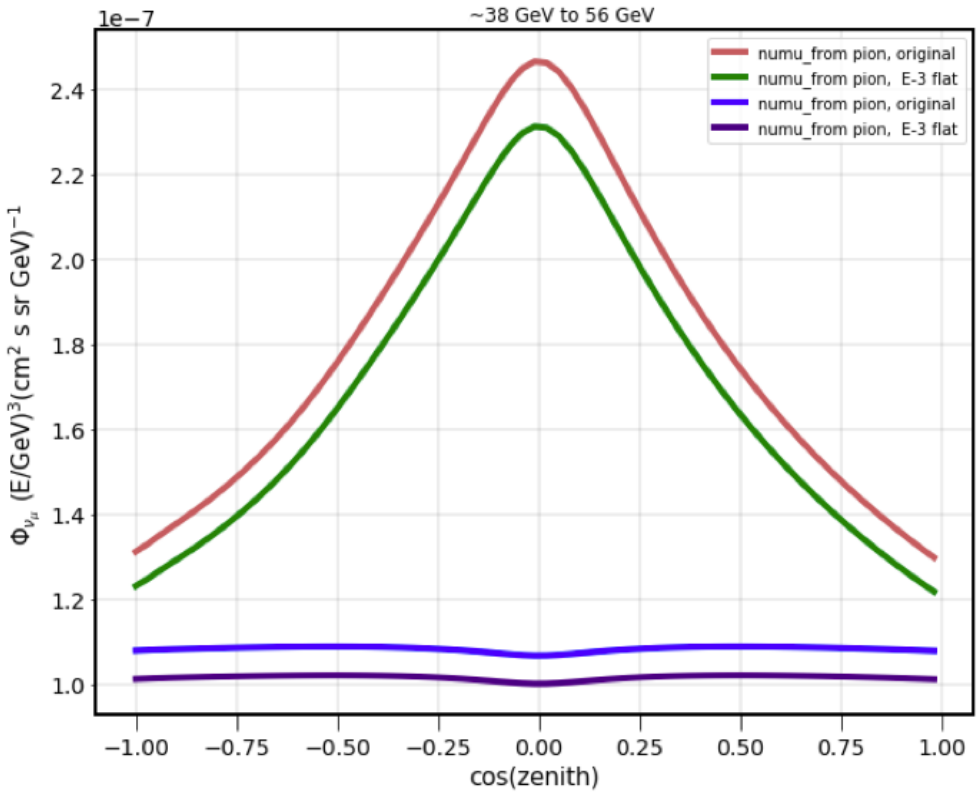

Figure E.3: Zenith projections of an energy segment based on MCEq tables before and after energy spectrum reweighing. Note the shape of the zenith distribution is preserved. This plot shows a mid energy range example segment.

Appendix F

Model Test Results

This appendix shows the detailed results for fit outcomes of each performed analysis. In the first section the results for every considered atmospheric neutrino model in case study A are shown. Reported uncertainties are from MINUIT2.

F.1 A - Model-Dependent Results

H3a DPMJET-III.2017.1		±
Atm. μ contamination [% of sample]	5.3	0.5
atmmu_template	data	
M_A^{res} [σ]	-1.6	
Δm^2_{31} [eV^2]	2.4E-03	1E-04
overall optical eff. [%]	108	3
expected_events	[49967.0]	
expected_events_mc	[49799.6]	
fit_function	chi_squared	
hesse_errors	TRUE	
relative optical eff., head-on (hiFwd) [a.u.]	-0.8	0.4
relative optical eff., lateral (hole ice scattering) [cm^{-1}]	0.2	0.3
χ^2_{mod} (modified χ^2 [3])	1.937E+02	
min_routine	migrad	
nonzero_bins	160	
NC relative normalization [%]	97	2
Neutrino event rate [% of nominal (i.e. detector livetime)]	100% (2.7 years)	
oscMode	Prob3	
θ_{13} [radians]	1.56E-01	8E-03
θ_{23} [radians]	8.35E-01	7E-02

GH.DPMJET-III-2017.1		±
Atm. μ contamination [% of sample]	6.0	0.5
atmmu_template	data	
M_A^{res} [σ]	-3.0	
Δm^2_{31} [eV^2]	2.23E-03	8E-05
overall optical eff. [%]	116	3
expected_events	[49967.0]	
expected_events_mc	[49782.0]	
fit_function	chi_squared	
hesse_errors	True	
relative optical eff., head-on (hiFwd) [a.u.]	-1.2E+00	4E-01
hole_ice	1.1E-02	3E-03
χ^2_{mod} (modified χ^2 [3])	2.296E+02	
min_routine	migrad	
nonzero_bins	160	
NC relative normalization [%]	90	10
Neutrino event rate [years] [% of nominal detector livetime)	2.28	
oscMode	Prob3	
θ_{13} [radians]	1.55E-01	8E-03
θ_{23} [radians]	7.9E-01	5E-02

GH.EPOS-LHC		±
Atm. μ contamination [% of sample]	6.0	0.5
atmmu_template	data	
M_A^{res} [σ]	-3.0	
Δm^2_{31} [eV^2]	2.25E-03	8E-05
overall optical eff. [%]	114	4
expected_events	[49967.0]	
expected_events_mc	[49791.0]	
fit_function	chi_squared	
hesse_errors	True	
relative optical eff., head-on (hiFwd) [a.u.]	-1.2E+00	4E-01
hole_ice	1.1E-02	3E-03
χ^2_{mod} (modified χ^2 [3])	2E+02	
min_routine	migrad	
nonzero_bins	160	
NC relative normalization [%]	90	10
Neutrino event rate [% of nominal (i.e. detector livetime)]	2.36	
oscMode	Prob3	
θ_{13} [radians]	1.55E-01	8E-03
θ_{23} [radians]	7.9E-01	5E-02

GH.DPMJET-III		±
Atm. μ contamination [% of sample]	5.7	0.5
atmmu_template	data	
M_A^{res} [σ]	-3.0	
Δm^2_{31} [eV^2]	2.28E-03	8E-05
overall optical eff. [%]	115	3
expected_events	[49967.0]	
expected_events_mc	[49784.7]	
fit_function	chi_squared	
hesse_errors	True	
relative optical eff., head-on (hiFwd) [a.u.]	-1.3E+00	4E-01
hole_ice	1.1E-02	3E-03
χ^2_{mod} (modified χ^2 [3])	2.250E+02	
min_routine	migrad	
nonzero_bins	160	
NC relative normalization [%]	92	11
Neutrino event rate [% of nominal (i.e. detector livetime)]	2.36	
oscMode	Prob3	
θ_{13} [radians]	1.55E-01	8E-03
θ_{23} [radians]	7.9E-01	5E-02

GH.qgsjet-II-04		±
Atm. μ contamination [% of sample]	5.7	0.5
atmmu_template	data	
M_A^{res} [σ]	-3.0	
Δm^2_{31} [eV^2]	2.26E-03	8E-05
overall optical eff. [%]	116	3
expected_events	[49967.0]	
expected_events_mc	[49777.8]	
fit_function	chi_squared	
hesse_errors	True	
relative optical eff., head-on (hiFwd) [a.u.]	-1.4E+00	4E-01
hole_ice	1.0E-02	3E-03
χ^2_{mod} (modified χ^2 [3])	2.344E+02	
min_routine	migrad	
nonzero_bins	160	
NC relative normalization [%]	91	11
Neutrino event rate [% of nominal (i.e. detector livetime)]	2.21	
oscMode	Prob3	
θ_{13} [radians]	1.55E-01	8E-03
θ_{23} [radians]	7.9E-01	4E-02

GH.SIBYLL2.1		±
Atm. μ contamination [% of sample]	4.8	0.6
atmmu_template	data	
M_A^{res} [σ]	1.1	
Δm^2_{31} [eV^2]	2.69E-03	1E-04
overall optical eff. [%]	105	4
expected_events	[49967.0]	
expected_events_mc	[497190]	
fit_function	chi_squared	
hesse_errors	True	
relative optical eff., head-on (hiFwd) [a.u.]	-1.7E+00	5E-01
hole_ice	1.5E-02	3E-03
χ^2_{mod} (modified χ^2 [3])	2.872E+02	
min_routine	migrad	
nonzero_bins	160	
NC relative normalization [%]	99	11
Neutrino event rate [% of nominal (i.e. detector livetime)]	2.04	
oscMode	Prob3	
θ_{13} [radians]	1.57E-01	8E-03
θ_{23} [radians]	8.6E-01	5E-02

GH.SIBYLL2.3		±
Atm. μ contamination [% of sample]	6.0	0.5
atmmu_template	data	
M_A^{res} [σ]	-3.0	
Δm^2_{31} [eV^2]	2.25E-03	8E-05
overall optical eff. [%]	115	3
expected_events	[49967.0]	
expected_events_mc	[49786.2]	
fit_function	chi_squared	
hesse_errors	True	
relative optical eff., head-on (hiFwd) [a.u.]	-1.3E+00	4E-01
hole_ice	1.1E-02	3E-03
χ^2_{mod} (modified χ^2 [3])	2.245E+02	
min_routine	migrad	
nonzero_bins	160	
NC relative normalization [%]	87	11
Neutrino event rate [% of nominal (i.e. detector livetime)]	2.32E+00	
oscMode	Prob3	
θ_{13} [radians]	1.55E-01	8E-03
θ_{23} [radians]	7.9E-01	5E-02

GSF.DPMJET-III-2017.1		±
Atm. μ contamination [% of sample]	6.8	0.5
atmmu_template	data	
M_A^{res} [σ]	-3.0	
Δm^2_{31} [eV^2]	2.15E-03	9E-05
overall optical eff. [%]	116	3
expected_events	[49967.0]	
expected_events_mc	[497726]	
fit_function	chi_squared	
hesse_errors	True	
relative optical eff., head-on (hiFwd) [a.u.]	-1.5E+00	4E-01
hole_ice	8E-03	3E-03
χ^2_{mod} **(modified χ^2 [3]**)	2.460E+02	
min_routine	migrad	
nonzero_bins	160	
NC relative normalization [%]	98	12
Neutrino event rate [% of nominal (i.e. detector livetime)]	2.41E+00	
oscMode	Prob3	
θ_{13} [radians]	1.54E-01	8E-03
θ_{23} [radians]	7.8E-01	4E-02

GSF.DPMJET-III		±
Atm. μ contamination [% of sample]	6.4	0.5
atmmu_template	data	
M_A^{res} [σ]	-3.0	
Δm^2_{31} [eV^2]	2.20E-03	9E-05
overall optical eff. [%]	115	3
expected_events	[49967.0]	
expected_events_mc	[49782.2]	
fit_function	chi_squared	
hesse_errors	True	
relative optical eff., head-on (hiFwd) [a.u.]	-1.5E+00	4E-01
hole_ice	9E-03	3E-03
χ^2_{mod} (modified χ^2 [3])	2.327E+02	
min_routine	migrad	
nonzero_bins	160	
NC relative normalization [%]	94	11
Neutrino event rate [% of nominal (i.e. detector livetime)]	2.51E+00	
oscMode	Prob3	
θ_{13} [radians]	1.54E-01	8E-03
θ_{23} [radians]	7.8E-01	4E-02

GSF.EPOS-LHC		±
Atm. μ contamination [% of sample]	7.0	0.5
atmmu_template	data	
M_A^{res} [σ]	-3.0	
Δm^2_{31} [eV^2]	2.17E-03	9E-05
overall optical eff. [%]	114	4
expected_events	[49967.0]	
expected_events_mc	[49774.2]	
fit_function	chi_squared	
hesse_errors	True	
relative optical eff., head-on (hiFwd) [a.u.]	-1.5E+00	4E-01
hole_ice	8E-03	3E-03
χ^2_{mod} (modified χ^2 [3])	2.446E+02	
min_routine	migrad	
nonzero_bins	160	
NC relative normalization [%]	96	11
Neutrino event rate [% of nominal (i.e. detector livetime)]	2.49E+00	
oscMode	Prob3	
θ_{13} [radians]	1.54E-01	8E-03
θ_{23} [radians]	7.8E-01	5E-02

GSF.qgsjet-II-04		±
Atm. μ contamination [% of sample]	6.4	0.5
atmmu_template	data	
M_A^{res} [σ]	-3.0	
Δm^2_{31} [eV^2$]	2.19E-03	8E-05
overall optical eff. [%]	116	3
expected_events	[49967.0]	
expected_events_mc	[49776.3]	
fit_function	chi_squared	
hesse_errors	True	
relative optical eff., head-on (hiFwd) [a.u.]	-1.6E+00	4E-01
hole_ice	8E-03	3E-03
χ^2_{mod} (modified χ^2 [3])	2.410E+02	
min_routine	migrad	
nonzero_bins	160	
NC relative normalization [%]	95	11
Neutrino event rate [% of nominal (i.e. detector livetime)]	2.34E+00	
oscMode	Prob3	
θ_{13} [radians]	1.54E-01	8E-03
θ_{23} [radians]	7.8E-01	4E-02

GSF.SIBYLL2.1		±
Atm. μ contamination [% of sample]	5.2	0.6
atmmu_template	data	
M_A^{res} [σ]	1.0	
Δm^2_{31} [eV^2]	2.8E-03	2E-04
overall optical eff. [%]	103	3
expected_events	[49967.0]	
expected_events_mc	[49698.8]	
fit_function	chi_squared	
hesse_errors	True	
relative optical eff., head-on (hiFwd) [a.u.]	-1.8E+00	5E-01
hole_ice	1.5E-02	4E-03
χ^2_{mod} (modified χ^2 [3])	3.103E+02	
min_routine	migrad	
nonzero_bins	160	
NC relative normalization [%]	98	10
Neutrino event rate [% of nominal (i.e. detector livetime)]	2.31E+00	
oscMode	Prob3	
θ_{13} [radians]	1.57E-01	8E-03
θ_{23} [radians]	8.9E-01	5E-02

GSF.SIBYLL2.3c		±
Atm. μ contamination [% of sample]	6.7	0.5
atmmu_template	data	
M_A^{res} [σ]	-3.0	
Δm^2_{31} [eV^2]	2.17E-03	9E-05
overall optical eff. [%]	115	4
expected_events	[49967.0]	
expected_events_mc	[49771.3]	
fit_function	chi_squared	
hesse_errors	True	
relative optical eff., head-on (hiFwd) [a.u.]	-1.5E+00	4E-01
hole_ice	8E-03	3E-03
χ^2_{mod} (modified χ^2 [3])	2.475E+02	
min_routine	migrad	
nonzero_bins	160	
NC relative normalization [%]	93	11
Neutrino event rate [% of nominal (i.e. detector livetime)]	2.45E+00	
oscMode	Prob3	
θ_{13} [radians]	1.54E-01	8E-03
θ_{23} [radians]	7.8E-01	4E-02

H3a.DPMJET-III-2017.1		±
Atm. μ contamination [% of sample]	5.3	0.6
atmmu_template	data	
M_A^{res} [σ]	-1.6	
Δm^2_{31} [eV^2]	2.4E-03	1E-04
overall optical eff. [%]	108	3
expected_events	[49967.0]	
expected_events_mc	[49799.6]	
fit_function	chi_squared	
hesse_errors	True	
relative optical eff., head-on (hiFwd) [a.u.]	-8E-01	5E-01
hole_ice	1.7E-02	3E-03
χ^2_{mod} (modified χ^2 [3])	1.937E+02	
min_routine	migrad	
nonzero_bins	160	
NC relative normalization [%]	1.0E+00	1E-01
Neutrino event rate [% of nominal (i.e. detector livetime)]	2.69E+00	
oscMode	Prob3	
θ_{13} [radians]	1.56E-01	8E-03
θ_{23} [radians]	8.4E-01	8E-02

H3a.DPMJET-III		±
Atm. μ contamination [% of sample]	5.2	0.6
atmmu_template	data	
M_A^{res} [σ]	-1.1	
Δm^2_{31} [eV^2]	2.4E-03	1E-04
overall optical eff. [%]	109	4
expected_events	[49967.0]	
expected_events_mc	[49791.5]	
fit_function	chi_squared	
hesse_errors	True	
relative optical eff., head-on (hiFwd) [a.u.]	-1.0E+00	5E-01
hole_ice	1.6E-02	3E-03
χ^2_{mod} (modified χ^2 [3])	2.021E+02	
min_routine	migrad	
nonzero_bins	160	
NC relative normalization [%]	95	11
Neutrino event rate [% of nominal (i.e. detector livetime)]	2.69E+00	
oscMode	Prob3	
θ_{13} [radians]	1.56E-01	8E-03
θ_{23} [radians]	8.3E-01	7E-02

H3a.EPOS-LHC		±
Atm. μ contamination [% of sample]	5.5	0.6
atmmu_template	data	
M_A^{res} [σ]	-1.2	
Δm^2_{31} [eV^2]	2.4E-03	1E-04
overall optical eff. [%]	109	4
expected_events	[49967.0]	
expected_events_mc	[49792.8]	
fit_function	chi_squared	
hesse_errors	True	
relative optical eff., head-on (hiFwd) [a.u.]	1.0E+00	5E-01
hole_ice	1.7E-02	3E-03
χ^2_{mod} (modified χ^2 [3])	2.024E+02	
min_routine	migrad	
nonzero_bins	160	
NC relative normalization [%]	91	11
Neutrino event rate [% of nominal (i.e. detector livetime)]	2.70E+00	
oscMode	Prob3	
θ_{13} [radians]	1.56E-01	8E-03
θ_{23} [radians]	8.6E-01	6E-02

H3a.qgsjet-II-04		±
Atm. μ contamination [% of sample]	5.1	0.6
atmmu_template	data	
M_A^{res} [σ]	-1.3	
Δm^2_{31} [eV^2]	2.5E-03	1E-04
overall optical eff. [%]	109	4
expected_events	[49967.0]	
expected_events_mc	[49792.1]	
fit_function	chi_squared	
hesse_errors	True	
relative optical eff., head-on (hiFwd) [a.u.]	-1.1E+00	5E-01
hole_ice	1.6E-02	3E-03
χ^2_{mod} (modified χ^2 [3])	2.016E+02	
min_routine	migrad	
nonzero_bins	160	
NC relative normalization [%]	95	11
Neutrino event rate [% of nominal (i.e. detector livetime)]	2.57E+00	
oscMode	Prob3	
θ_{13} [radians]	1.56E-01	8E-03
θ_{23} [radians]	8.3E-01	7E-02

H3a.SIBYLL2.1		
Atm. μ contamination [% of sample]	4.8	0.5
atmmu_template	data	
M_A^{res} [σ]	3.0	
Δm^2_{31} [eV^2]	2.7E-03	1E-04
overall optical eff. [%]	105	3
expected_events	[49967.0]	
expected_events_mc	[49701.1]	
fit_function	chi_squared	
hesse_errors	True	
relative optical eff., head-on (hiFwd) [a.u.]	-1.6E+00	5E-01
hole_ice	1.8E-02	3E-03
χ^2_{mod} (modified χ^2 [3])	3.187E+02	
min_routine	migrad	
nonzero_bins	160	
NC relative normalization [%]	98	10
Neutrino event rate [% of nominal (i.e. detector livetime)]	2.11E+00	
oscMode	Prob3	
θ_{13} [radians]	1.58E-01	8E-03
θ_{23} [radians]	9.0E-01	4E-02

H3a.SIBYLL2.3c		
Atm. μ contamination [% of sample]	5.4	0.6
atmmu_template	data	
M_A^{res} [σ]	-1.4	
Δm^2_{31} [eV^2]	2.4E-03	1E-04
overall optical eff. [%]	109	4
expected_events	[49967.0]	
expected_events_mc	[49792.3]	
fit_function	chi_squared	
hesse_errors	True	
relative optical eff., head-on (hiFwd) [a.u.]	-1.0E+00	5E-01
hole_ice	1.7E-02	3E-03
χ^2_{mod} (modified χ^2 [3])	2.021E+02	
min_routine	migrad	
nonzero_bins	160	
NC relative normalization [%]	88	11
Neutrino event rate [% of nominal (i.e. detector livetime)]	2.69E+00	
oscMode	Prob3	
θ_{13} [radians]	1.56E-01	9E-03
θ_{23} [radians]	8.5E-01	7E-02

HONDA_2015 (HKKM2014)		
Atm. μ contamination [% of sample]	5.1	0.5
atmmu_template	data	
M_A^{res} [σ]	-0.4	
Δm^2_{31} [eV^2]	2.48E-03	1E-04
overall optical eff. [%]	106	4
expected_events	[49967.0]	
expected_events_mc	[49795.4]	
fit_function	chi_squared	
hesse_errors	True	
relative optical eff., head-on (hiFwd) [a.u.]	-1.4E+00	4E-01
hole_ice	1.6E-02	3E-02
χ^2_{mod} (modified χ^2 [3])	1.930E+2	
min_routine	migrad	
nonzero_bins	160	
NC relative normalization [%]	88	11
Neutrino event rate [% of nominal (i.e. detector livetime)]	2.46E+00	
oscMode	Prob3	
θ_{13} [radians]	1.57E-01	8E-03
θ_{23} [radians]	8.2E-01	6E-02